ORNL/SPR-2025/1
M2LW-25OR0403045

Light Water Reactor Sustainability Program

Structural Assessment of Concrete Biological Shield and Vessel Supports under In-Service and Accidental Conditions

Yann Le Pape
Carlo Parisi
Mohammed Alnaggar

January 2025

U.S. Department of Energy
Office of Nuclear Energy

ORNL/SPR-2025/1
M2LW-25OR0403045

Structural Assessment of Concrete Biological Shield and Vessel Supports under In-Service and Accidental Conditions

Yann Le Pape
Carlo Parisi
Mohammed Alnaggar

January 2025

OAK RIDGE National Laboratory

ORNL IS MANAGED BY UT–BATTELLE LLC FOR THE US DEPARTMENT OF ENERGY

ORNL/SPR-2025/1
M2LW-25OR0403045

Nuclear Energy and Fuel Cycle Division

STRUCTURAL ASSESSMENT OF CONCRETE BIOLOGICAL SHIELD AND VESSEL SUPPORTS UNDER IN-SERVICE AND ACCIDENTAL CONDITIONS

Yann Le Pape
Carlo Parisi
Mohammed Alnaggar

January 2025

Prepared by
OAK RIDGE NATIONAL LABORATORY
Oak Ridge, TN 37831
managed by
UT-BATTELLE LLC
for the
US DEPARTMENT OF ENERGY
under contract DE-AC05-00OR22725

CONTENTS

LIST OF FIGURES

LIST OF TABLES

LIST OF ABBREVIATIONS

APS	Arizona Public Service
ATWS	anticipated transients without scram
BC	boundary condition
BWR	boiling water reactor
CAMP	Code Applications and Maintenance Program
CBS	concrete biological shield
CCB	concrete containment building
CMPD	core mid-plane distance
DEGB	double-ended guillotine break
DOE	US Department of Energy
EFPY	equivalent full-power year
FEA	finite element analysis
FEM	finite element method
ICAP	International Code Assessment and Applications Program
ID	inner diameter
INL	Idaho National Laboratory
IRUG	International RELAP5 Users Group
JCAMP	Japan Concrete Aging Management Program
LBLOCA	leg break loss-of-coolant accident
LDPM	lattice discrete particles model
LOCA	loss-of-coolant accident
LWR	light-water reactor
LWRS	Light-Water Reactor Sustainability
MCNP	Monte Carlo N-Particle
NPP	nuclear power plant
NRC	US Nuclear Regulatory Commission
NSSS	nuclear steam supply system
OBE	operating basis earthquake
OD	outer diameter
ODE	ordinary differential equation
ONS	Oconnee Nuclear Station
ORNL	Oak Ridge National Laboratory
PWR	pressurized water reactor
RIVE	radiation-induced volumetric expansion
RPV	reactor pressure vessel
RSBM	rigid-body spring model
RVSS	reactor vessel structural support
SAM	semi-analytical model
SRP	Standard Review Plan
SSE	safe shutdown earthquake
TMI	Three Mile Island
VERA	Virtual Environment for Reactor Applications
WWER–VVER	water-water energetic reactor

EXECUTIVE SUMMARY

This report focuses on the safety and structural integrity of concrete shield walls that protect and support critical components in nuclear power plants. Specifically, the report examines the concrete biological shield (CBS) and the support system for the reactor pressure vessel (RPV) in pressurized water reactors (PWRs). These concrete structures are crucial for protecting workers and equipment from radiation, and they also help support the reactor pressure vessel.

Over time, radiation from the reactor weakens the concrete. This report explores how irradiation and various accident scenarios such as pipe breaks (loss-of-coolant accidents [LOCAs]) and earthquakes affect these structures. This report uses computer simulations to help determine how radiation causes cracks in the concrete and how these cracks affect the concrete's ability to resist forces like pressure and weight.

In the reactor, the concrete shield and its support system are constantly exposed to radiation that changes the properties of the concrete over time. One of the primary concerns is how radiation causes the concrete to expand, causing cracks that could weaken its ability to support the reactor vessel.

One key finding is that radiation does not only affect the areas directly exposed to neutron damage; it also causes the concrete to expand in a way that creates internal stresses. This is known as *radiation-induced volumetric expansion* (RIVE), and it can lead to additional cracking in the concrete. As these cracks grow over time, they can weaken the structural integrity of the concrete shield, affecting its ability to withstand external forces from earthquakes or accidents.

The report focuses on two main areas: first, how the concrete biological shield (CBS) performs under normal operations and how it responds to accident conditions like those caused by pipe breaks; and second, how the shield and support systems handle dynamic loads during events like earthquakes. Although this study does not address the effects of irradiation on steel supports directly, it does examine how irradiated concrete might impact the overall support system.

By using various simulation methods, the research shows that cracks form in the concrete over time as a result of irradiation, particularly in the areas under high stress from the reactor's radiation. These cracks are mainly caused by expansion of the concrete, which is a key factor in understanding the long-term behavior of these structures. This report also notes that irradiation can increase the depth of damage in the concrete over decades, with significant effects visible after 40, 60, and 80 years of operation.

To better estimate how these changes affect the concrete's ability to support the reactor pressure vessel, a simplified analytical method, 1D-SAM, was developed. This method allows for faster calculations and can be used to predict how deep the damage will extend in the concrete over time, making it possible to conduct large-scale studies more easily.

The report also explores how accidents such as a LOCA might worsen the damage to the concrete. A combination of computer models was used to determine that the irradiation damage could extend further into the concrete during such events, but the increase was relatively small, approximately 4 cm deeper in some cases. Additionally, the report addresses how the support systems interact with irradiated concrete, particularly the shoe-type and cantilever beam systems which are directly connected to the concrete and could be more vulnerable to the effects of irradiation compared to skirt or columns support systems.

Finally, a detailed analysis of the shoe-type support system was conducted which examined its ability to carry loads during accidents like a pipe break. The study found that the safety margin for the support system is relatively low, especially when considering the weakening of the concrete from radiation. Although the system was found to be strong enough under some conditions, irradiation-induced damage, particularly

to the concrete, reduces its overall strength. This finding suggests that further research and more detailed simulations are needed to better understand the role of reinforcement in these systems and to improve the accuracy of safety assessments for long-term operation.

ACKNOWLEDGMENTS

This research was sponsored by the US Department of Energy (DOE) Office of Nuclear Energy Light Water Reactor Sustainability Program Cross-Pathway Activities between the Materials Research Pathway and the Risk-Informed Systems Analysis Pathway under contract DE-AC05-00OR22725 with UT-Battelle LLC / Oak Ridge National Laboratory (ORNL).

ABSTRACT

This report addresses the strength and safety of the concrete structures that support the reactor and pressure vessel in a nuclear power plant. It examines how the structure responds to the effects of radiation over time, as well as the impact of accidents like pipe breaks (loss-of-coolant accidents). This analysis used a computer program called RELAP5-3D to simulate the temperature and pressure changes that occur during a pipe break in the reactor. The report also includes detailed structural analysis that was performed using different analytical and numerical methods to improve understanding of how the materials and design hold up under these conditions.

FOREWORD

The analysis presented in this report assumes concrete properties obtained under accelerated irradiation conditions in test reactors. Although in-service irradiated concrete properties have yet to be obtained through a harvesting program, preliminary data from the Japan Concrete Aging Management Program (JCAMP) and Oak Ridge National Laboratory (ORNL) for the US Nuclear Regulatory Commission (NRC) indicate a reduction in the radiation-induced volumetric expansion (RIVE) as the fast neutron flux decreases toward in-service irradiation in pressurized water reactors (PWRs). Re-evaluation of the analysis results presented here will be needed in the future if significant differences in irradiated concrete properties between in-service and accelerated irradiation conditions are found.

1. INTRODUCTION

In light-water reactors (LWRs), the CBS is the concrete structure directly facing the reactor pressure vessel (RPV). The CBS's primary function is to protect equipment and personnel from the radiation exiting the RPV: that is, neutron and gamma irradiation. Concrete contains a large amount of high–cross-section hydrogen from the constitutive water (≈150–200 L m^{-3}), ensuring excellent shielding propertiesin the concrete (M.F Kaplan 1971, 1983). Unlike some water-water energetic reactors (WWER–VVERs) designs (Khmurovska et al. 2019), the CBS does not include a specific heavy-aggregate concrete shield (e.g., hematite, ilmenite, or magnetite); instead, it is made of natural aggregate structural concrete (Hookham 1991) that is similar to the the structural concrete used for the construction of other parts of the nuclear power plant, such as the containment building. The CBS is typically more massive in PWRs than the internal structures in boiling water reactor boiling water reactor (BWR) designs because it typically supports the RPV, the steam generators, and other large equipment. However, this is not always the case because in some designs, the RPV is supported by steel columns embedded in the CBS. The function of the RPV support structure is to transfer the static or seismic load of the reactor to the foundation system. Depending on the nuclear steam supply system (NSSS) (i.e., reactor, reactor coolant pump generator, steam generator in the PWR, and associated piping), a PWR RPV can weigh as much as 427,000 kg (941,600 lb) (Mager et al. 1999; Hookham 1991), excluding the core and the refueling cavity elements. The thickness of the biological shield wall varies according to the NSSS design Verrall and Fitzpatrick 1985, typically ranging between 1.5 and 2.2 m (4.9–7.2 ft) for PWRs and 0.60 and 1.20 m (2–4 ft) for BWRs. The total height of the CBS can reach up to ≈ 9 m. The most common form of RPV support includes short columns, support beams, and pedestals embedded in the CBS below the nozzles. The beams supporting the girders placed directly below the nozzle are located at the approximate elevation of the top of the fuel assembly. Thus, the support columns are located in a zone of active neutron and fluence exposure.

At a projected operation of 80 years, the surface of the CBS is exposed to the following irradiation conditions:

- Fast neutron flux: $\sim 0.1 - 0.2 \times 10^{11}$ n.cm^{-2} s^{-1} ($E > 0.1$ MeV),
- Fast neutron fluence: $2.0 - 6.0 \times 10^{19}$ n.cm^{-2} ($E > 0.1$ MeV),
- Gamma dose rate: ~ 10 kGy h^{-1},
- Gamma dose: ~ 100 MGy,
- Gamma heating: ~ 0.02 W g^{-1}, and
- Temperature: < 65 °C (by design).

From a long-term structural analysis point of view, the following items need to be addressed:

1. Structural integrity of the RPV support system,
2. Structural integrity of the CBS to transfer the in-service passive load to the foundation,
3. Structural integrity of the CBS to transfer dynamic loads to the foundation during an earthquake, and
4. Structural integrity of the CBS during a loss-of-coolant accident (LOCA).

Item 2 is addressed in a previously published Light-Water Reactor Sustainability (LWRS) report entitled "Assessment of the Effect of the Irradiation-Induced Degradation on the In-Service Structural Performance of the Concrete Biological Shields" (ORNL/SPR-2023/3031, M3LW-23OR040301). In that report, two different simulation methods—namely finite element analysis and the lattice discrete particle model—were used to determine that in-service irradiation causes crack formation in the concrete facing the reactor cavity. Cracks open along the radial direction of the CBS because the portion of the concrete that is most subjected to damaging fast-neutron fluence is subject to compressive stresses in the vertical and the orthoradial directions. This structural effect is caused by restrained radiation-induced volumetric expansion. In the plane located at the reactor's approximate core mid-elevation, the depth of concrete subject to irradiation-induced cracking varies over time, reaching ≈8, 10, and 11 cm at 40, 60, and 80 years, respectively. From the point of view of the in-service structural function of the CBS, which is to transfer the passive loading of the NSSS, including that of the reactor pressure vessel, the assessment report demonstrated that approximately 95% of the CBS cross section at the elevation where the neutron flux is the highest remains sound and can transfer the in-service loading to the foundation.

This report addresses the impact of in-service irradiation on the structural integrity of the CBS) during a (LOCA or an earthquake. The objective of this research is to determine whether long-term operation affects the supporting function of the CBS during a LOCA.

During a LOCA caused by a double-end rupture of the cold leg (the most critical scenario for PWRs), it is anticipated that in the worst-case scenario, the temperature and pressure in the air gap between the pressure vessel and the CBS will increase suddenly and will then remain relatively steady for several hours. Under these conditions, the inner surface of the CBS will be subjected to a thermal shock with the potential to cause concrete dehydration, water vaporization, and restrained thermal expansion–induced stress in concrete areas previously damaged by in-service irradiation. The jet thrust at the break will also cause a lateral force that will act on the RPV support.

The key question is whether damage induced by a LOCA will exacerbate the pre-existing damage resultling from in-service irradiation at various operational times, possibly leading to the catastrophic failure of the CBS and the NSSS.

2. CONCRETE BIOLOGICAL SHIELD DESIGNS

2.1 GENERAL PRINCIPLES

The "Standard Review Plan (SRP) for the *Standard Review Plan for the Review of Safety Analysis Reports for Nuclear Power Plants: LWR Edition* (n.d.) provides guidance to NRC staff in performing safety reviews of construction permit (CP) or operating license (OL) applications (including requests for amendments) under 10 CFR Part 50 and early site permit (ESP), design certification (DC), combined operating license (COL), standard design approval (SDA), or manufacturing license (ML) applications under 10 CFR Part 52 (including requests for amendments).

Section 3.8.3 of the SRP addresses "Concrete and Steel Internal Structures of Steel or Concrete Containments." To perform safety-related functions, these structures must be capable of resisting loads and load combinations to which they may be subjected and should not become the initiator of a LOCA. If such an accident were to occur, then the structures must be able to mitigate its consequences by protecting the containment and other engineered safety features from effects such as jet forces and whipping pipes.

PWR dry containment internal structures include concrete supports for the reactor, the primary shield, and the reactor cavity. Depending on the PWR design, the support and shield functions can be combined (e.g., the CBS directly supports the reactor) or separated (e.g., the reactor is supported by embedded steel columns).

Concrete Supports for Reactor

> *The PWR vessel should be supported and restrained to resist normal operating loads [e.g., static loads and thermal loads], seismic loads, and loads induced by postulated pipe rupture, including LOCAs. The support and restraint system should restrain the movement of the vessel to within allowable limits under the applicable load combinations. However, the support system should minimize resistance to the thermal movements expected during operation. With these functional requirements in mind, the review evaluates the general arrangement and principal features of the reactor vessel supports, with an emphasis on the methods of transferring loads from the vessel to the support and ultimately to the structure and its foundations* (NUREG-0800, Section 3.8.3).

Primary Shield Wall and Reactor Cavity

> *The primary shield wall forms the reactor cavity and usually supports and restrains the reactor vessel. It is often a thick wall that surrounds the reactor vessel and may be anchored through the liner plate to the containment base slab. The review evaluates the general arrangement and principal features of the wall and cavity, including the reinforcement and anchorage system* (NUREG-0800, Section 3.8.3]).

2.2 REACTOR SUPPORT DESIGN

Several designs of RPV support systems exist in PWRs operating in the United States. Appendix D of NUREG/CR-7280 provides design details of the reactor support systems for several US plants (Biwer et al. 2021). These systems can be categorized as vertical column support systems, neutron shield tanks, support skirts, shoe-type supports, and ring girder supports. The designs are detailed below, and they are ranked in terms of their susceptibility to in-service irradiation- and LOCA-induced degradation of the CBS.

2.2.1 Vertical Columns

In this design, the reactor loads are transferred to the base mat located beneath the reactor cavity through steel columns, the number of which varies from one design to another.

Arkansas Nuclear One (ANO) Unit 2

At ANO Unit 2, a Combustion Engineering two-loop PWR, only three vertical columns are present (see Figure 1).

Prairie Island Units 1 and 2

Prairie Island Units 1 and 2 are Westinghouse two-loop PWRs. Each unit is supported by six steel columns which are welded to or braced by a surrounding metal band at the top, all of which are embedded in the CBS wall (Figure 2).

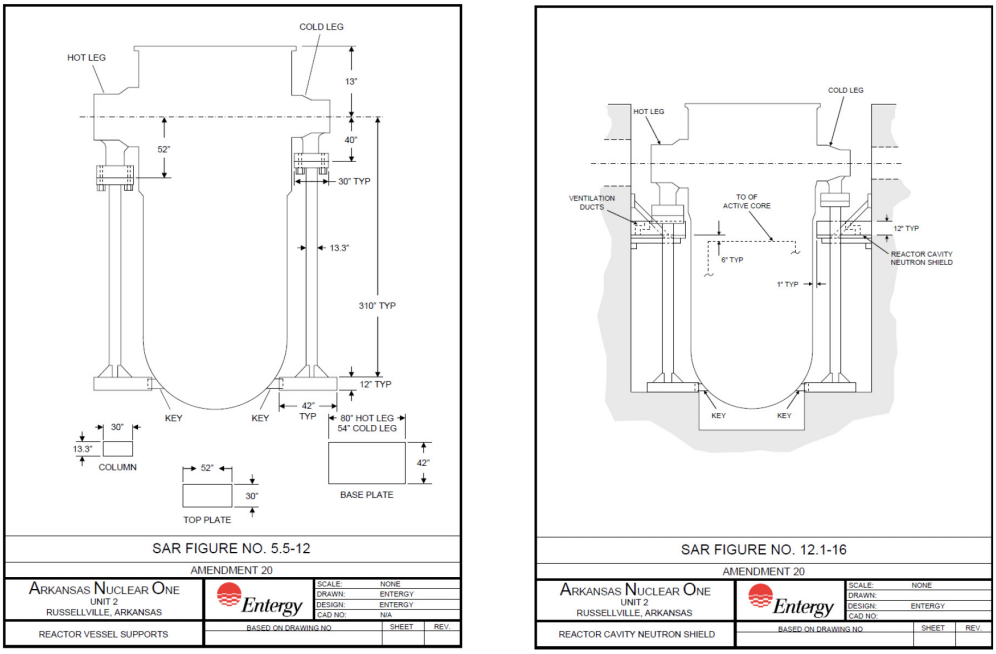

Figure 1. ANO reactor vessel support design (left) and reactor cavity neutron shield (right), Entergy Operations, Inc., 2016, ANO Unit 2, Safety Analysis Report Amendment 26, Docket No. 50-368, Russellville, AR, ADAMS Accession No. ML18092A457.

The function of the columns is limited to transferring vertical loads. These columns are embedded in the CBS, but their structural design treats them as independent from the surrounding concrete, thereby neglecting potential interactions. Such interactions may primarily affect the concrete surrounding the columns. For example, Risner, Alpan, and Yang (2020) found that irradiation-induced energy deposition in embedded steel columns causes an increase in the heating rate by a multiplying factor of approximately 8. That study has not been extended to analyze heat transfer and its consequences on the material properties; furthermore, thermal gradient–induced degradation in the surrounding concrete has not been analyzed.

Horizontal loads are carried by a horizontal bracket system embedded in the concrete at an elevation immediately below the RPV nozzle (Prairie Island). Each nozzle is supported by a ventilated hollow box pad to limit the temperature in the column, the bracket, and the supporting concrete. The design temperature at the bottom of the plate is 150 ^{o}F. This temperature also corresponds to the American Concrete Institute 349 code design value for in-service concrete temperature.

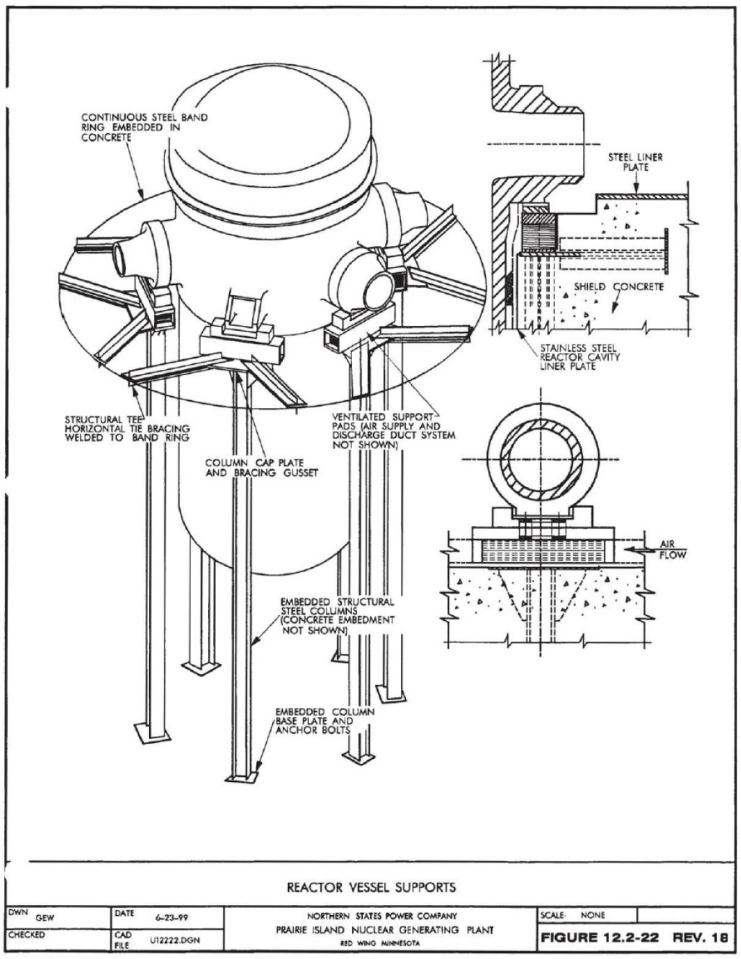

Figure 2. Prairie Island reactor vessel support design, Xcel Energy, 2018, Prairie Island Nuclear Generating Plant Units 1 and 2, Updated Safety Analysis Report Revision 35, Dockets 50-282 and 50-306, Welch, MN. ADAMS Accession No. ML18155A440 - Chapter 5; ML18155A456 - Chapter 12.

2.2.2 Neutron Shield Tank

Some designs include a shield tank that is attached to the CBS wall.

Beaver Valley

At the Beaver Valley plant,

> *. . . the reactor vessel structural support (RVSS) is a cylindrical, skirt-supported, double-walled structure designed to transfer loading to the reinforced concrete mat of the containment structure and to the surrounding primary shield wall; it is fabricated of SA-516, Gr-70 plate.* ***This component support is designed to restrain vertical, lateral, and rotational movement of the reactor vessel while permitting thermal expansion/contraction of the reactor vessel during plant operation.*** *The reactor vessel is set on leveling devices between each of the six RPV loop nozzle pads and the top of the support structure. This support is also designed to provide neutron shielding and thermal protection to the surrounding structure by means of a water-filled annular section, as well as to house and cool the ex-core neutron detectors* (FENOC 2024).

See Figure 3 for a drawing of the neutron shield tank.

> *The reactor vessel support/leveling device, fabricated with material in compliance with the ASTM A-668-72 Type K material specification, is shown on Figure 4. The triple wedge shape device is positioned (without mechanical attachment) between each of the six reactor vessel nozzle pads and a lubricated plate which is fastened to the top surface of the reactor vessel structural support. The functional requirement of the RPV support/leveling device is to provide vertical adjustment at each RPV nozzle restraint pad during installation of the reactor vessel. Each support/leveling device has a screw assembly to produce relative horizontal translation of the wedge shaped plates, which results in a limited vertical adjustment of the reactor vessel during installation. During all plant conditions, this support system is designed to transfer only vertically downward (compression) loads from the reactor vessel nozzle pads to the reactor vessel structural support. Upward loads are reacted by gib keys* (FENOC 2024).

North Anna Units 1 and 2

North Anna Units 1 and 2 are Westinghouse three-loop PWRs. Supported by shoes under all six nozzles, each RPV rests directly on a neutron shield tank that is grouted into the shield wall (Biwer et al. 2021). The shield wall provides lateral stability for the shield tank, and the shield tank is supported by the concrete base mat. The neutron shield tank is designed to resist a differential pressure of 130 psi (~0.9 MPa).

The presence of the neutron shield tank causes an important attenuation of the fast neutron flux which affects the CBS wall. The support elements are directly located above the shield tank, thus transferring the load to the RVSS.

2.2.3 Support Skirt

Other RPVs are directly supported by a steel skirt located under the vessel resting directly on the base mat. Similar designs are found in BWRs.

Three Mile Island

Three Mile Island (TMI) is a 2-loop Babcock and Wilcox PWR.

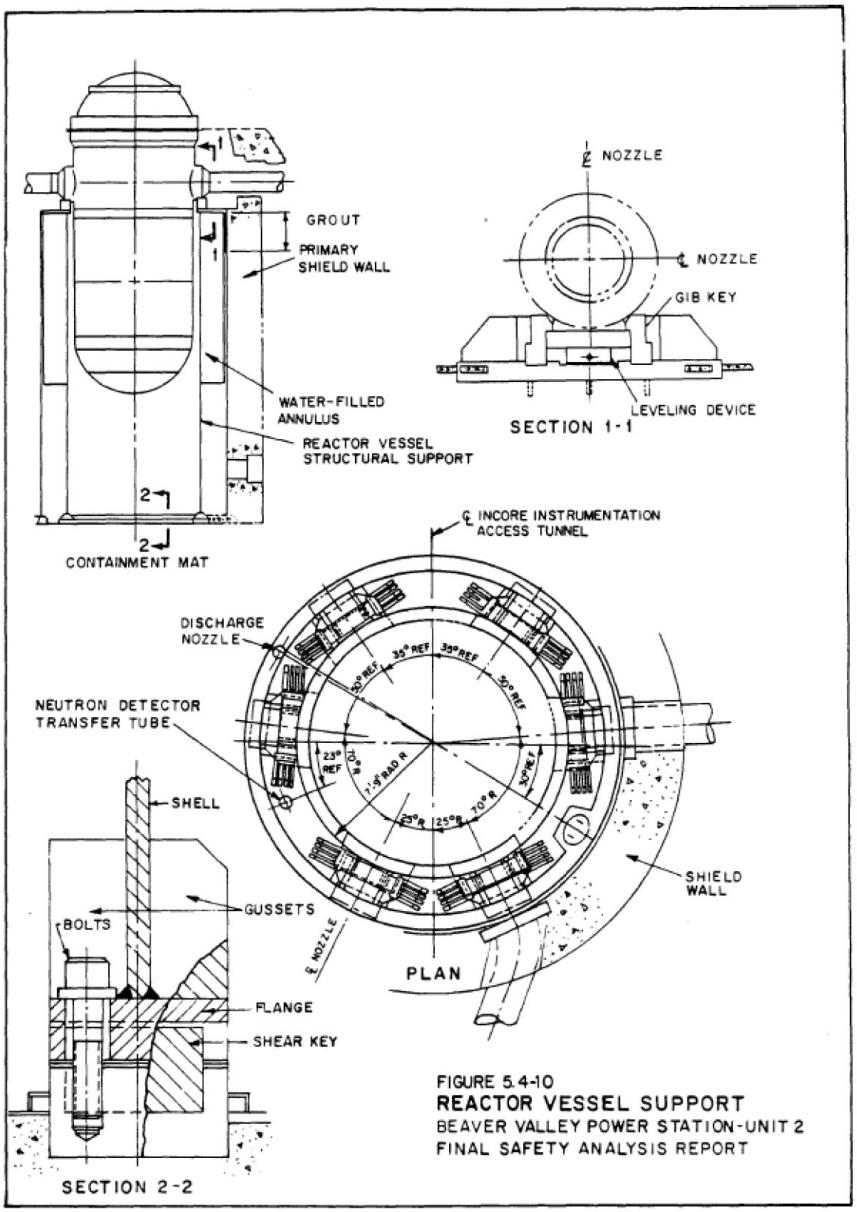

Figure 3. Beaver Valley Unit 2 reactor vessel support design – neutron shield tank (FENOC 2024).

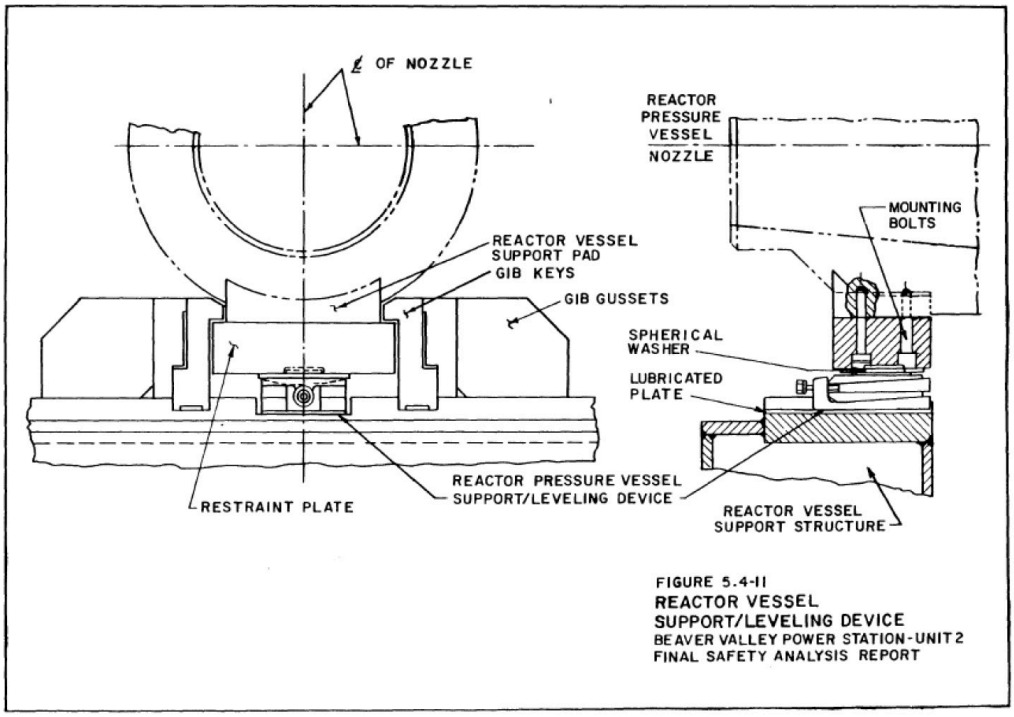

Figure 4. Beaver Valley Unit 2 reactor vessel support shoe design (FENOC 2024).

The reactor vessel is bolted to reinforced concrete foundation designed to support and position the vessel and withstand the forces imposed on it by a combination of loads, including the weight of vessel and internals, thermal expansion of the piping, design basis earthquake, and dynamic load following reactor trip. The foundation, in addition, restrains the vessel during the combined forces imposed by circumferential rupture of a 36 inch reactor outlet line and a simultaneous maximum hypothetical earthquake. The vessel foundation is also designed to provide accessibility for the installation and later inspection of in-core instrumentation, piping and nozzles, to contain duct work and vent space for cooling air, to remove heat losses from the vessel insulation, and, to provide a drainage line for leak detection (Exelon Generation 2018).

Arkansas Nuclear One, Unit 1

Arkansas Nuclear One, Unit 1, is a 2-loop Babcock and Wilcox PWR.

The reactor vessel supports include a support skirt and support flange. The reactor vessel support skirt is a cylindrical structure that supports the reactor vessel. The support skirt rests on a sole plate. The sole plate is fixed to a supporting, reinforced concrete pedestal through a steel flange bolted to the pedestal. The evaluation boundary of the reactor vessel support skirt begins at the weld of the skirt to the reactor vessel transition forging and terminates at the bottom of the skirt flange. The evaluation boundary also includes the exposed surface of the anchor bolts and shear pins. The reactor vessel support skirt was designed, fabricated, tested, and inspected in accordance with ASME Section III (Reference 2.4-5). The support skirt consists of two carbon steel semi-circular rings welded together to form a cylinder. This cylinder is welded to the bottom of the reactor vessel transition forging. The cylinder has holes for ventilation of the reactor vessel cavity. The anchor bolts are prestressed to accommodate the loads of a design basis seismic event (Entergy Operations Inc. 2000).

Although Entergy and Exelon (Entergy Operations Inc. 2000; Exelon Generation 2018) have not provided any drawings of the support system, these drawings can be found in "Oconnee Nuclear Station Units 1, 2, and 3 Application for Subsequent License Renewal Appendix E – Applicant's Environmental Report" (Framatome 2021). Figure 5 and Figure 6 present the general support assembly and a detail of the support connection with the concrete pedestal, respectively. "The support flange is bolted to the concrete with 48 bolts spaced equally around the outside of the flange, and 48 bolts spaced equally around the inside part of the flange" (Framatome 2021).

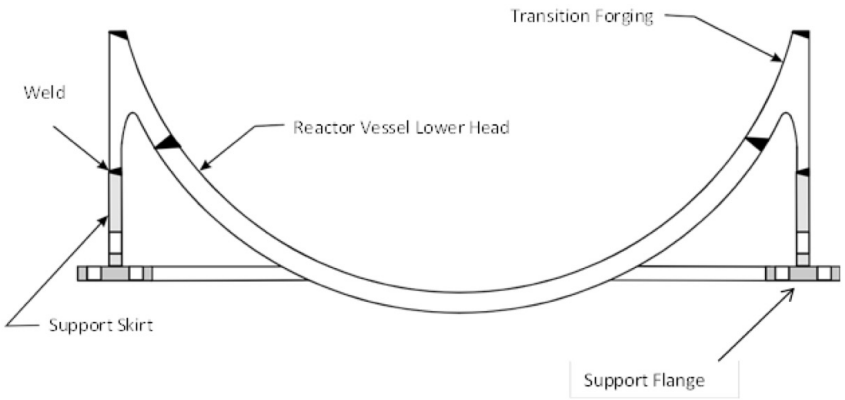

Figure 5. Reactor pressure vessel support assembly at Oconnee Nuclear Station.

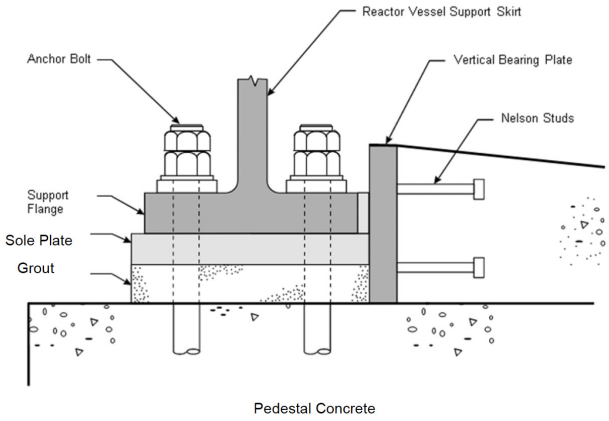

Figure 6. Reactor pressure vessel support embedment detail at Oconnee Nuclear Station.

2.2.4 Shoe Supports

In the absence of a neutron shield tank, the nozzle supports are placed directly on the CBS wall. Examples of such a design are provided below.

Calvert Cliffs Units 1 and 2

Calvert Cliffs Units 1 and 2 are Combustion Engineering–designed two-loop PWRs. The support design is described as follows :

> *The reactor vessel is supported vertically and horizontally by three pads welded to the underside of the reactor vessel nozzles. Each assembly consists of the following – [Figure 7]:*
>
> *a. A support foot (SA-508 CL2) welded to a reactor coolant nozzle;*
>
> *b. A socket [American Society for Testing and Materials (ASTM A283-67)] bolted to the support foot with Allenoy cap screws; and*
>
> *c. A sliding bearing (ASTM B22, Alloy E) whose spherical crown fits into the socket and whose flat sliding surface rests on a base plate (AISI-4140).*
>
> *The arrangement of the vessel supports allows radial growth of the reactor vessel due to thermal expansion while maintaining it centered and restrained from movement caused by seismic disturbances.*
>
> *The functions of the supports are:*
>
> *1. Restrain the vessel to maintain the integrity of emergency core cooling systems and to prevent the rupture of additional primary pipes should LOCA occur due to single pipe rupture;*
>
> *2. Permit slow radial thermal expansion of the vessel under normal operation; and*
>
> *3. Restrain the vessel against seismic and LOCA jet forces.*

(Exelon Generation Company LLC 2017)

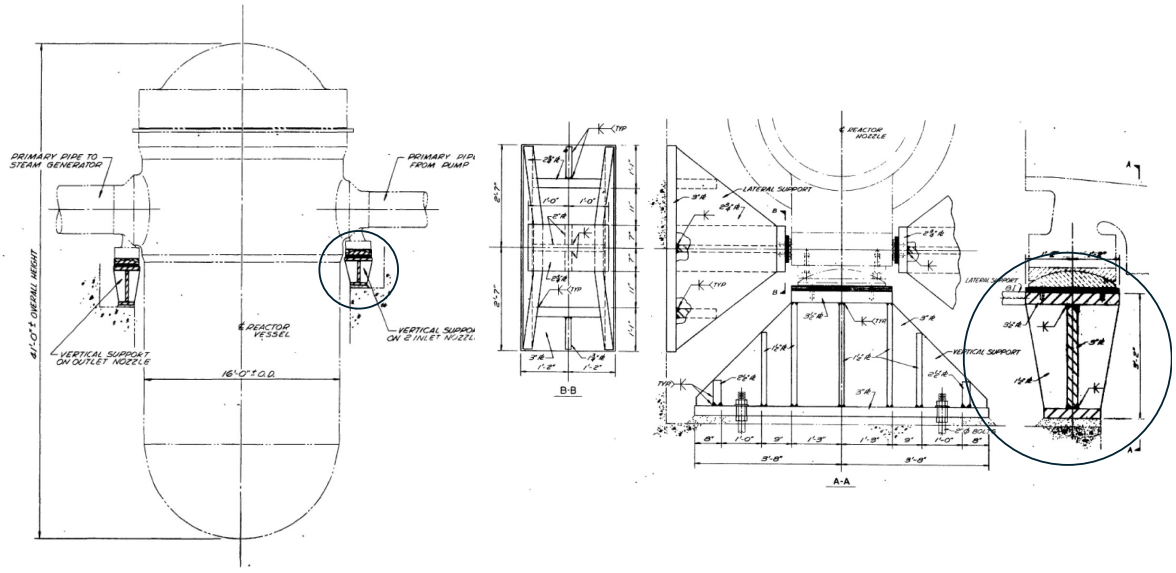

Figure 7. Calvert Cliffs Units 1 and 2 reactor core position relative to supports (left) and reactor vessel support detail (right) (Exelon Generation Company LLC 2017).

Farley Units 1 and 2

In these Westinghouse three-loop PWRs, the reactor vessel supports rest directly on the CBS wall.

> *Supports for the reactor vessel are individual, air-cooled, rectangular-box structures beneath the vessel nozzles bolted to the primary shield wall concrete. Each box structure consists of a horizontal top plate that receives loads from the reactor vessel shoe, a horizontal bottom plate supported by and transferring loads to the primary shield wall concrete, and connecting vertical plates. The supports are air-cooled to maintain the supporting concrete temperature at or below 190°F at a flow rate of 2,000 ft^3/min with an air temperature of 120°F to meet the acceptance criteria for the localized concrete temperature of 200°F. However, recognizing the potential degradation of the RPV supports subjected to sustained temperatures higher than 15°F, Farley Nuclear Plant has committed (NEL letter #00-279 to USNRC) to an augmented program to inspect the structural components including portions of the RVSS in the containment buildings as part of the maintenance rule structural monitoring program. This program will ensure that significant cracking of RVS that could affect the structural support of the reactor vessel or cause out of plumbness conditions will be detected and corrected.* (NRC commitment CTS #10533)

H. B. Robinson

In the H. B. Robinson Nuclear Generating Station, also a Westinghouse three-loop PWR,

> *The reactor vessel support structure consists of a circular box section ring girder, fabricated of carbon steel plates. The bottom flange of the girder is in continuous contact (except for openings for neutron detectors) with a non-yielding concrete foundation. The reactor vessel has three supports located at alternate nozzles. Each support bears on a support shoe, which is fastened to the support structure. The support shoe is a structural member that transmits*

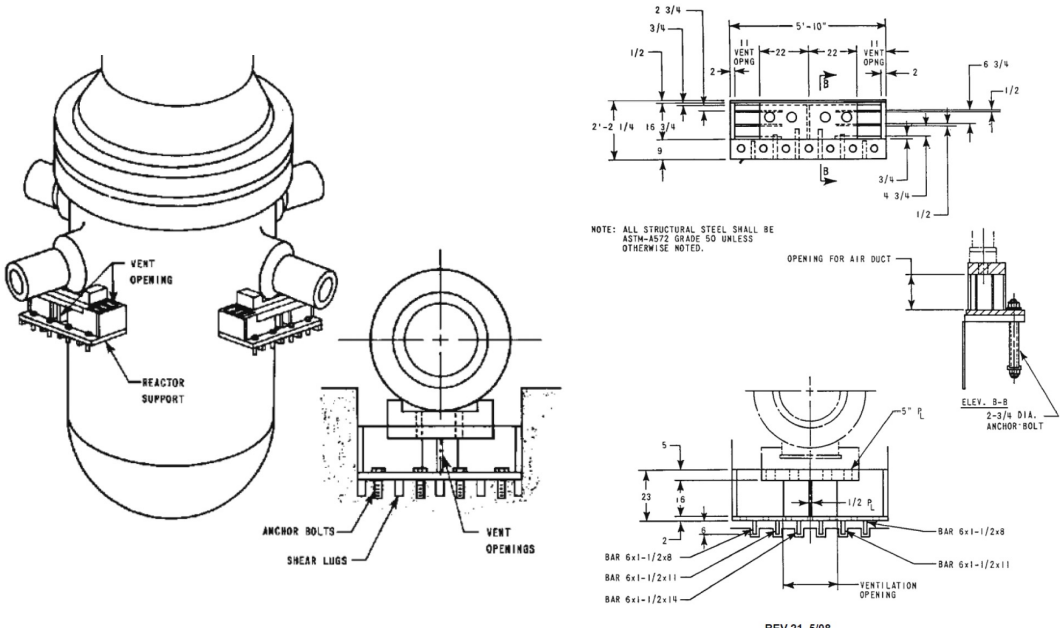

Figure 8. Farley Units 1 and 2 reactor vessel support design (left) and reactor vessel support box (right) (Southern Nuclear 2017).

> *the support loads to the supporting structure. Each support shoe is designed to restrain vertical, lateral, and rotational movement of the reactor vessel, but allows for thermal growth by permitting radial sliding on bearing plates* (Carolina Power & Light 2017).

Shearon Harris Unit 1

Shearon Harris units are also Westinghouse three-loop pressurized water reactor (PWR).

> *The reactor pressure vessel (RPV) is supported and restrained to resist normal operating loads, seismic loads, and loads induced by the postulated pipe ruptures, including a LOCA. The RPV is supported at six points, the three inlet and three outlet nozzles, so that adjacent supports are 50 or 70 degrees apart. Steel pads, which are an integral part of the nozzles, rest on a steel bearing block atop a steel support pedestal.*

It appears that the drawing of the supports shows the same Farley Units 1 and 2 Reactor Vessel Support Design (Biwer et al. 2021) (See Figure 8).

> *The steel support pedestal is welded to a stiffened base plate at its bottom. The base plate is attached to the reinforced concrete by anchor bolts. The base plate has shear bars on its underside to resist part of the lateral loads, including piping loads.*
>
> *Supports for the reactor vessel are individual air cooled rectangular box structures beneath the vessel nozzles bolted to the primary shield wall concrete. Each box structure consists of a horizontal top plate that receives loads from the reactor vessel shoe, a horizontal bottom plate which transfers the loads to the primary shield wall concrete, and connecting vertical plates. The supports are air cooled to maintain the supporting concrete temperature within acceptable levels.*

The technical drawings are not available, but the nozzle support description appears to be comparable to Farley's.

The transfer of horizontal seismic and postulated accident loads from the RPV and the connecting piping system into the concrete primary shield wall is performed through embedded steel structures. These structures consist of billet plates welded to vertical circular plates, anchored into the concrete wall by using anchor bolts and embedded structural steel assemblies. The gap between the vertical RPV supports and the horizontal RPV supports is shimmed in the cold condition with a predetermined allowance for thermal expansion.

2.2.5 Cantilever Beam System

Although decommissioned and dismantled, the Westinghouse-designed Trojan vessel support system provides an interesting design study that is possibly comparable to Davis-Besse's. It is composed of upper and lower beam structures joined by pinned columns (Figure 9). The lower beam is located closest to the core mid-plane, where the fast-neutron fluence is nearly at its maximum. The vertical short column is embedded in the concrete at a distance ranging from approximately 10 to 25 cm from the reactor cavity. This concrete region is susceptible to significant irradiation-induced damage.

According to Biwer et al. (2021), cantilever systems may also be located directly under the nozzle (**??**), thus avoiding the need for pinned short columns. Portions of such a support system remain in a region susceptible to high fast neutron fluxes.

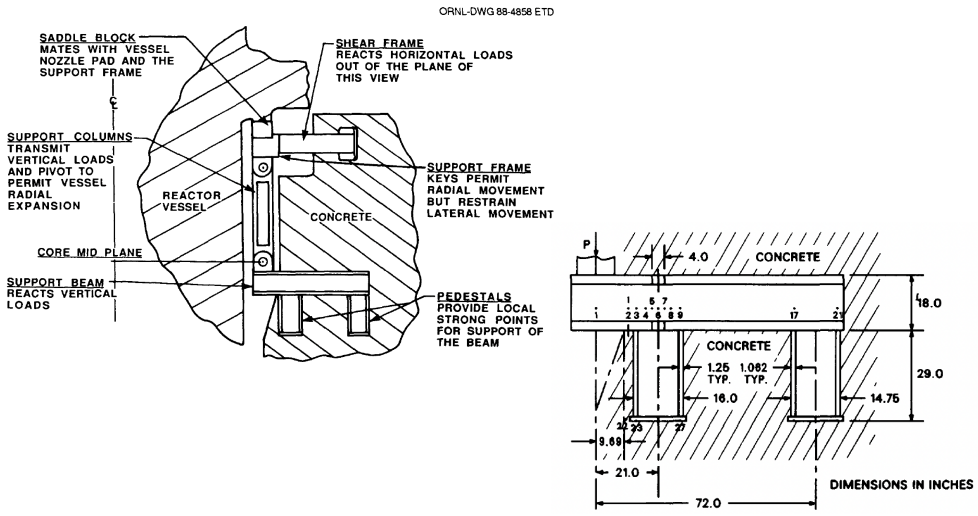

Figure 9. Radial section through Trojan reactor vessel supports showing principal structural and kinematic elements and details of the support beam (Cheverton et al. 1989).

2.2.6 Summary

Table 1 provides a summary of the RPV support system data collected by Biwer et al. (Biwer et al. 2021). The table is organized according to support categories: column, skirt, shield tank, cantilever brackets, and shoe. The estimated distance between the fuel's mid-core elevation and the support is also provided. This distance is reported as the core mid-plane distance (CMPD). It is expected that the concrete in the vicinity of the support will be more susceptible to irradiation-induced damage as the CMPD decreases. The different types of support are categorized according to the significance of possible irradiation-induced damage of the concrete in the vicinity of the support system.

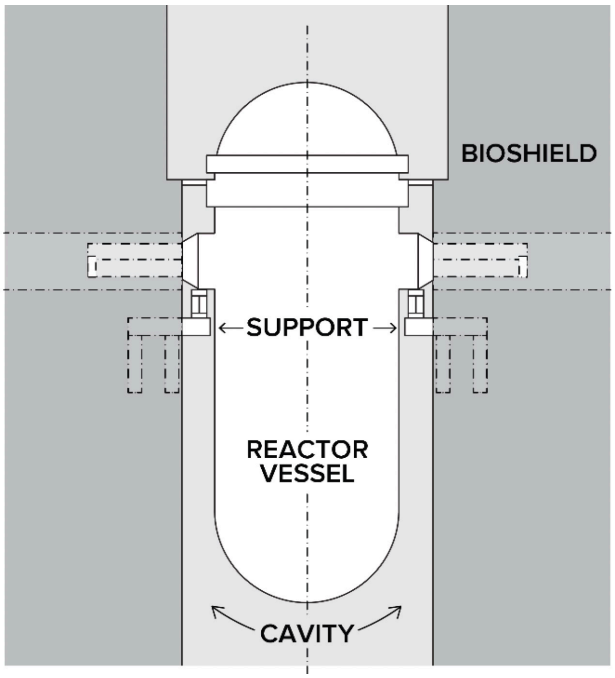

Figure 10. Schematics of a cantilever beam system directly located below the nozzle (Biwer et al. 2021).

Low Significance

Information collected on *base skirt supports* was limited. Most Babcock and Wilcox PWRs in commercial operation incorporate a support skirt design similar to that used for BWRs. It appears that all in-service and accidental loads are directly transferred to the concrete foundation through the base skirt assembly. This area, which is located directly under the RPV, receives irradiation doses lower than the estimated damage threshold. "72 equivalent full-power year (EFPY) fluence at the Oconnee Nuclear Station (ONS) RPV support embedment is estimated at 1.63×10^{18} n.cm^{-2} ($E > 0.1$ MeV) and gamma dose at 1.75×10^{9} rad. As such, the embedment concrete and grout are not susceptible to irradiation [damage]" (Framatome 2021).

When a neutron shield tank is present, it is expected that the fast neutron flux will be dramatically reduced, thus preventing any significant irradiation-induced damage to the CBS (Bruck 2018).

Moderate Significance

Column support-based systems rely exclusively on steel columns to transfer vertical loads to the foundation. The potential irradiation-induced degradation of the concrete surrounding the columns does not appear to affect their function. Lateral loads are transferred to the CBS wall through embedded horizontal brackets (e.g., Prairie Island) or anchors (e.g., Palo Verde – Arizona Public Service (APS)). Although this region is subject to lower fast neutron fluence, the anchor bond properties and the resistance of surrounding concrete may be affected by irradiation-induced damage.

High Significance

Support systems directly located under the nozzles include shoes resting on the CBS wall or a cantilever system embedded in the concrete. Some systems also include a ring girder located below the nozzle pads. The role of the ring girder in the distribution of vertical and horizontal loads from the RPV to the CBS has yet to be studied. Nevertheless, shoe-type and cantilever beam supports are essential for transferring both vertical and horizontal loads from the RPV to the CBS. The possible effects of irradiation on these systems require further study.

Table 1. Summary of RPV support configuration – simplified and reorganized by support types from Biwer et al. 2021

Design	Plant	Support types / numbers	CMPD
		Column supports	
WH (2-l.)	Point Beach (1,2)	6 (4 RPV nozzle / 2 RPV brackets), ring girder	12 ft
WH (2-l.)	Prairie Island	6 (4 RPV nozzle / 2 RPV brackets), ring girder, embedded column	n.a.
CE (2-l.)	ANO-2	3 RPV nozzle (2 inlet / 1 outlet)	6 ft
CE (2-l.)	Palo Verde 1–3	4 RPV nozzle (upper column attached to CBS for lateral support)	8.5–15 ft (lat. support – base)
WH (3-l.)	V.C. Summer 1	6 RPV nozzle, embedded steel beam and column assembly	0 ft
		Base skirt supports	
BW (2-l.)	ANO-1	base skirt	n.a.
BW (2-l.)	Oconnee (1,2)	base skirt	15 ft
BW (2-l.)	TMI 1	base skirt	13 ft
		Neutron shield tank (NST)	
WH (3-l.)	Beaver Valley (1,2)	6 RPV nozzle, shoe on NST / concrete skirt	6–31 ft (grout–c. skirt)
WH (3-l.)	North Anna (1,2)	6 RPV nozzle, shoe on NST / concrete skirt	31 ft (c. skirt)
WH (3-l.)	Surry (1,2)	RPV nozzle, shoe on NST / concrete skirt	31 ft (c. skirt)
		Cantilever brackets	
BW (2-l.)	Davis Besse	4 RPV inlet nozzle	2.3 ft
WH (3-l.)	Turkey Point (3,4)	Shoe supports sitting on embedded cantilevered steel beam and column assembly	0 ft
		Shoe resting on CBS	
WH (2-l.)	Ginna	6 (4 RPV nozzle / 2 RPV brackets)	3 ft
CE (2-l.)	Calvert Cliff (1,2)	3 RPV nozzle (2 inlet / 1 outlet), direct support on concrete	2.8 ft
CE (2-l.)	Palisades	3 RPV nozzle (2 inlet / 1 outlet), unclear config.	7.5 ft
CE (2-l.)	Millstone 2	3 RPV nozzle (2 inlet / 1 outlet)	n.a.
CE (3-l.)	St. Lucie (1,2)	3 RPV nozzle (2 inlet / 1 outlet). Pads on embedded horizontal beams	7.5 ft
CE (2-l.)	Waterford 3	4 RPV inlet nozzle. shoe support on embedded ring girder	3 ft
WH (3-l.)	J. Farley (1,2)	6 RPV nozzle, direct concrete support	7.5 ft
WH (3-l.)	H.B. Robinson 2	3 RPV alt. nozzle, direct concrete support	n.a.
WH (3-l.)	Shearon Harris	6 RPV nozzle, direct support on concrete	7.5 ft

BW - Babcock and Wilcox; CE - Combustion Engineering; WH - Westinghouse; 2/3-l - two/three-loop; CMPD - core mid-plane distance

2.3 DESIGN LOADS

The PWR vessel must be supported and restrained to withstand normal operating loads, seismic loads, and design basis accident loads, including those induced by postulated pipe ruptures such that which occurs in a LOCA. The support and restraint system should limit the movement of the vessel to within allowable limits under the applicable load combinations. For the primary shield wall, LOCA-related loads include differential pressure across the reactor cavity created by a pipe break near the reactor nozzles which acts either on the entire cavity or on portions of it.

2.3.1 In-Service Loads

In general, in-service normal loads include dead loads (D) such as those caused by the weight of the RPV resting on its support structure, live loads (L) such as those from an overhead or traveling crane, dead weight of equipment, piping, cable trays, and so on, (L') and water loads (F) from the refueling cavity. Irradiation-induced expansion is an additional loading scenario that was introduced recently in a structural performance analysis associated with license extension applications.

2.3.2 Accidental Loads

Accidental loads include hypothetical low-frequency earthquake loads generated by an operating basis earthquake (OBE) (E)[1] or a safe shutdown earthquake (SSE) (E')[2].

In addition to environmental loads, abnormal loads are generated by a postulated high-energy pipe break accident within the containment and/or compartment thereof. A LOCA falls under that category. During a LOCA event, the discharged pressurized water from a pipe break at a reactor vessel nozzle will result in three types of LOCA dynamic and transient loads acting simultaneously on the reactor vessel support and the primary shielding wall:

1. Temperature (T) and pressure (P) increase in the reactor cavity and the containment building
2. Jet thrust force at the break (M)
3. Forces from the differential pressure as the decompression wave travels through reactor internals (i.e., reactor internal LOCA blowdown loads) that do not affect the CBS

"The loading transients depend on the postulated break conditions, the postulated break locations, and on the operating conditions and geometry of the system." (Hosford et al. 1981)

These three loads must be combined with the load from the seismic event as part of the load combination in the licensing basis design.

Because of the coolant pressure, a LOCA is expected to produced higher transient and dynamic loading in a PWRs than in BWRs: "The overall safety significance is considered to be much less because of the lower operating pressures in primary systems in PWRs" [compared to that in BWRs.] (Hosford et al. 1981)

Pressurization and Heating of the Reactor Cavity

Pipe breaks at an RPV nozzle cause the release of steam into the annulus between the RPV and the CBS. Depending on the temperature of the steam and its cooling speed while being transported in the cavity, transient thermal loading and pressurization of the CBS wall may occur. In the report entitled "Assessment

1. An earthquake that could be expected to affect the site of a nuclear reactor but for which the plant's power production equipment is designed to remain functional without undue risk to public health and safety.
2. Maximum earthquake potential for which certain structures, systems, and components, important to safety, are designed to sustain and remain functional.

of the Effect of the In-Service Irradiation-Induced Degradation on the Structural Performance of Biological Shields during a Loss of Coolant Accidents" (ORNL/SPR-2023/3158), it is approximated that the released steam would uniformly fill the annulus, thus producing time-dependent temperature and pressure that is uniformly applied to the inner surface of the CBS. NUREG-0609 suggests that the asymmetry of the break may create differential pressure and temperature in the annulus between the closest and farthest locations from the break, as shown in Fig. Figure 11. Under these conditions, the inner surface of the CBS is thus subject to a thermal “shock,” potentially causing concrete dehydration, water vaporization, and restrained thermal expansion–induced stress of the concrete region that was previously damaged by in-service irradiation.

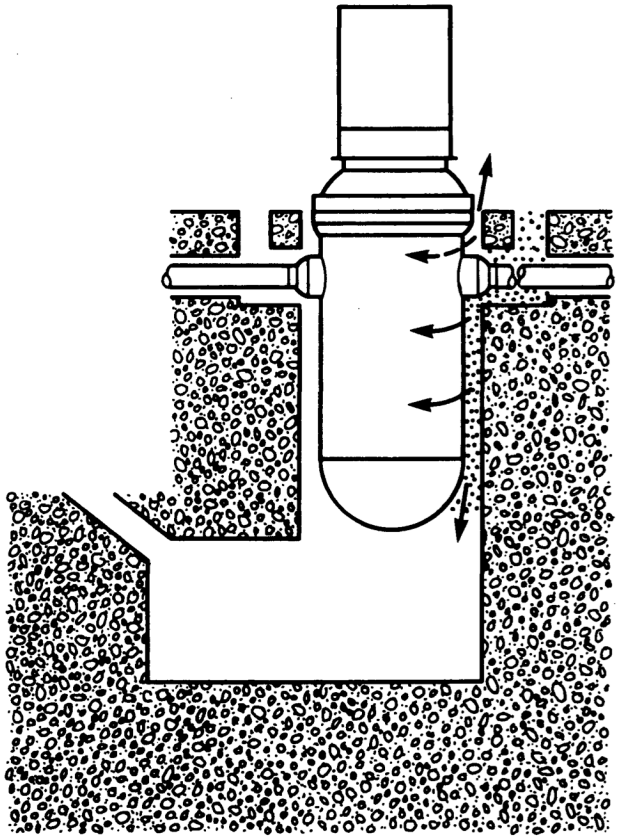

Figure 11. Pressurization of reactor annulus per NUREG-0609 (Hosford et al. 1981).

Subcooled Blowdown Loads

> *As coolant discharges from the pipe break, a depressurization wave will travel from the break point into the vessel, causing unbalanced loads in the RPV and its internals. These loads are called LOCA blowdown loads. As this decompression wave enters the reactor vessel and travels down the vessel-to-barrel annulus [see Figure 12], it will cause the core barrel to deflect sideways toward the side of the decompression wave due to differential pressures acting on the two sides of the core barrel. This sideways deflection of the core barrel will create horizontal and vertical compressive forces on the reactor vessel supports and reactor internals. Such transient differential pressures, although of short duration, could place a significant load on the reactor vessel supports and reactor internals* (Biwer et al. 2021).

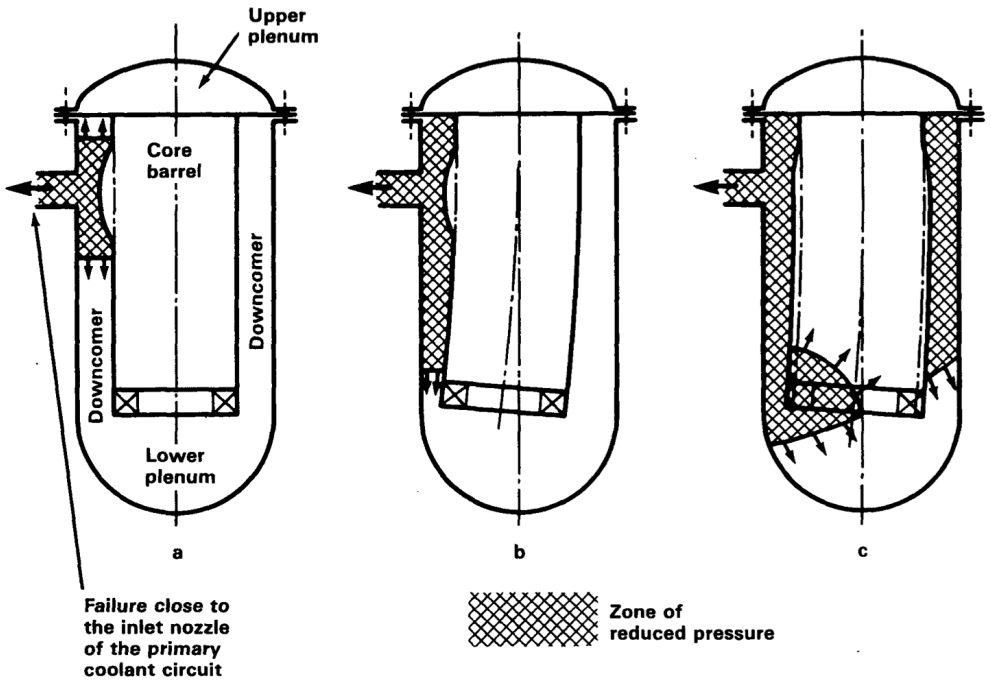

Figure 12. Example of asymmetrical internals load from NUREG-0609 (Hosford et al. 1981).

Jet Thrust

At the pipe break location, a steam and water mixture is expelled, creating an axial thrust force that acts on the pipe. For PWRs, these breaks could be on the order of 75 cm (30 in) in diameter. The resulting jet will impinge on nearby structures, potentially creating horizontal and vertical forces on a reactor vessel support. Figure 13 shows the pipe jet thrust load acting on the reactor vessel and the reactor vessel supports at the location of the pipe break.

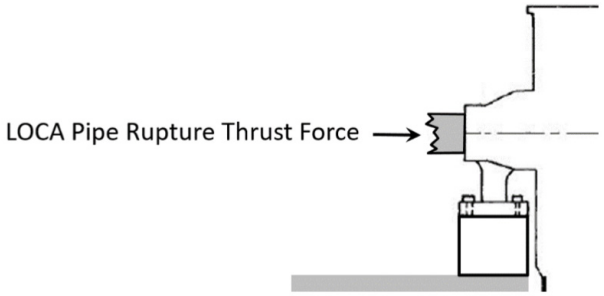

Figure 13. LOCA pipe rupture thrust force from NUREG-0609 (Biwer et al. 2021).

3. SIMULATIONS OF ACCIDENTAL CONDITIONS DURING LOCA

3.1 INTRODUCTION

To calculate the generic reactor cavity over-pressurization as a consequence of a LOCA, a RELAP5-3D system thermal-hydraulic code model of a generic three-loop PWR reactor cavity has been developed. This model is coupled with a complete primary and secondary side model of the PWR. The scope of this model development is as follows:

- To calculate, with a sufficient degree of resolution and accuracy, the pressure wave propagation in the reactor cavity and the neighboring reactor compartments;
- To provide the boundary conditions (pressure and temperature distributions at the break) for evaluating the jet impingement forces;
- To serve as a tool for performing fast sensitivity and uncertainty analyses on the main parameters involved in the phenomena representation.

In the next subsection, a brief description of the RELAP5-3D code capabilities and the rationale for its selection are provided, followed by a description of the PWR reactor cavity model developed for this project. Results of the large and medium size breaks LOCA calculations are then presented in the following subsection.

3.2 RELAP5-3D CODE AND RATIONALE FOR THE CODE SELECTION

The selected tool for the system's thermal-hydraulic analysis, including the reactor cavity over-pressurization analysis, is the Idaho National Laboratory (INL) RELAP5-3D code (Team 2018a). RELAP5-3D was developed under the sponsorship of the US Department of Energy (DOE), the NRC, members of the International Code Assessment and Applications Program (ICAP), members of the Code Applications and Maintenance Program (CAMP), and members of the International RELAP5 Users Group (IRUG). RELAP5-3D can simulate transients in LWR systems such as loss of coolant, anticipated transients without scram (ATWS), and operational transients like loss of feedwater, loss of offsite power, station blackout, and turbine trip. A key feature for this project is RELAP5-3D's capability to model 3D thermal hydraulics through dedicated 3D hydraulic components. This multidimensional simulation capability allows the user to more accurately model the multidimensional flow behavior that can be exhibited in any component or region of an LWR system.

A postulated instantaneous double-ended break of an RPV nozzle or of a hot leg or cold leg is an event that introduces asymmetric mass flows, temperature, and pressure distributions in the containment compartments (Hosford et al. 1981). Therefore, 3D thermal-hydraulic modeling capability is needed. RELAP5-3D allows the user to divide the analyzed system into several control volumes which are then connected by zero-dimensional junctions. Thus, a "nodalization" of the system is developed by the analyst. Non-equilibrium, two-phase, two-component (water and steam/non-condensable gases) equations for mass, momentum, and energy are solved, thus determining the main thermal-hydraulic parameters for each volume and junction as a function of time. Dedicated closure relations and special models allow for simulation of complex two-phase thermal-hydraulic phenomena such as critical flow, critical heat flux, and counter-current flow limitation.

Because the main objective of this project is to determine concrete degradation around the RPV, a 3D model of the reactor cavity was created using the RELAP5-3D "multid" hydraulic component.

3.3 GENERIC 3-LOOP PWR AND RELAP5-3D NODALIZATION

In this subsection, the main public information retrieved from the NRC library for a generic 3-loop PWR cavity is presented. The developed RELAP5-3D model is also described, with key modeling choices and parameters highlighted.

Different versions of reactor containment designs reflecting the evolution of PWR systems are considered. For this reactor cavity analysis, most of the data are consistent with the design data of H.B. Robinson Unit 2, a Westinghouse post-tensioned concrete large dry containment (see Figure 14 and Figure 15).

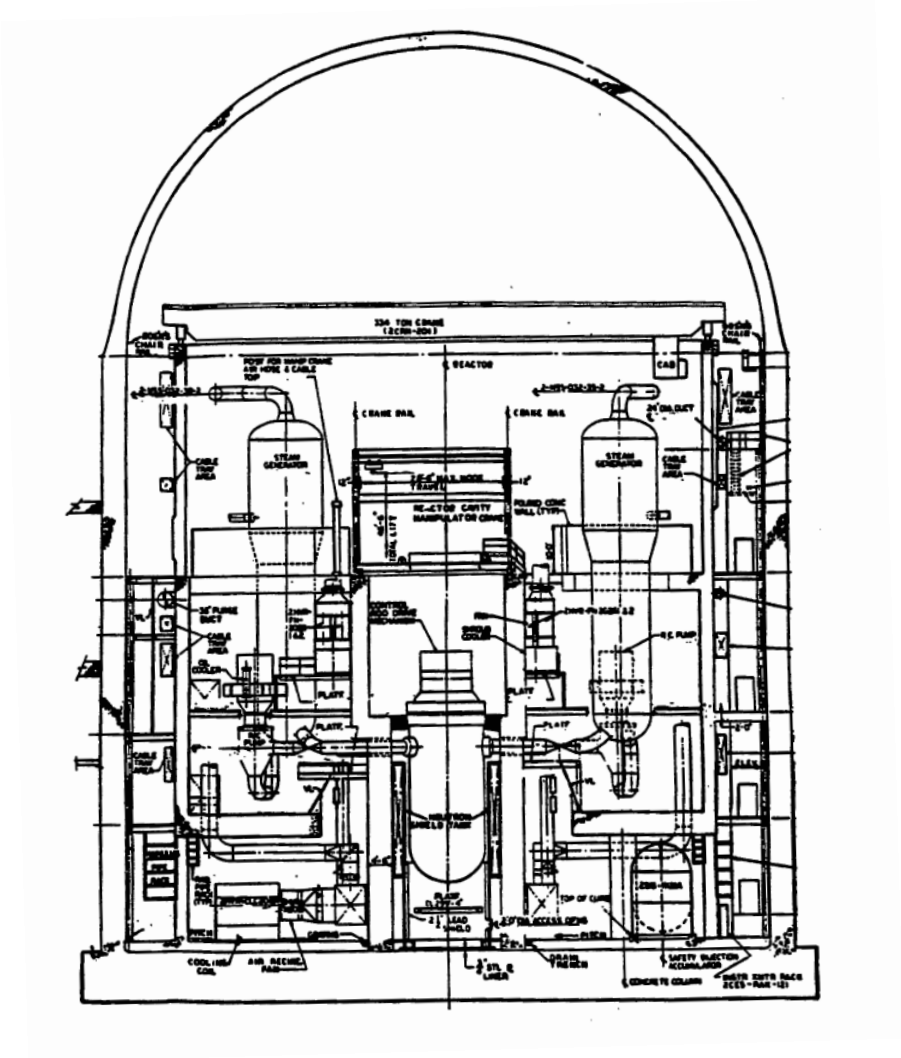

Figure 14. Cross section of 3-loop Westinghouse PWR containment building (Lobner, Donahoe, and Cavallin 1990).

As can be seen in Figure 14, the RPV is located in an annular compartment (reactor cavity) for which the boundaries are defined by the thick biological shield walls on the sides, the reactor foundation slab on the bottom, and the refueling cavity on the top. Figure 14 also shows a neutron shield tank in the reactor cavity. This component was not considered in the modeling for this work because most of the retrieved data pertain to the H.B. Robinson nuclear power plant, which does not include neutron shield tank ((Energy 2017)). The presence of a neutron shield considerably attenuates the irradiation dose in the CBS, making the plant

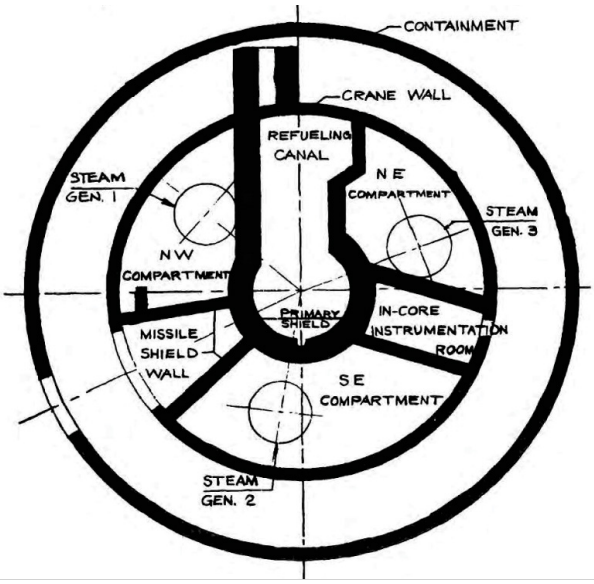

Figure 15. PWR three-loop reactor building compartments (Energy 2017).

design less susceptible to irradiation-induced damage.

Penetrations for the hot and cold legs connect the reactor cavity with the steam generator compartments, whereas other openings guarantee connection with the refueling cavity, the lower compartment, and the residual heat removal system room. Connections between the different containment compartments for another 3-loop Westinghouse plant, the Beaver Valley Nuclear Power Plant, are shown in the figures below. These figures represent a containment nodalization for the MAAP severe accident analysis code (Beaver Valley Power Station 2014). Information reported in these figures (e.g., compartment connection flow areas, volumes) has been used to supplement the missing data for defining the reference reactor cavity geometry for a 3-loop Westinghouse plant.

Further information about the reactor cavity configuration was gathered from Basta (2023), Simpson (2023), and Smith (2023). Relevant information used for the model development is presented in the following figures and tables.

Based on the retrieved information, it can be observed that the RPV is tightly confined within the reactor cavity. The gap between the RPV insulation and the CBS wall is 8.2 cm (0.268 ft) wide, or 17.1 cm (0.561 ft) wide if the RPV insulation is not considered. The RPV support system is located in dedicated niches of the CBS wall (see Figure 20). The main parameters derived from the open literature review are reported in Table 2. The containment atmosphere has been modeled as air with zero relative humidity at about 1 atm pressure (14.7 psi) and 20 °C.

The RELAP5-3D model was developed by combining an existing nodalization of the H. B. Robinson Nuclear Power Plant (Don Fletcher, Davis, and Ogden 1985) with a new 3D model of the reactor cavity and the containment. The main characteristics of this new part of the RELAP5-3D nodalization are reported in the following figures and tables. The reactor cavity's annular space below the nozzle line was modeled using a single "multid" component (component 50) which is connected at the bottom via multiple junctions to another multid component that models the bottom of the reactor cavity (component 48). The top part of component 50 is connected via multiple junctions to another multid component modeling the RPV nozzle zone (component 52), which includes the cold leg and hot legs. This component is connected at

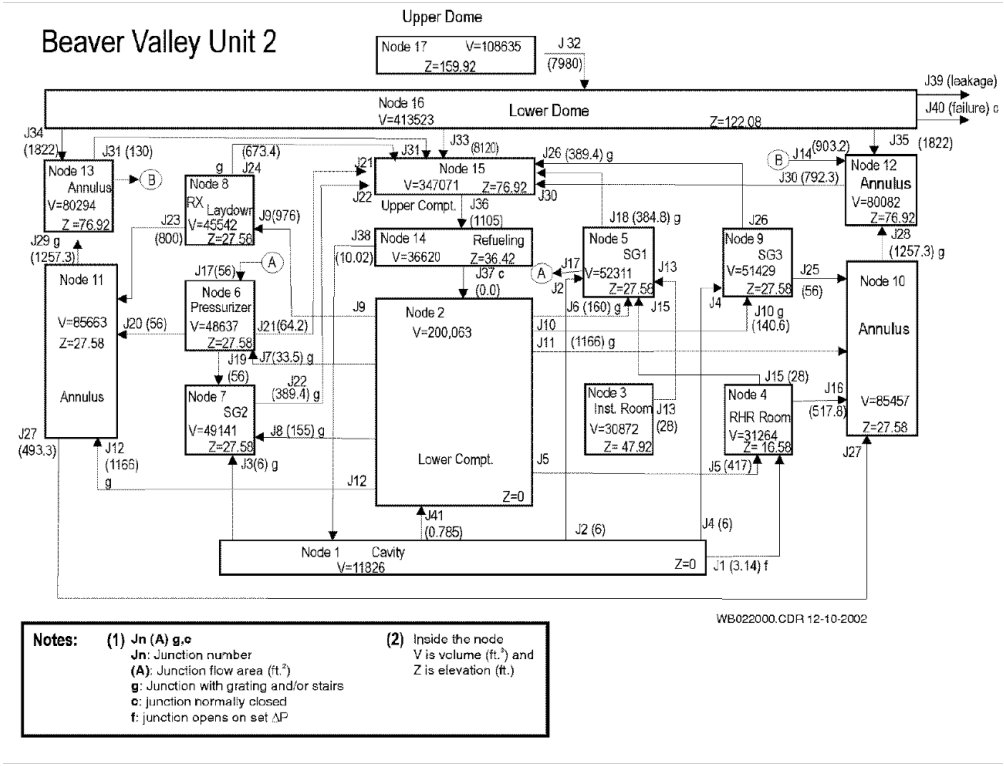

Figure 16. Example of 3-loop containment nodalization (Beaver Valley Power Station 2014).

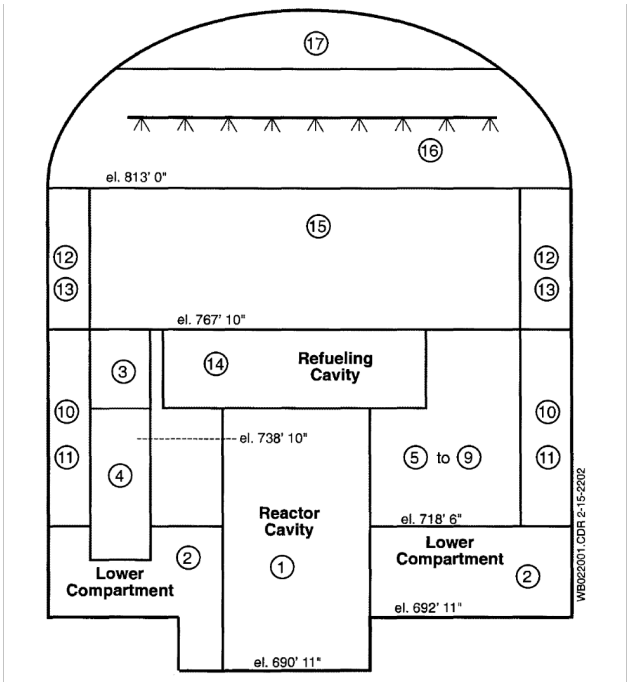

Figure 17. Containment nodalization layout, front view (Beaver Valley Power Station 2014).

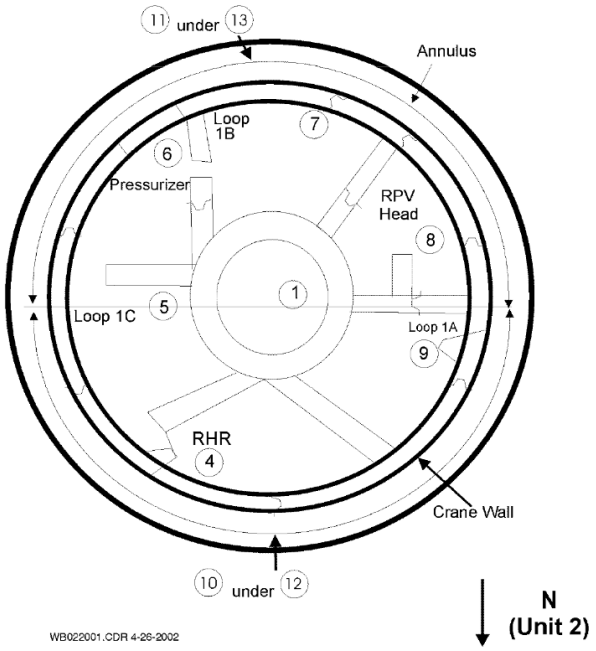

Figure 18. Compartment nodalization layout, top view (Beaver Valley Power Station 2014).

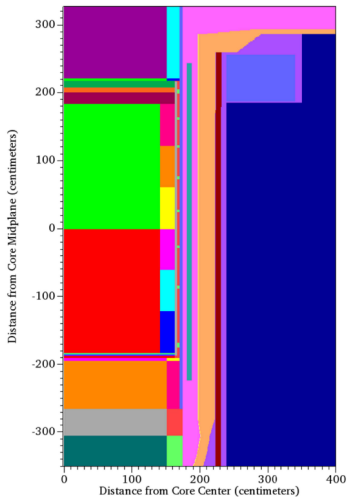

Figure 19. RPV geometry (Smith 2023).

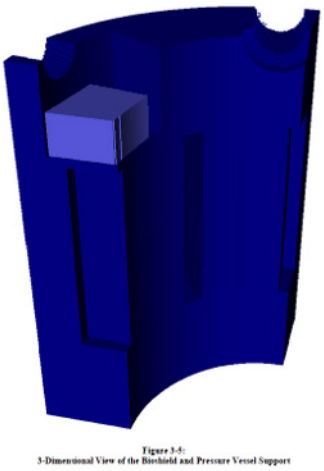

Figure 20. Cavity geometry (Smith 2023).

Table 2. Main parameters used for reactor cavity modeling

Parameter	**Value (SI)**	**Value (Imperial)**
Reactor cavity gap (RPV OR to CBS IR)	0.171 m	0.561 ft
Effective reactor cavity gap (RPV insulation OR to CBS IR)	0.082 m	0.268 ft
RPV cylindrical part height below the nozzles	5.400 m	17.717 ft
RPV lower plenum height	1.750 m	5.736 ft
CBS thickness	1.612 m	5.290 ft
Bottom reactor cavity height	3.250 m	10.666 ft
Bottom reactor cavity diameter	5.020 m	16.484 ft
Refueling cavity height	6.500 m	21.330 ft
RPV nozzle zone height	2.301 m	7.551 ft
Cold leg diameter	0.699 m	2.292 ft
Flow area between RPV cavity and SG compartments	1.690 m^2	3.14 ft^2
Flow area between RPV cavity and RHR room	0.290 m^2	18.1 ft^2
Reactor cavity net free volume	335 m^3	1.18×10^4 ft^3
Refueling cavity net free volume	1,037 m^3	3.66×10^4 ft^3
Containment net free volume	57,000 m^3	2.01×10^6 ft^3

the top to multid component 54, which models the reactor refueling cavity, and it is connected on the radial periphery to one-dimensional components (branches) modeling the tunnels for the cold legs and hot legs. Components 54 and 48 are connected via a junction to the other components modeling the other parts of the containment (Components 232–235). The branches modeling the tunnel for the cold legs and hot legs (Components 236–239, 244 and 245) are connected to the volumes modeling part of the containment (Branch 233) via dedicated junctions. Using this modeling strategy, the main flow path for the two-phase flow resulting from a cold or hot leg break is identified. Two-phase coolant from the RPV break can be directly discharged through dedicated break-valves (components 242 and 243) simulating the cold or hot leg break. Component 221 (valve) is open during normal operation to provide continuity between the two cold or hot leg parts (e.g., pipe components 220 and 222) and closed during a LOCA simulation. The containment and the break schematics are represented in Figure 21 and Figure 22, respectively.

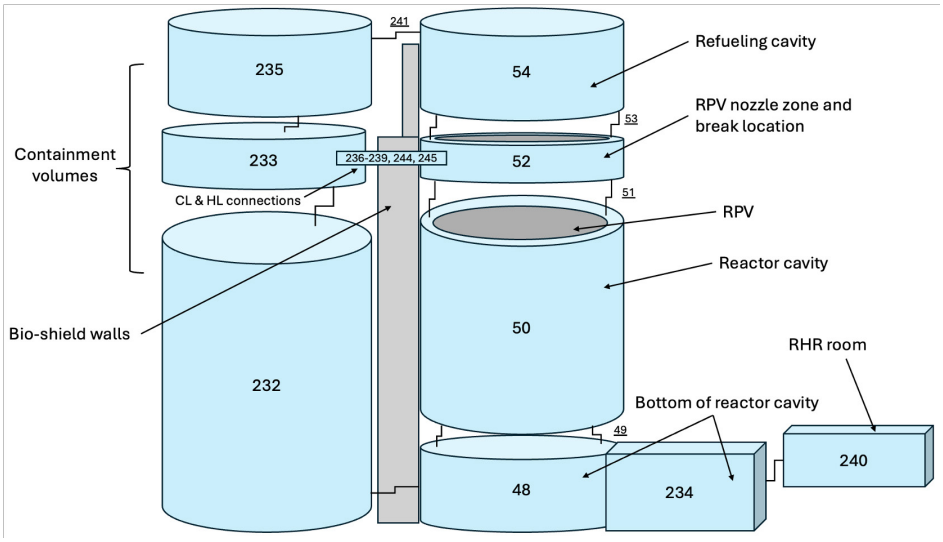

Figure 21. RELAP5-3D reactor cavity and containment nodalization.

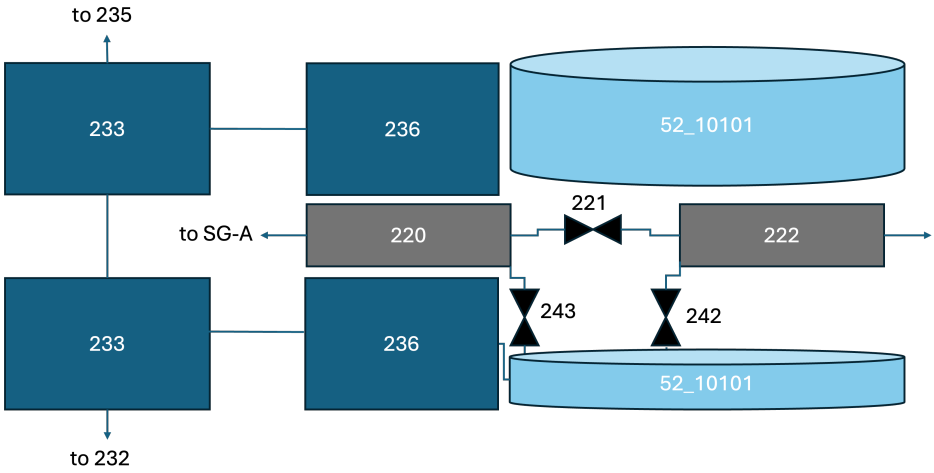

Figure 22. RELAP5-3D cold leg A break nodalization.

Details of the 3D component meshing is reported in Table 3. Uniform azimuthal meshing has been used (30 degrees per mesh, see Figure 23), and the axial and radial meshing has been chosen to match the main

dimensions of the geometry (cavity thickness, RPV height, etc.).

Table 3. 3D component meshing characteristics.

Modeled part	Component ID number	Radial mesh	Azimuthal mesh	Axial mesh
Lower part of reactor cavity	48	4	12	5
Reactor cavity	50	1	12	7
RPV nozzle section	52	1	12	5
Refueling cavity	54	9	12	7

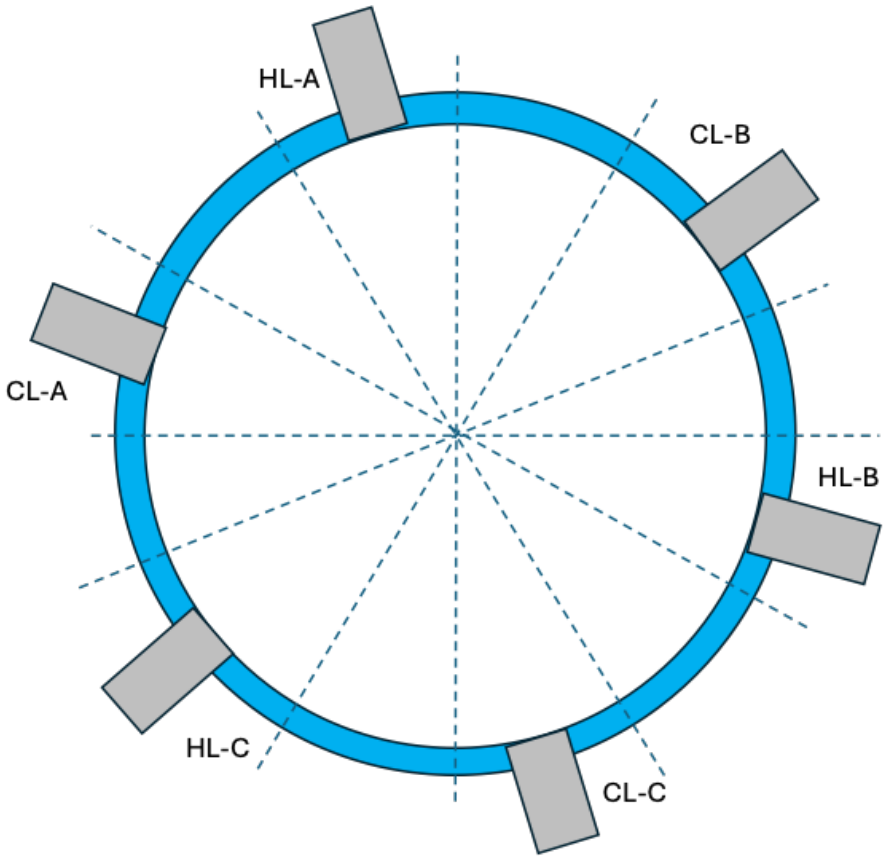

Figure 23. Azimuthal discretization of the reactor cavity.

The primary and secondary sides of the RELAP5-3D nodalization are presented in Figure 24, Figure 25, and Figure 26.

3.4 LOCA RESULTS

In this subsection, the results of the main thermal-hydraulic outputs obtained from the RELAP5-3D simulations for an instantaneous double-ended guillotine break (DEGB) and for 1A (where A is the flow area of a cold leg) of cold leg A are reported. These events are referred to as leg break loss-of-coolant accident (LBLOCA). The main output parameters investigated include the pressure evolution in the reactor cavity, the differential pressures between the different zones and elevations of the reactor cavity, the temperature distributions, and the jet impingement force. The jet impingement force was calculated according to ANS guidelines (Society 1988) using the formula presented in Eq. (1):

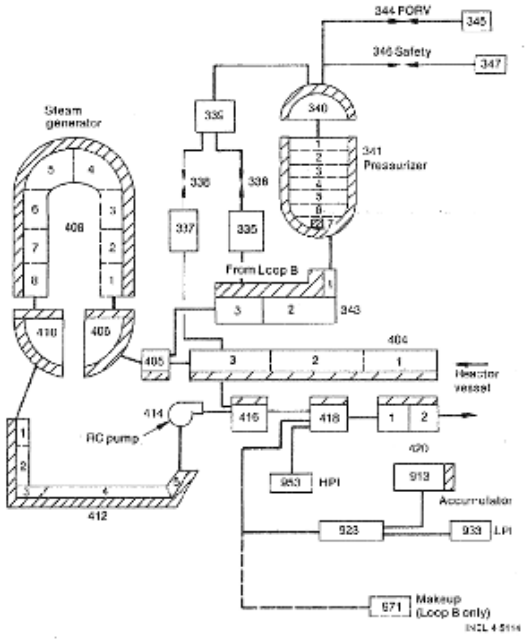

Figure 24. RELAP5-3D primary side nodalization.

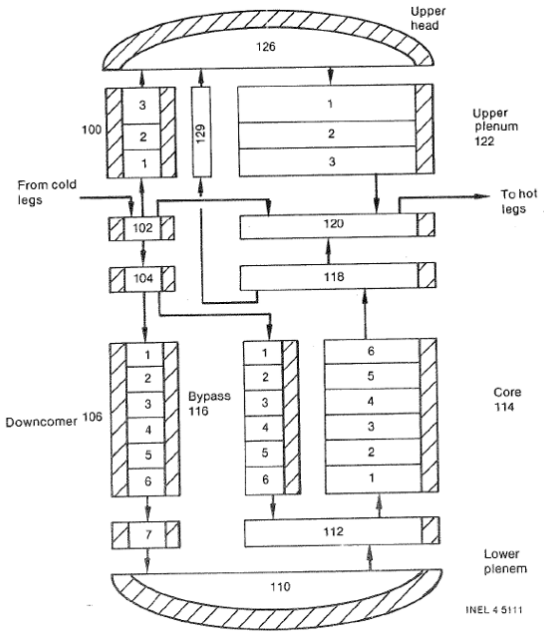

Figure 25. RELAP5-3D RPV nodalization.

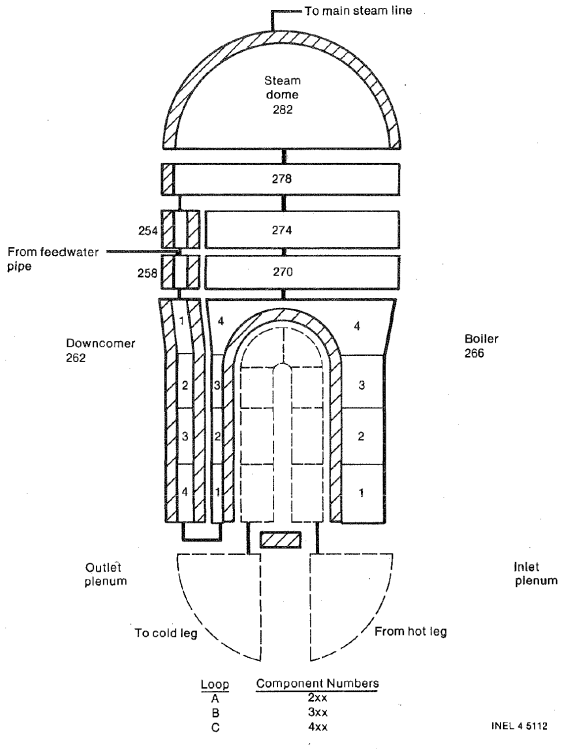

Figure 26. SG secondary side nodalization.

$$F_b = G_e^2 A_e / \varrho_e g_c + A_e(P_e - P_{amb}), \tag{1}$$

where G_e is the mass flux, A_e is the break area, ϱ is the fluid density, g is gravitational constant, P_e is the pressure at the break plane, and P_{amb} is the compartment pressure.

3.4.1 2A LOCA

In the DEGB LBLOCA, the break valves open at time $t = 0$, causing an immediate pressurization of the reactor cavity (see Figure 27 and Figure 28). The pressure wave propagates in both azimuthal directions around the RPV, resulting in a pressure spike on the opposite side of the ruptured nozzle (HL-B location).

The pressure immediately spikes in the annular space below the RPV nozzles (see Figure 29). Some small delays are observed at different azimuths and elevations (see Figure 30).

Pressure spikes in the lower part of the reactor cavity, located below the RPV, and in the refueling cavity are significantly reduced (see Figure 31). In this simulation, the containment pressure reaches an asymptotic value because the containment fan coolers, spray system, and passive heat structures are not modeled (see Figure 32).

The differential pressure around the RPV-nozzle zone is maximum during the first ten seconds of the transient, reaching peak values of about 33 bars (see Figure 33) in the studied scenario. This is the result of the propagation of the pressure wave in the azimuthal direction from both sides of the RPV. Differential pressure at lower elevations (e.g., in the annular space of the reactor cavity) is much lower, as shown in Figure 34. Differential pressure between the CBS wall and the remainder of the containment peaks at approximately 40 bars during the first ten seconds (see Figure 35).

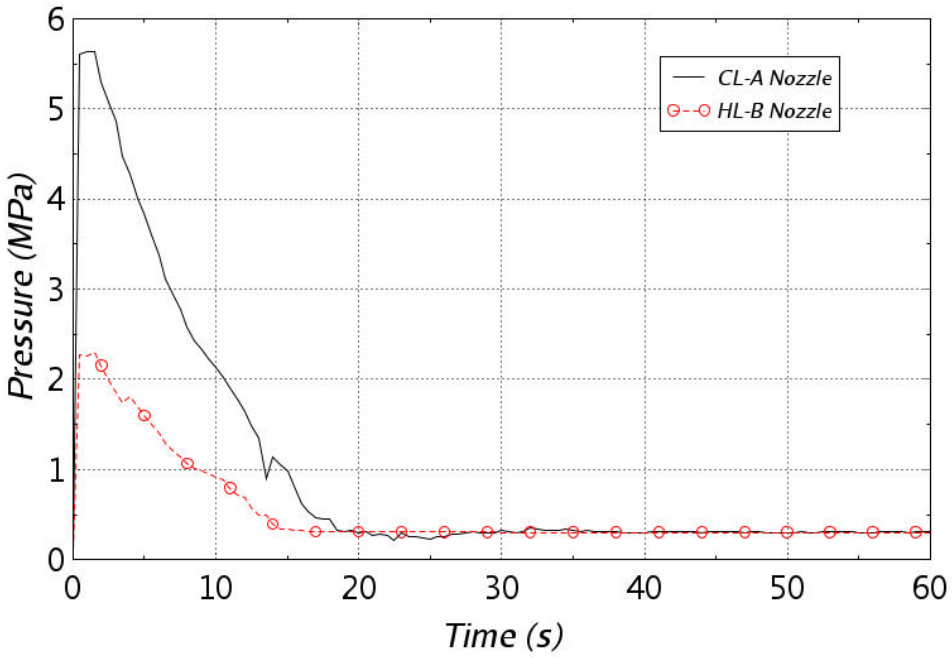

Figure 27. Pressure in the RPV nozzle zone - 2A DEGB case.

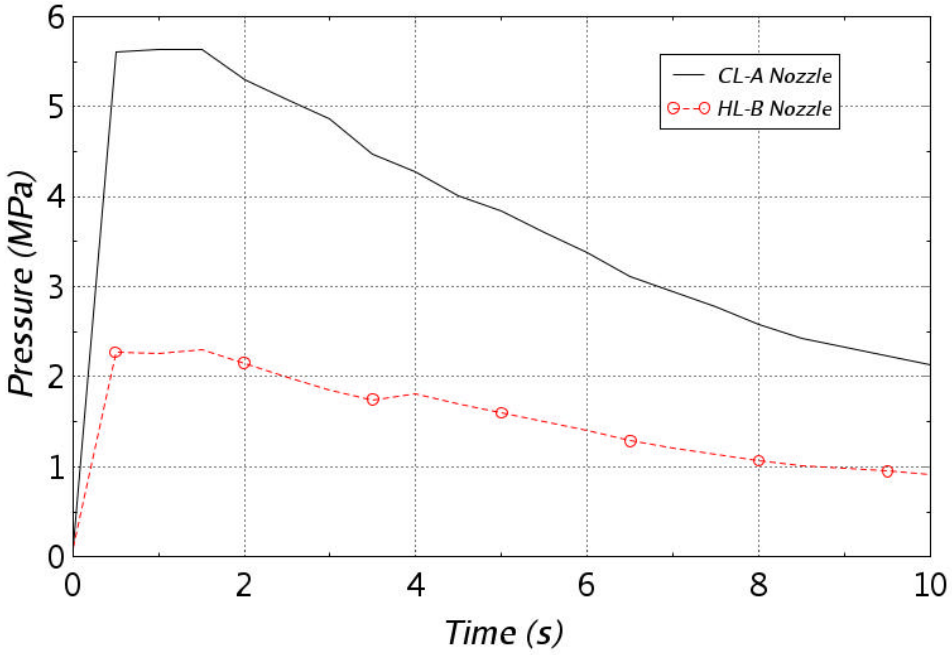

Figure 28. Pressure in the RPV nozzle zone, first ten seconds - 2A DEGB case.

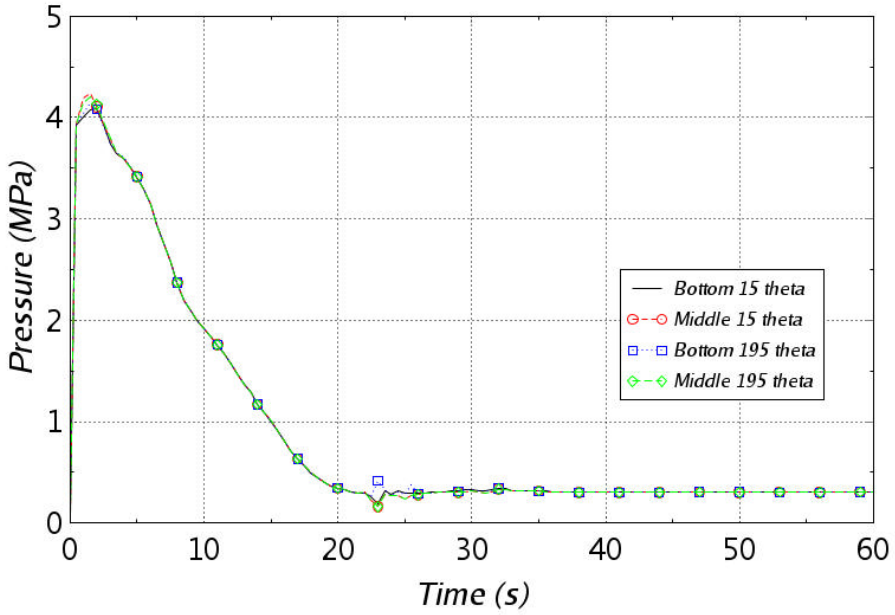

Figure 29. Pressure in the annular cavity zone - 2A DEGB case.

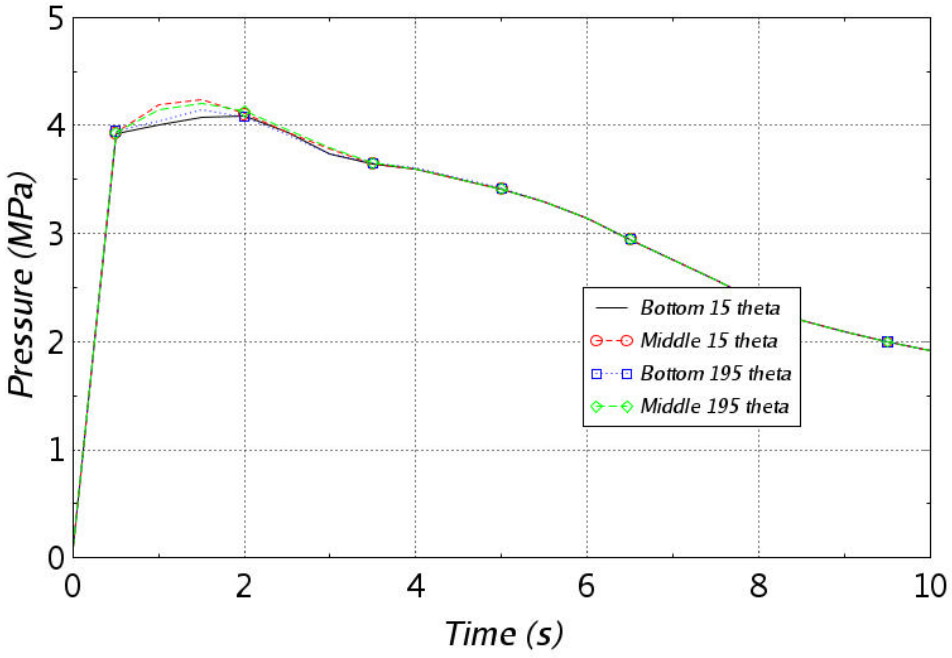

Figure 30. Pressure in the annular cavity zone, first ten seconds - 2A DEGB case.

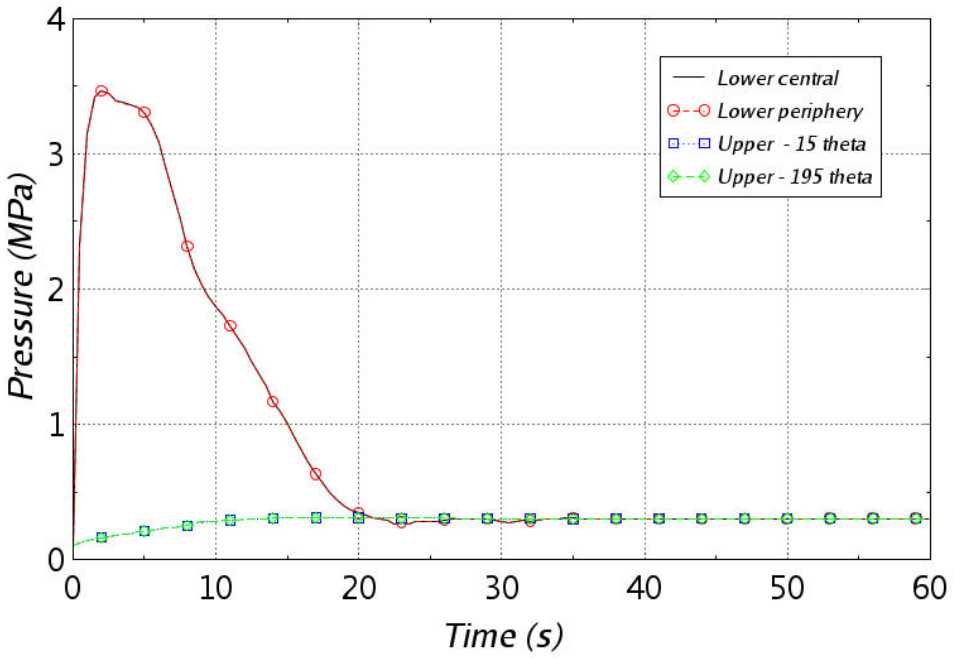

Figure 31. Pressure in the lower part of reactor cavity and in the refueling cavity - 2A DEGB case.

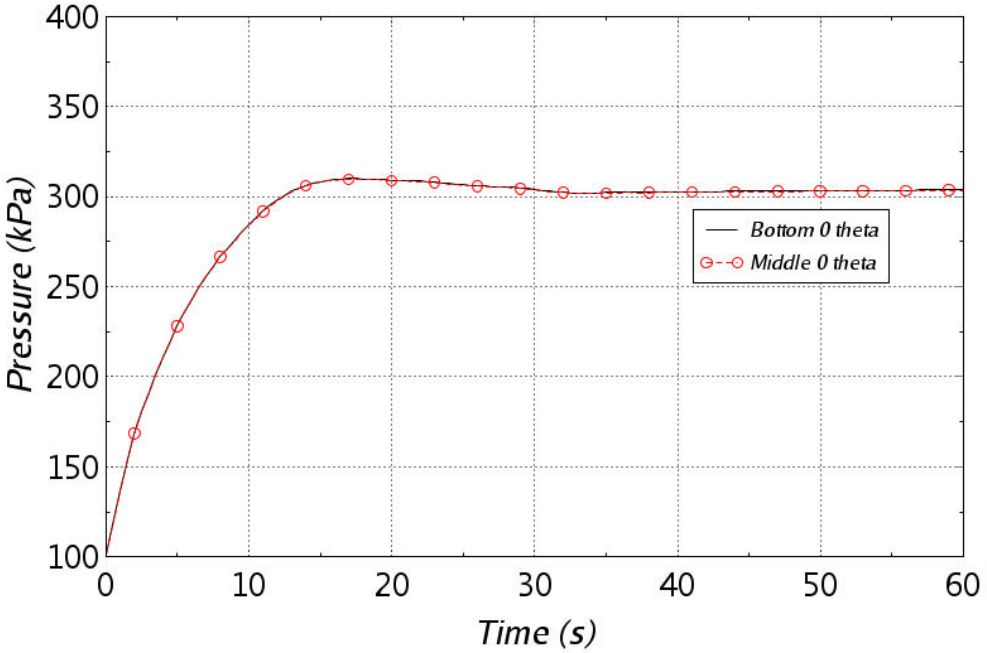

Figure 32. Containment pressure - 2A DEGB case.

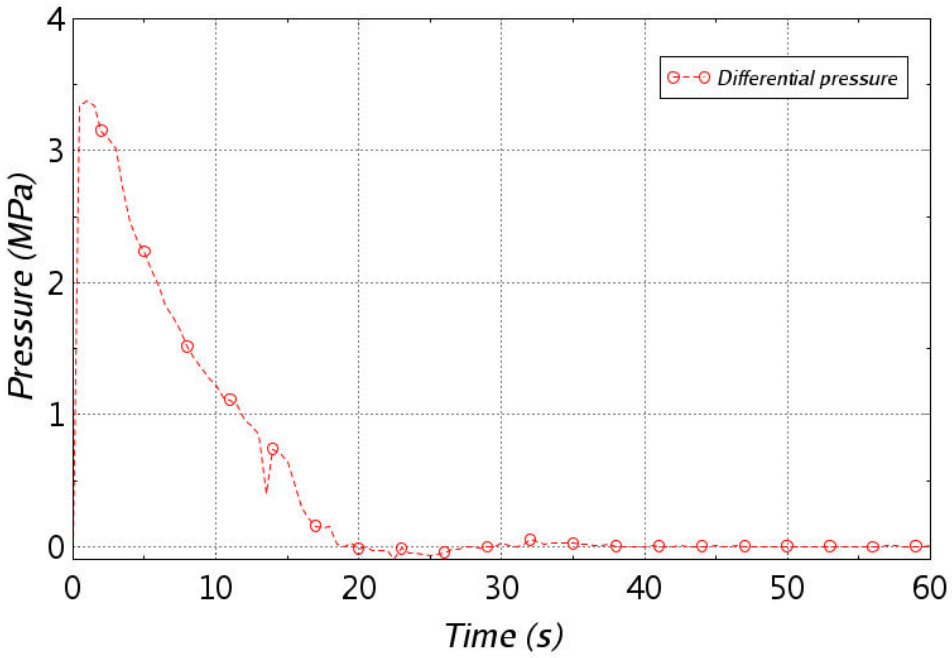

Figure 33. Differential pressure in the RPV nozzle zone - 2A DEGB case.

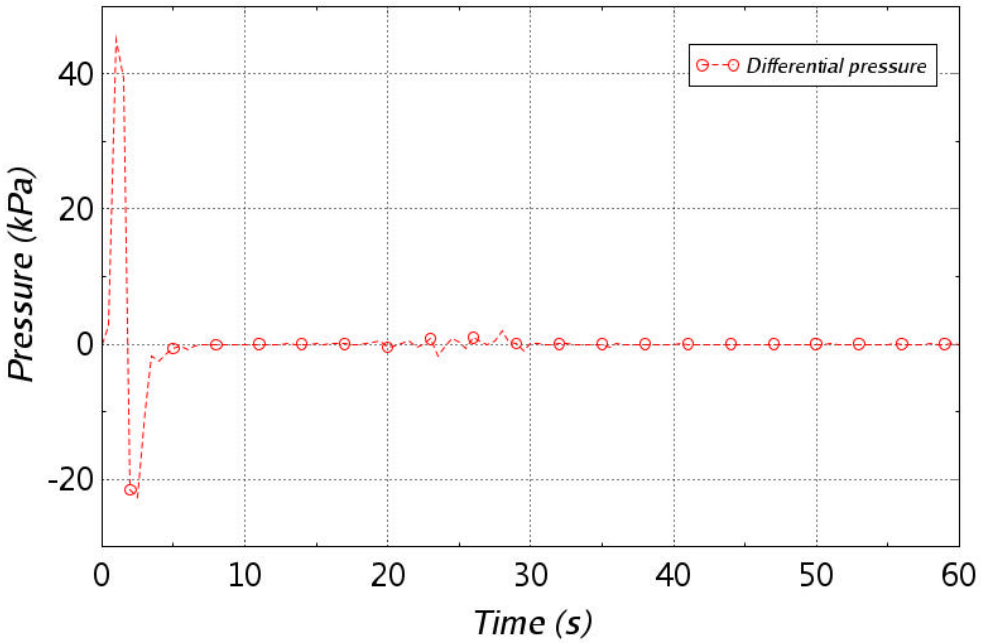

Figure 34. Differential pressure in the annular zone of reactor cavity - 2A DEGB case.

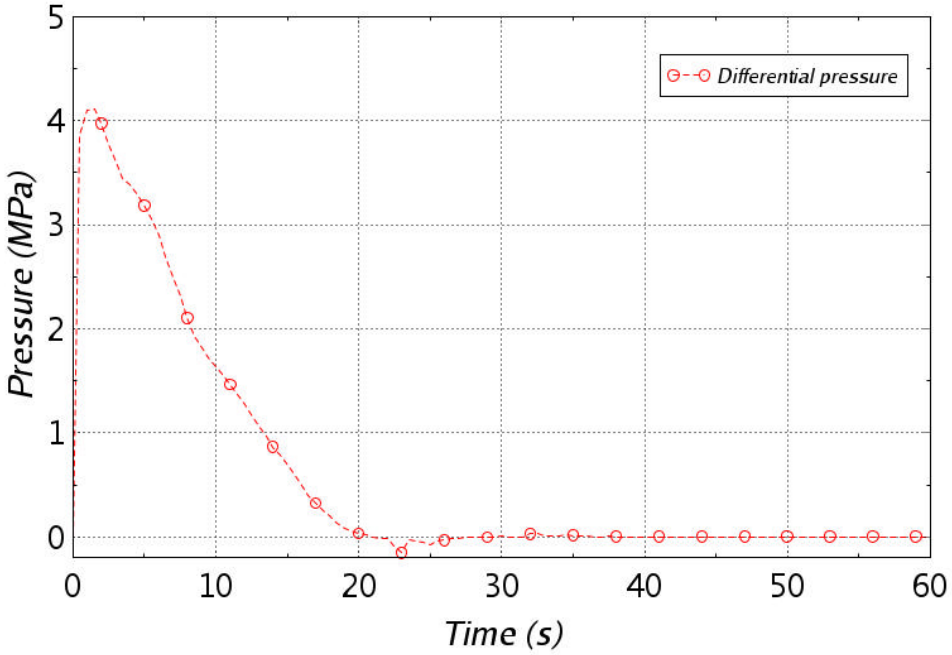

Figure 35. Differential pressure across the CBS wall - 2A DEGB case.

Finally, temperature evolution of the different modeled volumes of the reactor cavity and the containment are presented in Figure 36. Mass flows at the break and the jet impingement force are shown in Figure 37 and **fig:R5_JIF_2A**. Containment atmosphere is overheated over the short term by the discharge of high-enthalpy fluid from the primary side. Jet impingement force is approximately 6.03 MN.

3.4.2 1A LOCA - REFERENCE CASE

Main results from an instantaneous 1A break of cold leg A are reported below. In this case, a single break valve on cold leg A was open at $t = 0$, discharging the two-phase flow into the RPV cavity. 1A LOCA is considered the reference case for this study. The pressure trends are similar to those observed in the DEGB LOCA, with pressure spikes in the RPV nozzle and the annular zone reduced from 5.5 MPa to 5 MPa (see Figure 39 and Figure 40).

Differential pressures across the RPV and the CBS wall remain high but are lower compared to the DEGB case (see Figure 41, Figure 42, Figure 43). Temperature trends and jet impingement force are also similar to 2A DEGB case, as expected (see Figure 44 and Figure 46).

3.5 SENSITIVITIES ON 1A LOCA CASE

In this section, sensitivities on the 1A LOCA calculations are reported. The first sensitivity concerns the use of a different two-phase critical flow model. The reference case uses the default RELAP5-3D standard two-phase critical flow model, or the Ransom-Trapp model (Team 2018b). The first sensitivity calculation was run by using the Henry-Fauske (HF) model (Team 2018b) with discharge coefficients typical for nozzles. The second sensitivity was run by changing the break location in the cavity: that is, by modeling a 1A break on hot-leg B (the loop with the pressurizer) instead of cold-leg A. Results are reported in the table

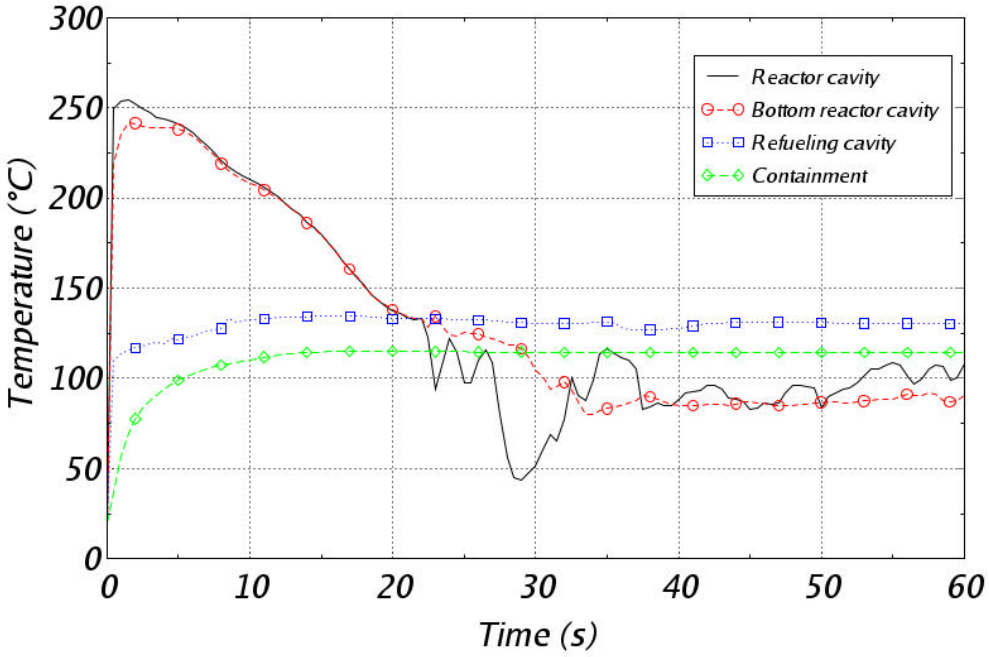

Figure 36. Reactor cavity zones and containment temperature trends - 2A DEGB case.

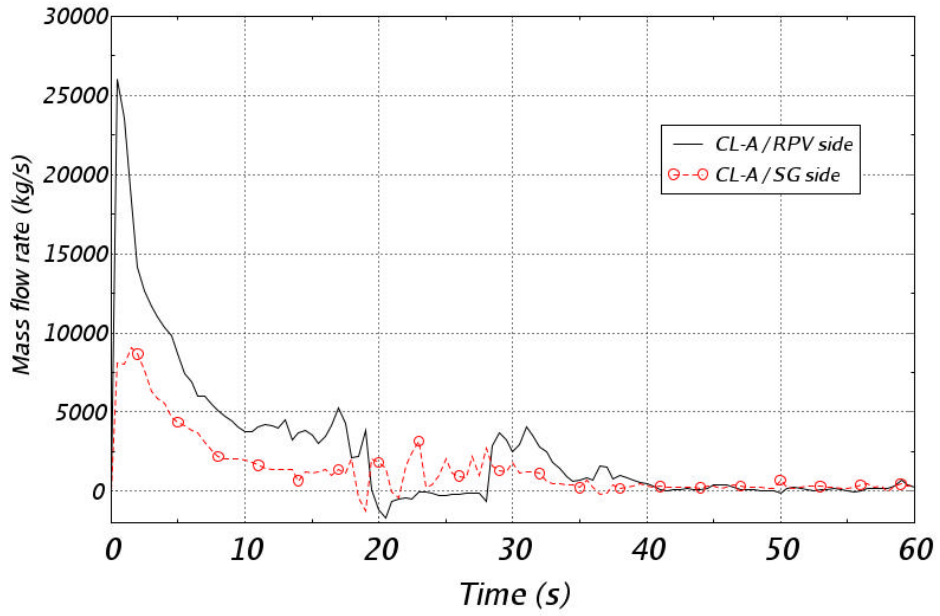

Figure 37. Mass flow at the breaks - 2A DEGB case.

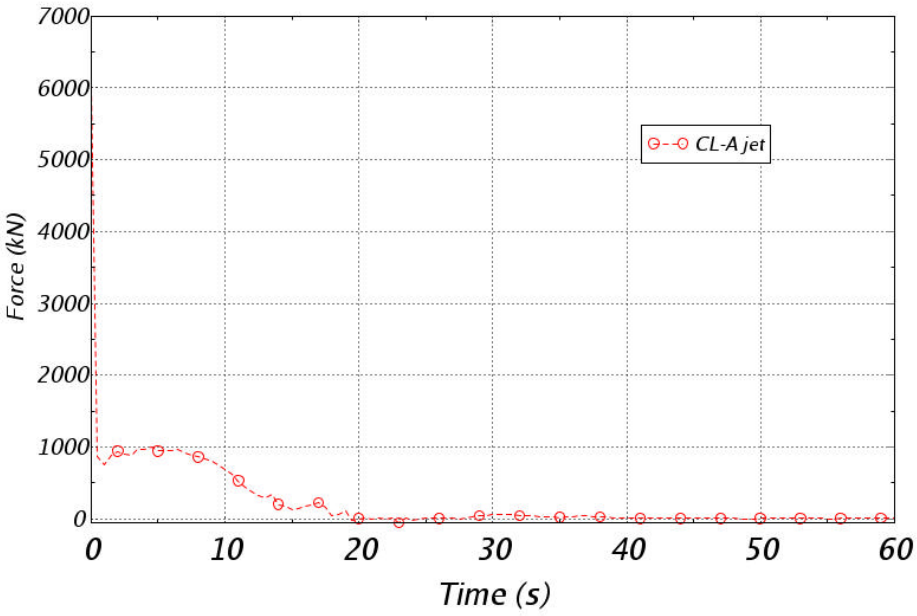

Figure 38. Jet impingement force - 2A DEGB case.

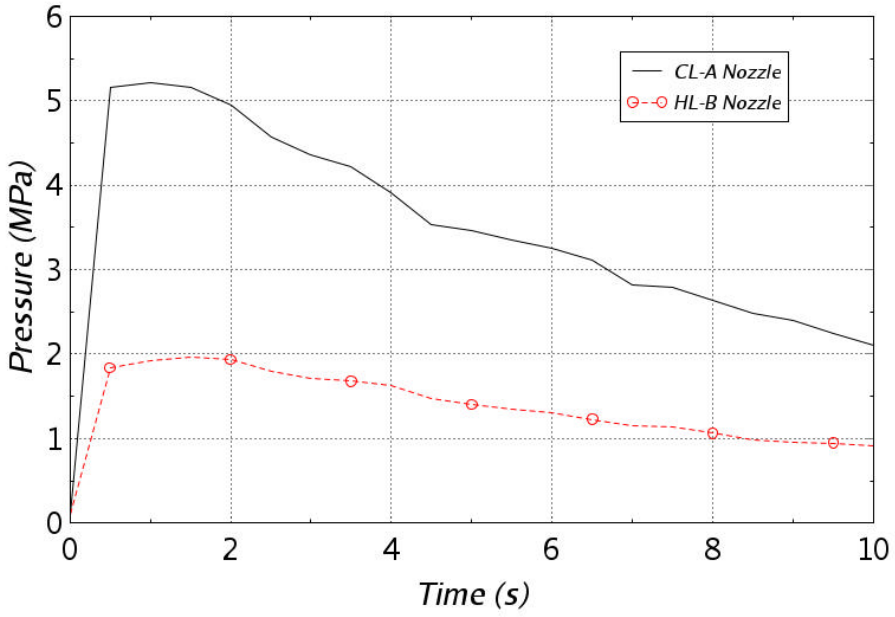

Figure 39. Pressure in the RPV nozzle zone, first ten seconds - 1A reference case.

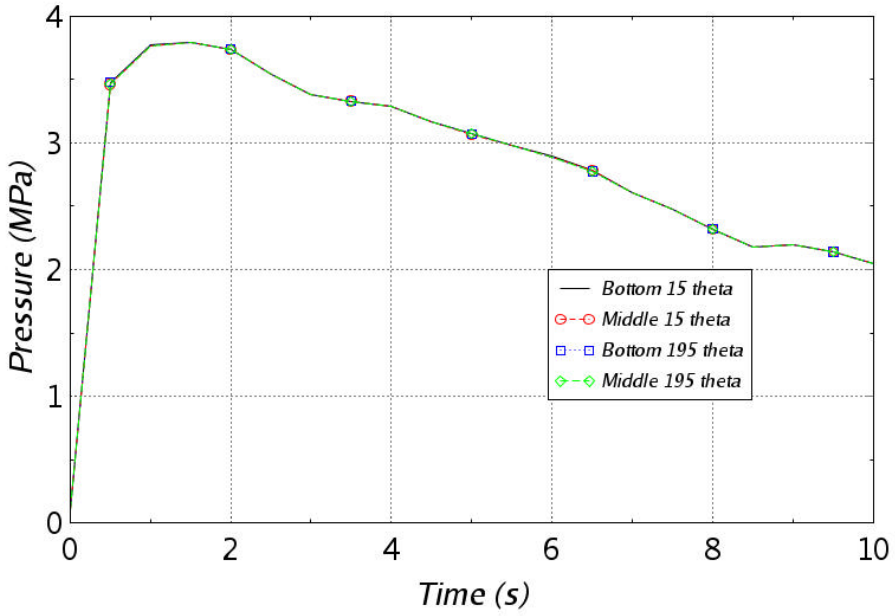

Figure 40. Pressure in the annular cavity zone, first ten seconds - 1A reference case.

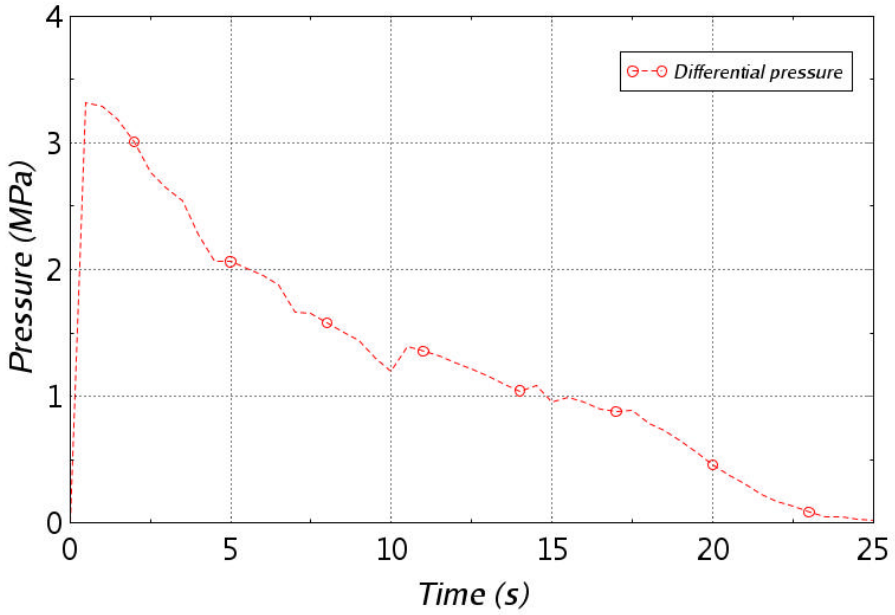

Figure 41. Differential pressure in the RPV nozzle zone - 1A reference case.

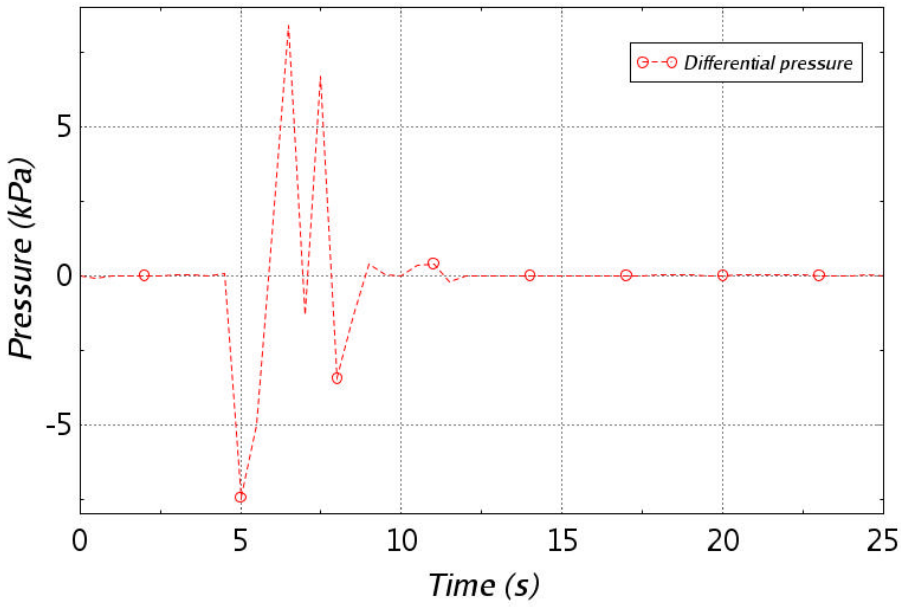

Figure 42. Differential pressure in the annular zone of reactor cavity - 1A reference case.

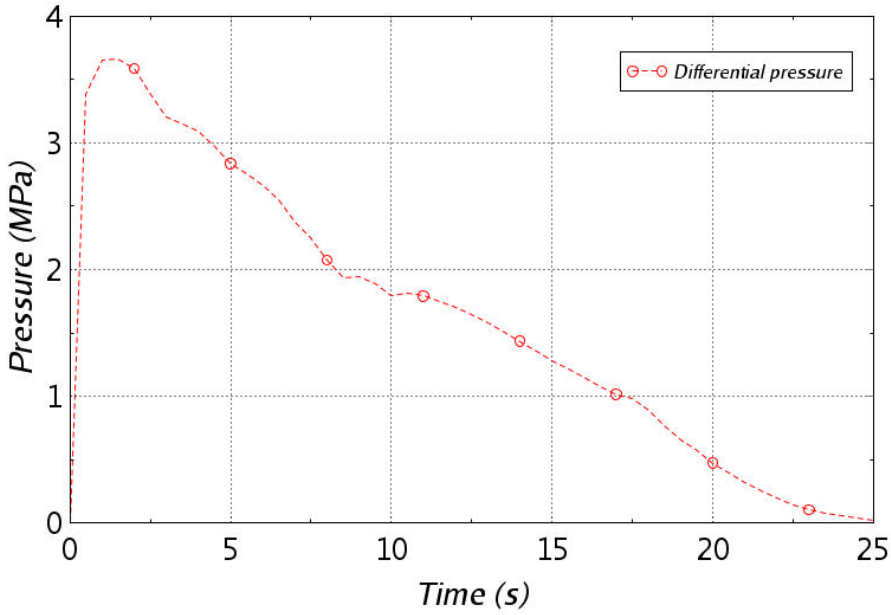

Figure 43. Differential pressure across the CBS wall - 1A reference case.

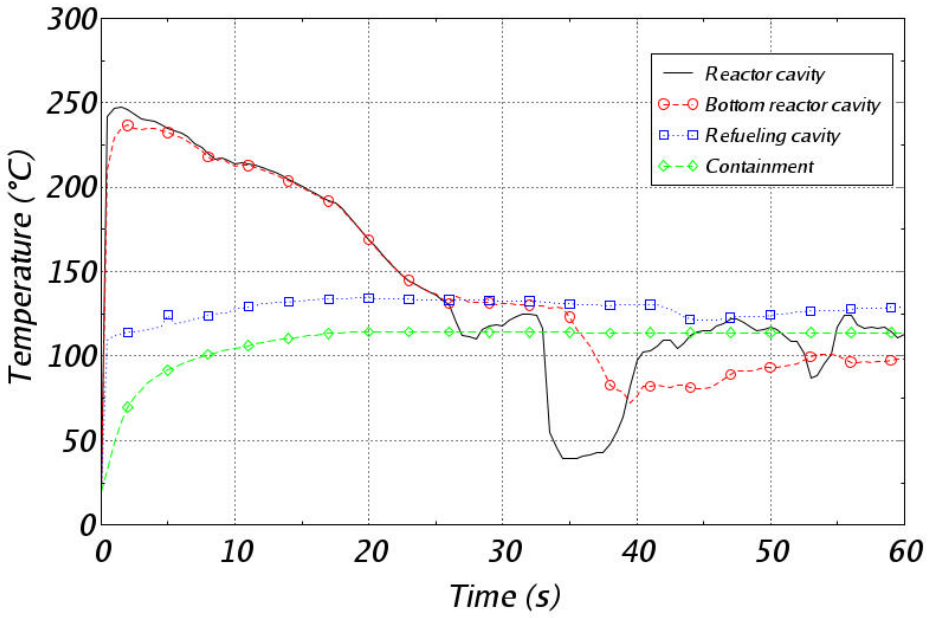

Figure 44. Reactor cavity zones and containment temperature trends - 1A reference case.

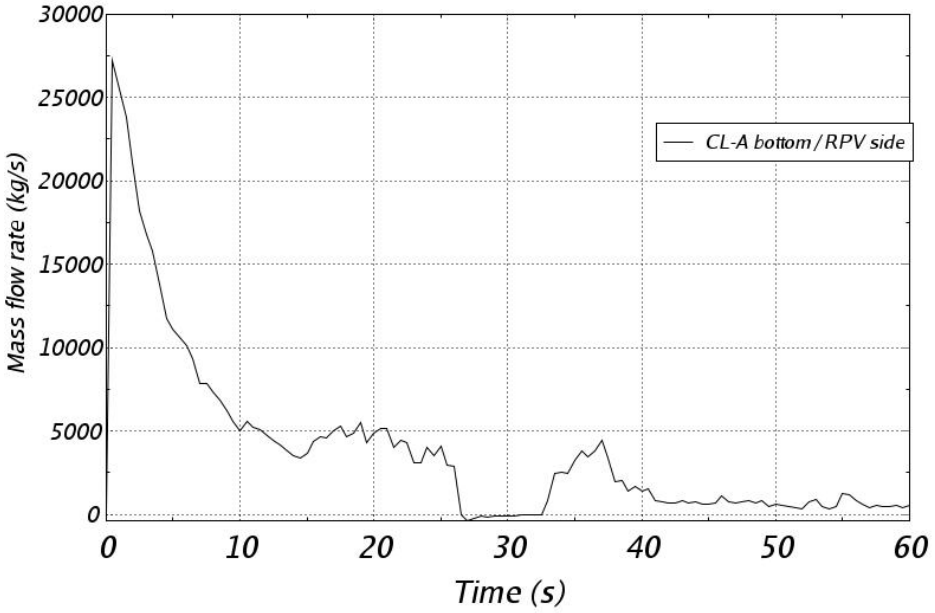

Figure 45. Mass flow at the break - 1A reference case.

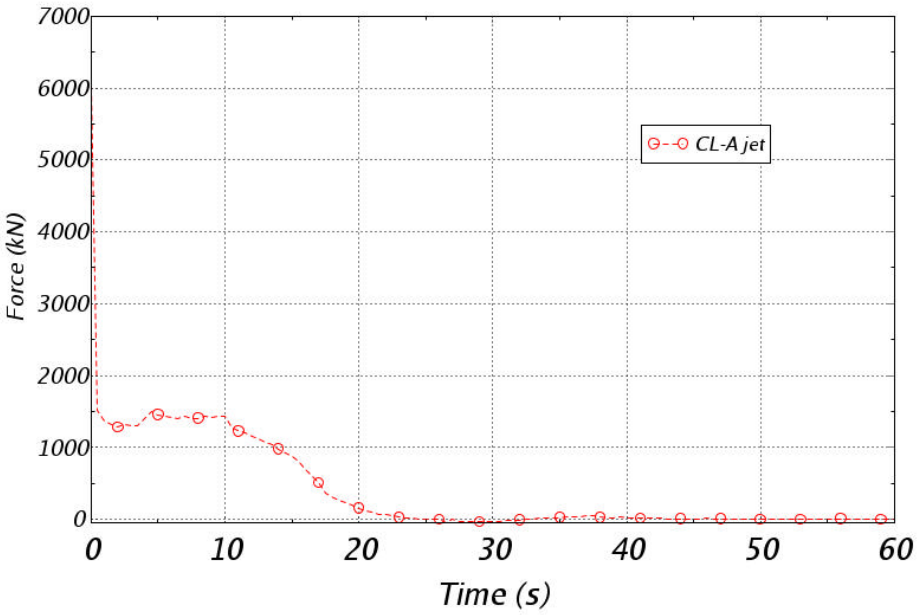

Figure 46. Jet impingement force - 1A reference case.

below and in the following figures. The HF model resulted in a slight change of the pressure peak value (see Figure 47 and Figure 48). However, the 1A break on hot-leg B (HL-B) resulted in a lower pressure load on the reactor cavity.

Table 4. Sensitivities on 1A LOCA case

Case	Cavity peak pressure	
	(MPa)	(psi)
Reference	5.21E+06	756
Henry-Fauske model	5.37E+06	779
Hot-leg B	3.92E+06	569

3.6 SENSITIVITIES ON BREAK AREA

To assess the break area effect on the cavity pressure peak, the differential pressure across the bioshield wall and the jet impingement force, calculations were run using the reference case (CL-A 1A break, Ransom-Trapp critical flow model) by changing the break area. The list of cases and the main results are reported in the tables below (Table 5 and Table 6) and in the following figures.

To perform an independent validation of the results, the calculations reported above were compared with results published by Cloud 1978. Comparison of results in Figure 52 shows that RELAP5-3D calculations are consistent with results obtained with the MULTIFLEX code. The acceptable differences between the two set of results are likely caused by differences in the reactor cavity geometry and containment that have been studied, as well as differences in the code methods.

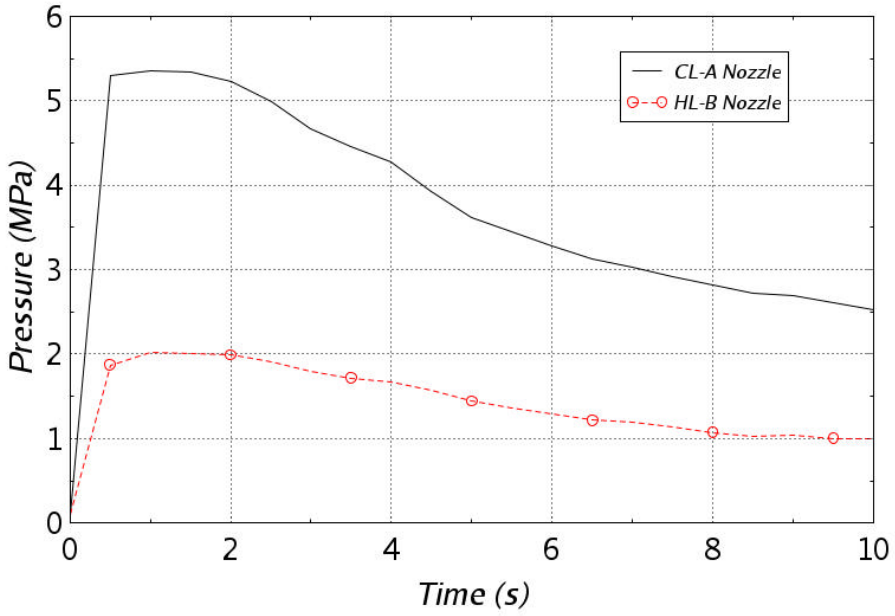

Figure 47. Pressure in the RPV nozzle zone, first ten seconds - 1A sensitivity, HF model.

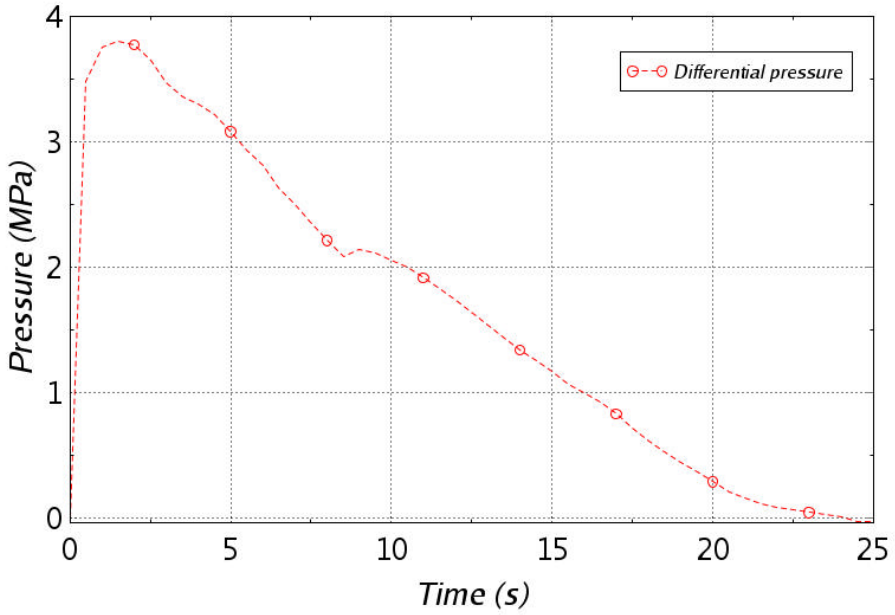

Figure 48. Differential pressure across the CBS wall - 1A sensitivity, HF model.

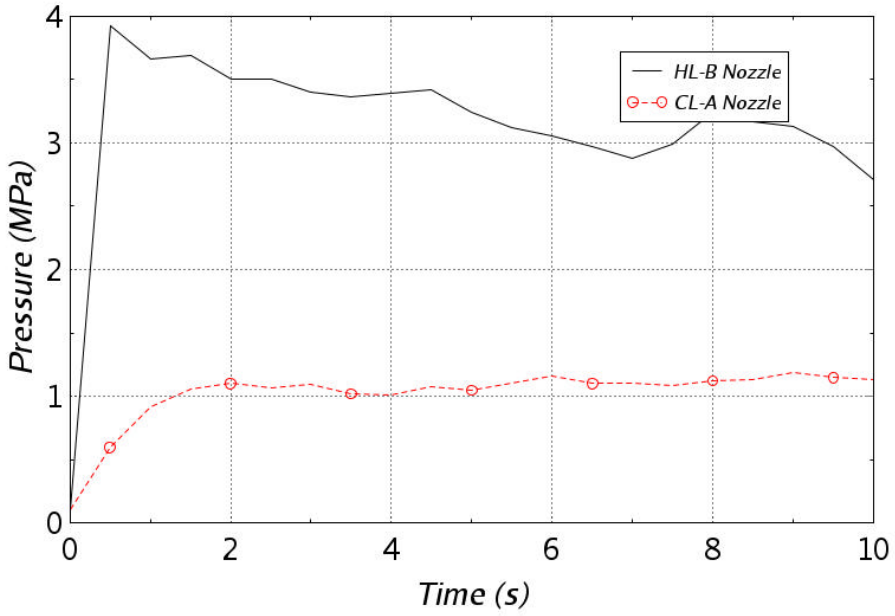

Figure 49. Pressure in the RPV nozzle zone - 1A sensitivity, HL-B break.

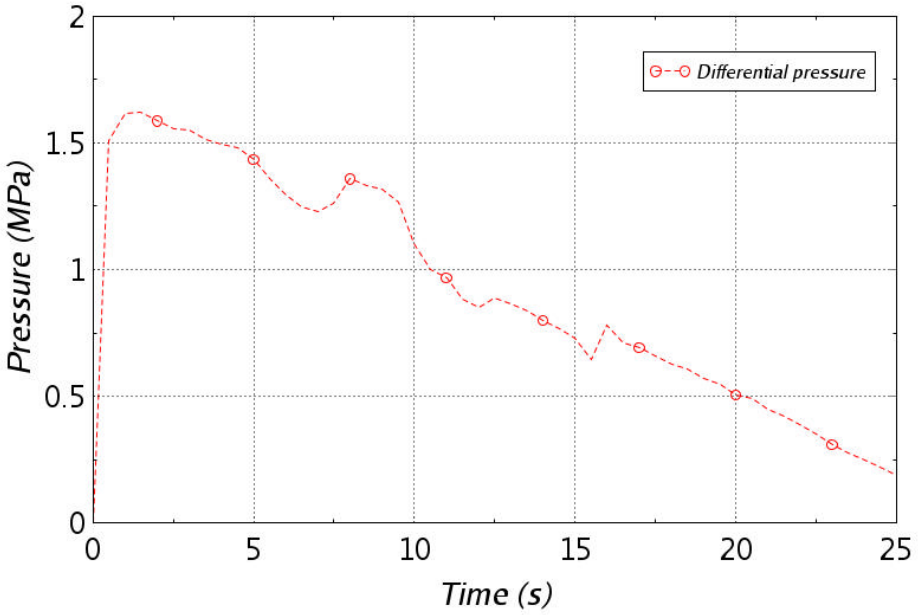

Figure 50. Differential pressure across the CBS wall - 1A sensitivity, HL-B break.

Table 5. Sensitivities on the break area

Case	Cavity peak pressure	
	(MPa)	(psi)
DEGB 2A (0.766 m2)	5.63E+06	817
Reference 1A (0.383 m2)	5.21E+06	756
0.5 A (0.192 m2)	3.91E+06	567
0.25 A (0.0958 m2)	2.38E+06	345

Table 6. Maximum jet impingement force

Case	**Maximum jet impingement force** (MN)
DEGB 2A (0.766 m2)	6.03
Reference 1A (0.383 m2)	6.03
0.5 A (0.192 m2)	3.01
0.25 A (0.0958 m2)	1.51

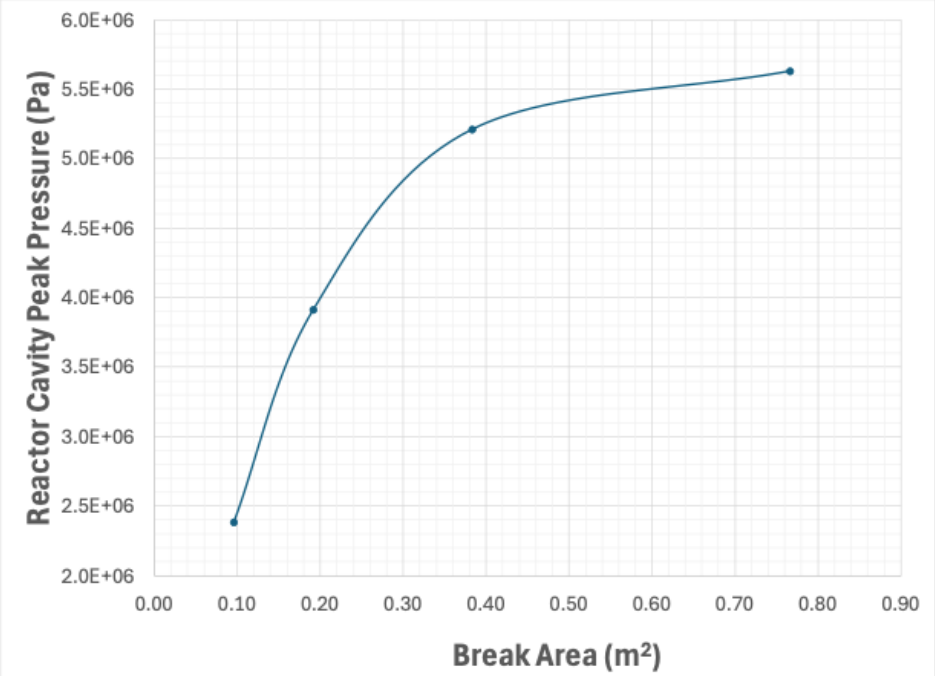

Figure 51. Reactor cavity peak pressure vs. break area.

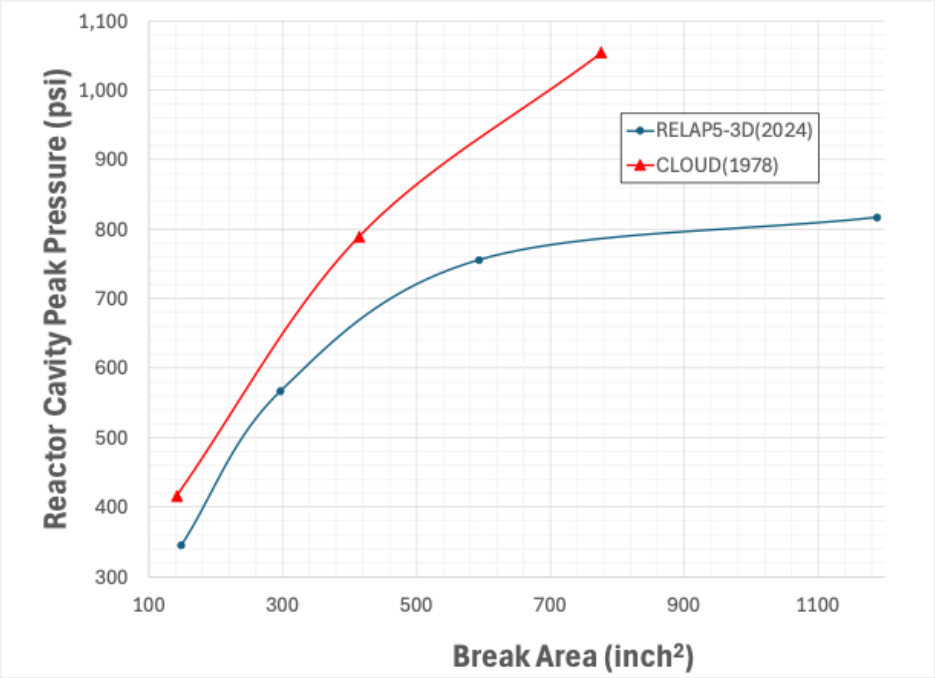

Figure 52. Comparison between RELAP5-3D results and MULTIFLEX code (Cloud 1978).

4. ASSESSMENT OF THE CBS STRUCTURAL PERFORMANCE

4.1 PRINCIPLES

The assessment of the CBS subjected to in-service irradiation includes three successive steps:

1. *Irradiation fields*. Estimates of the neutron and gamma ray radiation levels are the main operating factors affecting the properties of concrete. The radiation fields in the CBS vary with height, azimuth, and depth because of the dissymmetry of the fuel core design and the attenuation caused by concrete and embedded steel elements. Determination of the radiation fields relies on the following:

    - Extrapolation from irradiation exposure in the RPV using analytical attenuation in the concrete (Esselman and Bruck 2013). This approach is generally limited to the radial projection at the fuel core mid-elevation.

    - Simulation of the irradiation transport using established codes such as Monte Carlo N-Particle (MCNP), SCALE, and Virtual Environment for Reactor Applications (VERA)-shift (Remec et al. 2016; Risner, Alpan, and Yang 2020), to name a few. Concrete is mostly made of calcium, silicon, oxygen, and hydrogen. Hydrogen is present in the concrete mix from the batching water, which partly combines with the cement oxides to form hydrates (chemically bounded water). However, a remaining fraction of the original water remains in the form of adsorbed or free water in the capillary pores. This water can be subject to transport in liquid or gaseous forms because of unbalanced hygral equilibrium (i.e., drying). This phenomenon occurs in unlined CBS because of the reactor cavity's temperature, relative humidity, and convection caused by venting. When the CBS design includes a metal liner, the moisture remains trapped in the wall. In addition, irradiation leads to water radiolysis, eventually forming di-hydrogen and di-oxygen (Bouniol and Aspart 1998; Bouniol 2004). The radiochemistry of water in cementitious systems and the transport of radiolytic gas though convection and diffusion are complex and not well characterized to date. Because of the high cross section of hydrogen, this element is a significant contributor to the attenuation of fast neutron transport in concrete. Ideally, irradiation and moisture/gas transport should be coupled. This is currently not the practice. More commonly, uncertainties of moisture content are mitigated by studying the effects of varied hydrogen content on neutron transport. Lower hydrogen contents ("dry" concrete) evidently lead to deeper penetration of neutron in concrete.

2. *Irradiation-induced damage*. Neutron irradiation causes expansion of the concrete aggregate. The amplitude of this RIVE depends on the mineralogy of the aggregates and the received neutron fluence. At any given moment during operation, the CBS wall is subject to a field of internal expansion. In addition, the mechanical properties of irradiated concrete are affected by RIVE because of the formation of microcracking. Structural models of irradiated CBS can be organized in three categories:

    - Semi-analytical models (Andreev and Kapliy 2014; Le Pape 2015) are generally limited to 1D analysis, deriving the mechanical stress and strength profiles along the radial direction using finite difference methods. The analysis is generally conducted at the location of the highest surface fluence—at the fuel core's mid-elevation and the azimuth of the highest fluence value. These methods benefit from fast computation time, which makes it possible to run parametric and probabilistic analysis. The limitations of these methods are their inability to account for structural damage caused by excessive stress and the inaccuracies associated with approximative boundary conditions. In the following discussion, this method is referred to as "1D-semi-analytical model (SAM)."

- Mesoscale discrete models (Kambayashi et al. 2020; Le Pape, Alnaggar, and Cheniour 2023)such as rigid-body spring model (RSBM) or lattice discrete particles model (LDPM) present the advantage of an explicit representation of the mesostructure of concrete formed by coarse aggregates ($\gtrapprox$ 4 mm, the "particles") embedded in a matrix of hardened cement paste and sand. Hence, the effects of irradiation such as RIVE and the irradiated Young's modulus are explicitly represented at the level of the aggregates. The loss of concrete strength results from the formation of microcracking between "particles." Because of the difference between the millimetric size of the smallest particles and the metric dimensions of the CBS, a complete model of the CBS using discrete models is out of reach of computational resources that utilize multithread processors or even medium-sized clusters. Hence, published simulations of irradiated CBS using mesoscale models are limited to representative angular sectors.
- Finite element models (Pomaro et al. 2011; Bruck et al. 2019; Khmurovska et al. 2019; Cheniour et al. 2023) provide a main advantage through finite element analysis (FEA), generating a full representation of the CBS geometry, including the presence of reinforcement. Finite element models remain computationally intense for full 3D simulations.

3. *Residual bearing capacity*.

As explained in (Le Pape, Alnaggar, and Cheniour 2023), the varied aging structural model of the CBS was subjected to in-service irradiation using different modeling strategies (semi-analytical, finite element, discrete approach), all leading to similar conclusions:

1. Irradiation-induced damage in concrete is caused by two concurrent mechanisms: (1) *intrinsic* damage caused by formation of voids and cracking in the concrete constituents, as observed on a concrete specimen subject to free expansion, and (2) the *structural* damage caused by excessive stresses in the region subject to high fast-neutron fluence toward the reactor cavity. These excessive stresses occur in the vertical and orthoradial directions and are caused by structural constraints associated with the cylindrical geometry of the CBS and the attenuation profile of fast neutrons moving radially toward the back of the CBS.
2. Although the damaged depth varies from one model to another because of differences in the parameters used in the RIVE, damage, and creep constitutive laws, all models indicate that the damage extends to or beyond the location of reinforcement. This observation leads to questions about the integrity of the steel–concrete bond during accident conditions.
3. Cracks open mainly along the unrestrained radial direction in the region located near the reactor cavity. Crack opening width decreases with the CBS radius: larger cracks occur near the CBS surface, and minimal cracking occurs at or beyond the reinforcement location.

4.2 IN-SERVICE DAMAGE DEPTH

Estimation of the damage depth at the fuel's mid-core elevation is central to the assessment of the in-service structural performance of the CBS. As discussed in the previous section, three methods can be employed to this aim: FEA (Cheniour et al. 2023), a mesoscale discrete method such as LDPM (Le Pape, Alnaggar, and Cheniour 2023), and a 1D semi-analytical model (Le Pape 2015). The computational resources and time required to complete a single simulation using each of these methods are largely different. When either FEA or LDPM is used, several days are needed to complete a simulation on a multi-node cluster and a multi-threaded workstation, respectively. A single 1D semi-analytical simulation is completed within a few minutes on a personal computer. Hence, the 1D semi-analytical approach makes it possible to conduct large parametric—for example based on the effects of the concrete's chemical composition—and probabilistic studies. However, to date, the 1D semi-analytical approach has not yet been not validated

against the results obtained more recently using finite element method (FEM) and LDPM. This topic is addressed in the next section.

4.2.1 Comparison between FEM, LDPM, and 1D Semi-Analytical Methods

The nature, constitutive models, and boundary conditions of the three models exhibit differences:

- FEM and 1D-SAM consider concrete as a homogeneous material and assume a continuum description of concrete structures. Instead,LDPM explicitly represents the coarse aggregate distribution and model discontinuity caused by cracking.
- The 1D-SAM accounts only for the *intrinsic* irradiation-induced damage, meaning the loss of mechanical properties caused by microcracking. The FEM includes both *intrinsic* irradiation-induced damage and *structural* damage following the isotropic damage model proposed by Mazars and Pijaudier-Cabot (1989). The LDPM addresses *intrinsic* irradiation-induced damage by reducing the Young's modulus of the irradiated aggregate and accounting for microcracking in the mortar, which arises from microstructural heterogeneity and differential expansion between adjacent aggregates. Additionally, *structural* damage is represented at the level of the mortar.
- The boundary conditions (BCs) in the vertical direction assumes no deformation or homogeneous deformation for the 1D-SAM and LDPM, respectively. The BCs of a representative wedge cut-out from the CBS at the fuel'smid-core elevation are mixed deformation and stress conditions resulting from the structural response of the entire CBS subject to a nonuniform field of fluence.
- A similar comment can be made about the BCs in the orthoradial direction which are assumed axisymmetric for the 1D-SAM and LDPM.

Nevertheless, the noted variations in BCs only moderately affect the mechanism underlying the formation of damage, which is governed by RIVE-induced unconfined expansion in the radial direction near the reactor cavity.

In the following itemized analysis, the different models were run with comparable conditions:

- The fast neutron flux profile is obtained from irradiation transport using the VERA-Shift code (Cheniour et al. 2023).
- The temperature ranges from 65 °C at the inner radius and 40 °C at the outer radius.
- Aggregate RIVE is calculated assuming a quartz content of 92% and a RIVE model derived from Bykov et al. (1981) (see equations in (Le Pape, Alsaid, and Giorla 2018)). Concrete RIVE is obtained using comparable homogenization rules in the LDPM and 1D-SAM.
- The loss of the Young's modulus of irradiated aggregate and concrete assumes empirical relations derived from post-irradiation measurement of the Con-A concrete and GA(F) aggregate specimens provided by the JCAMP (Maruyama et al. 2017; Sabatino et al. 2024).
- The unirradiated tensile and compressive strengths of concrete are similar in all simulations.
- No concrete shrinkage is considered.

Figure 53 presents the results of previous simulations obtained using LDPM and FEM. Within the damaged depth, the damage profiles are much sharper (solid lines) than the profiles obtained from the finite element simulation using Grizzly (dashed lines). Whereas the maximum damage value at the surface of the CBS gradually increases with the operation time, its value is always higher in the interpretation of the LDPM simulations.

In the LDPM simulation, the RIVE value near the surface of the concrete creates a delamination of cement paste located between the liner and the first layer of aggregates, as well as spalling of the aggregates located in the immediate nearby region. In the finite element model, the heterogeneities created by aggregates of varied sizes are not represented. Thus, the induced microcracking is not represented either.

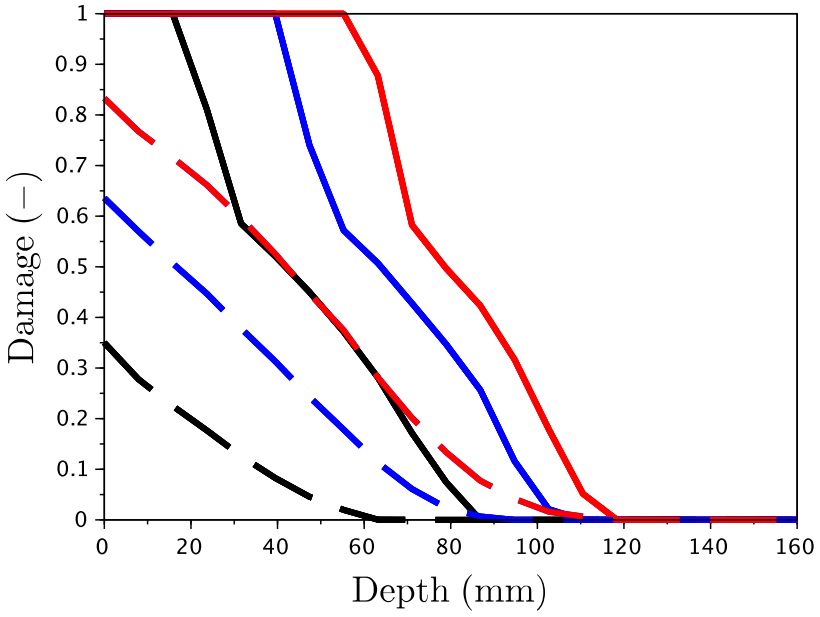

Figure 53. Comparison of the damage profile in the CBS obtained using LDPM (solid lines) and FEM (dashed lines) at 40, 60, and 80 years of operation (in black, blue and red, respectively).

The damage depth corresponds to the maximum depth at which damage is strictly positive. These damage depths are plotted against the fast neutron fluence at the surface of the concrete in Figure 54. Note that the results presented here are representative only for ordinary concrete, in which the aggregate is almost exclusively composed of quartz ([Qz] = 92%). The blue diamond and red square markers correspond to the damage depths obtained by LDPM and FEM, respectively. The dashed and solid lines correspond to the damage depths obtained using 1D-SAM simulation. The dashed line represents the damage criterion related to excessive biaxial compression, whereas the solid line corresponds to the damage criterion associated with excessive radial deformations. Notably, the deformation-based criterion shows a strong correlation with the FEM-based results. In contrast, the stress-based criterion fails to capture damage resulting from the formation of cracks caused by RIVE unconfined in the radial direction and confined in the vertical and orthoradial directions as indicated by the red regions in Figure 55. However, this criterion should not be dismissed entirely because it may be more conservative in situations where the quartz content—and hence the RIVE amplitude—is significant.

In conclusion, estimates of the damage depth caused by in-service irradiation of the CBS at the elevation of the fuel's mid-core can be obtained using the 1D-SAM. This approach is computationally unintensive and thus makes it possible to run varied scenarios, including study of extended duration of operation and the role of varied mineral composition of the concrete aggregate.

The effects of mineralogy on damage depth are not the specific subject of this report. However, some results obtained from previous research on igneous or magmatic rocks are presented here to provide ranges

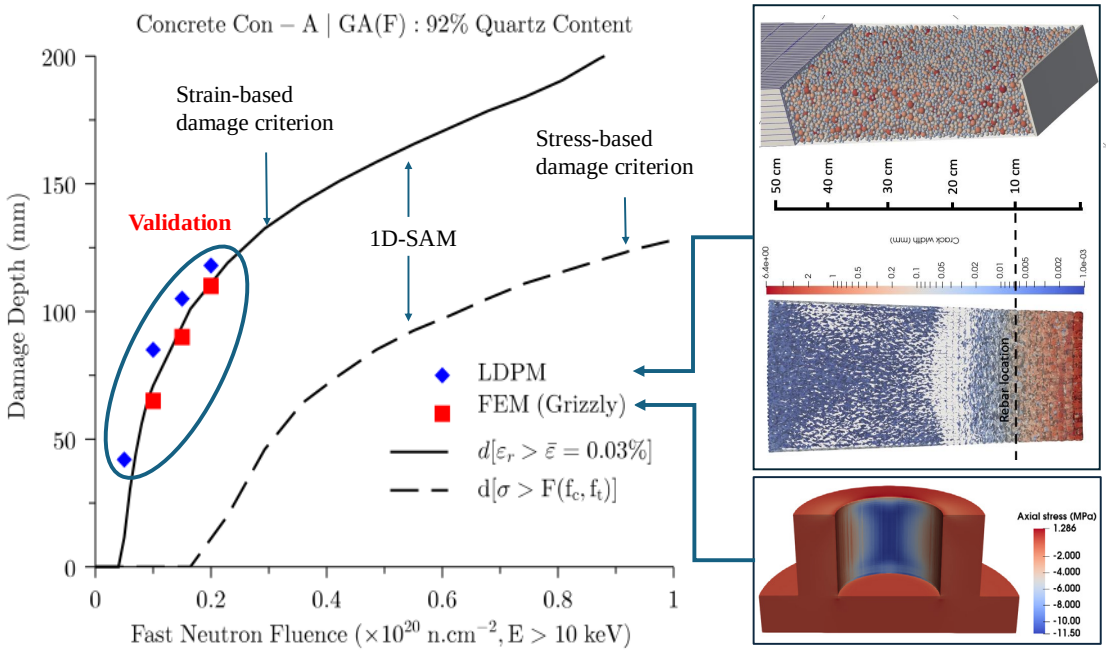

Figure 54. Damage depth in the CBS with increasing fast neutron fluence at the surface of the concrete. Comparison of LDPM, FEM, and 1D-acsam simulations.

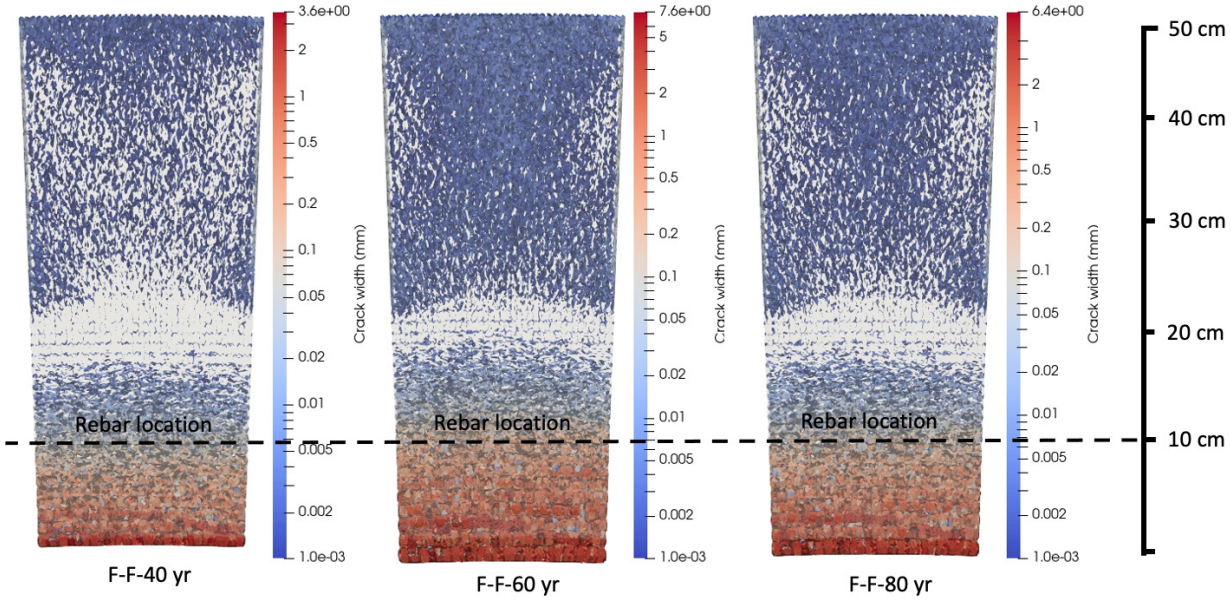

Figure 55. Crack opening map (top view) using the LDPM (Sabatino et al. 2024).

of damage depths at varying operation durations.

In a previous report (Le Pape, Sabatino, and Tajuelo Rodriguez 2023), the estimated damage depth was obtained using a stress-based criterion. Here, the results are presented using a strain-based criterion.

The formation of igneous rocks depends on the thermodynamic equilibrium of mineral phases associated with the cooling of magma. From a single parental magma, all the various types of igneous rocks can be derived following the so-called Bowen series (Bowen 1913).

The common minerals of igneous rocks can be classified into two series: a continuous reaction series of feldspars, and a discontinuous reaction series of ferromagnesian minerals (olivine, pyroxene, hornblende, biotite). The second reaction series is characterized by a gradual coordination of silicate tetrahedra, progressing from isolated silicates to chain silicates to sheet silicates, and finally to framework silicates.

The RIVE susceptibility of silicates is correlated with the Goldich series (Le Pape, Alsaid, and Giorla 2018)—Figure 56— which describes the tolerance of silicates to weathering (Goldich 1938). The Goldich series is essentially the reverse of the Bowen series.

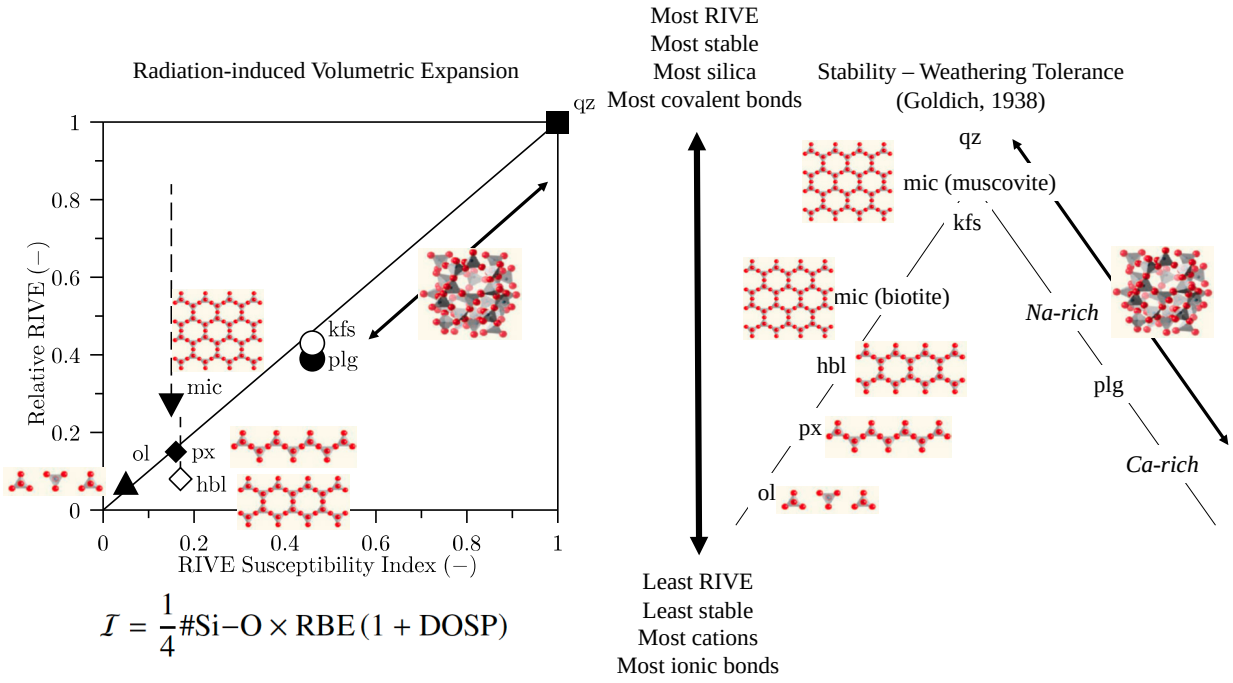

Figure 56. Reproduced from (Le Pape, Alsaid, and Giorla 2018). Correlation of the RIVE susceptibility index, $\mathcal{I}$, and the relative maximum volumetric expansion normalized by that of quartz (17.8%) for different groups of minerals—hornblende (hbl), potassium feldspar (kfs), micas (mic), olivine (ol), (data limited to high-magnesian olivine), plagioclase (plg), pyroxene (px), and quartz (qz) (Whitney and Evans 2010). Vertical dashed lines indicate the uncertainty of the maximum RIVE expansions (left), and Goldich series showing the tolerance of silicates against weathering (right).

Using the Bowen series, the compositions of various igneous rocks can be determined (Figure 57). The names of the rocks are given according to their silicate proportions.

Note that in this study, the distinction between intrusive (plutonic) and extrusive (volcanic) igneous rocks is ignored. Although comparable mineral compositions can be found between intrusive and extrusive

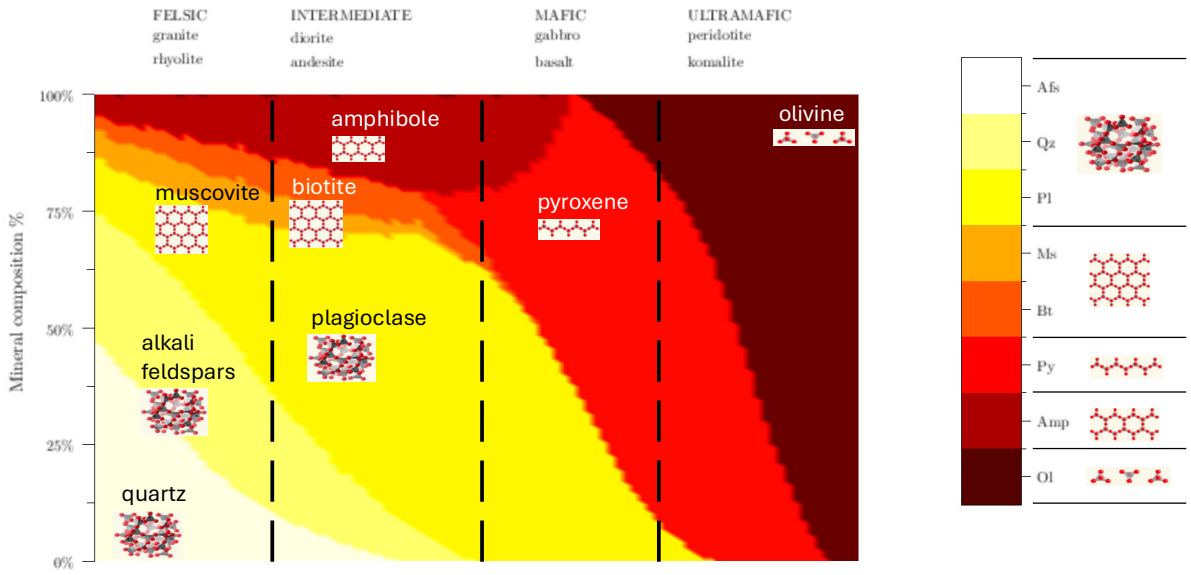

Figure 57. Mineral compositions of igneous rocks.

rocks, the faster cooling rate of extrusive rocks leads to the formation of smaller grains compared to those in intrusive rocks.

In the proposed model, the effects of grain size on the irradiated properties of the rocks are not considered. In Figure 57, the names of the rocks are given first for the intrusive form and then for the extrusive form: for example, granite (intrusive), and rhyolite (extrusive).

Using the information provided in Figure 56, it can be inferred that ultramafic igneous rocks, which contain mostly isolated and chain silicates, are likely to be less susceptible to RIVE than felsic igneous rocks, which contain framework and sheet silicates. This expected result is confirmed by the simulation.

Figure 58 shows the calculated RIVE values for various igneous rocks following the compositions presented in Figure 57. The vertical axis corresponds to increasing fast neutron fluence. All simulations presented in Figure 58 were run at 45 °C.

Interestingly, the RIVE of intermediate and mafic igneous rocks (the middle portion of the color map) is lower than the RIVE of both felsic and ultramafic igneous rocks.

Finally, Figure 59 presents the calculated irradiation-induced damage depths in the CBS for the various igneous rock compositions. The simulations were conducted using the 1D-SAM model presented in the appendix.

The observations from Figure 59 and Figure 58 show a qualitative correlation between the RIVE and the irradiation-induced damage depth. The most susceptible type of igneous rocks is granite (or rhyolite).

The corresponding irradiation-induced damage depths are approximately 10 cm, 15 cm, and 19 cm at fast neutron fluences of 2×10^{19}, 4×10^{19}, and 8×10^{19} n.cm^{-2} ($E > 10$ keV), respectively.

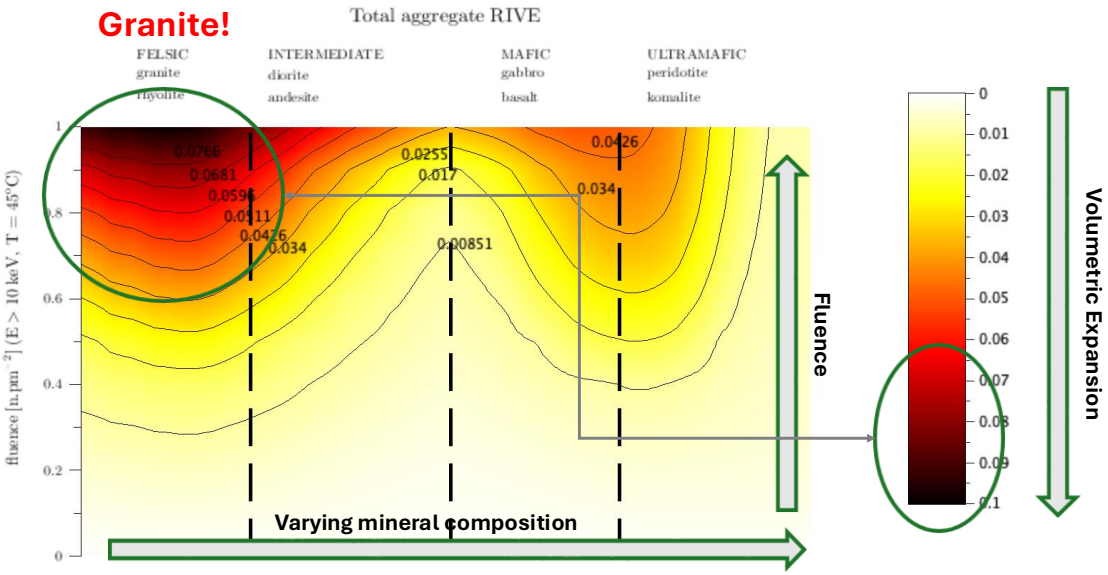

Figure 58. Calculated RIVE of varied igneous rocks with increasing fast neutron fluence at a temperature of 45 °C.

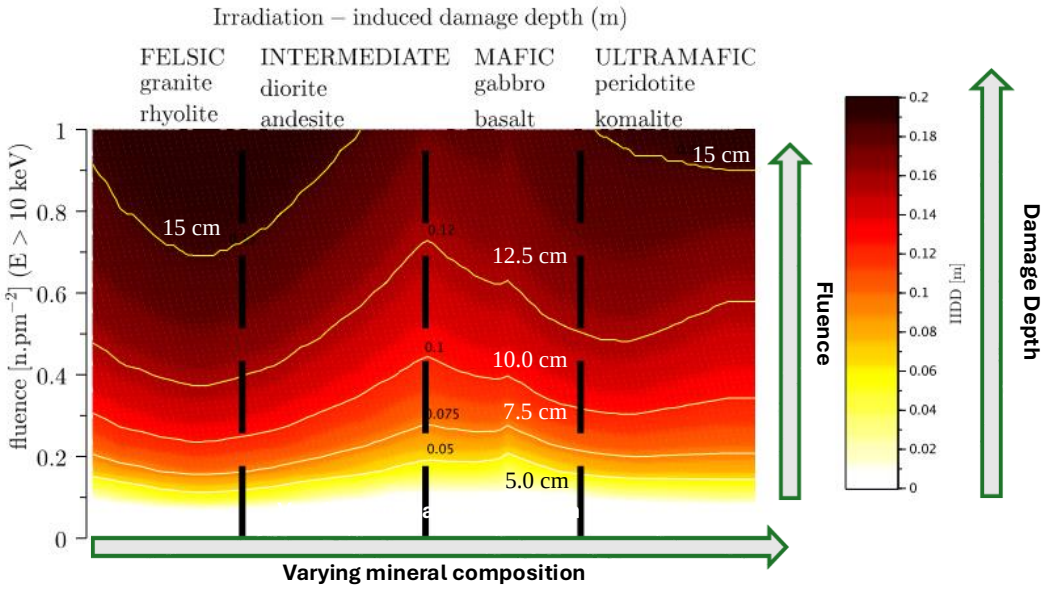

Figure 59. Calculated irradiation-induced damage depth of varied igneous rocks with increasing fast neutron fluence.

4.3 LOCA EFFECTS ON CBS DAMAGE

In this section, the thermomechanical effects of LOCA on CBS damage are studied. LOCA causes vapor release in the reactor cavity with increased pressure and temperature.

4.3.1 Cavity Pressure

Because CBS geometry can be modeled as a thick cylindrical structure, the pressure-induced stress field in the undamaged concrete can be approximated from:

$$\sigma_\theta = p\frac{r_a^2}{r_b^2 - r_a^2}\left(1 + \frac{r_b^2}{r^2}\right) \tag{2}$$

and

$$\sigma_r = p\frac{r_a^2}{r_b^2 - r_a^2}\left(1 - \frac{r_b^2}{r^2}\right), \tag{3}$$

where r_a and r_b are the inner and outer radii of the CBS, and p is the LOCA-induced pressure relative to the atmospheric pressure. This pressure exerts compression in the radial direction and tension in the orthoradial direction. The maximum value of $|\sigma_r|$ is p at the inner surface of the CBS. The maximum value of σ_θ is equal to $p(r_b^2 + r_a^2)/(r_b^2 - r_a^2)$. For example, assuming values of 2.4 m for the inner radius and a CBS wall thickness of either 1 m or 2 m, $\sigma_\theta(r_a)$ equals $\sim 3.00p$ or $\sim 1.85p$, respectively. Thus, depending on the value of p, the orthoradial stresses may exceed the tensile strength of the concrete. As a result, the structural integrity of the CBS may partly depend on the presence of hoop reinforcement and the ability to transfer loading from the concrete to the bonded reinforcing bars.

Equations (3) and (2) are valid under the assumption that the elastic properties of the concrete are uniform within the CBS, and therefore they apply before the onset of irradiation-induced damage during service. However, it is important to note that the cavity pressure produces tensile orthoradial stresses, whereas irradiation-induced orthoradial stresses are compressive. As a result, during LOCA, the pre-existing orthoradial stresses may be relaxed.

4.3.2 Accidental Temperature

The release of vapor increases the temperature in the reactor cavity. During the LOCA, the temperature profile in the CBS evolves over time as a function of the reactor cavity temperature history and heat conduction through the wall. This type of transient has been studied using the LDPM (Alnaggar, Choi, and Le Pape 2023). For the sake of illustration, the model is reproduced in . Further details can be found in the referenced technical report (Alnaggar, Choi, and Le Pape 2023).

4.3.3 Models

The modeling strategy adopted to estimate the additional damage depth caused by a LOCA is similar to that used to determine the in-service irradiation-induced damage depth at the elevation of the fuel mid-core elevation. The LDPM simulation results presented in (Alnaggar, Choi, and Le Pape 2023) serve as baseline data. The Alnaggar, Choi, and Le Pape study was performed to obtain an understanding of the effects of thermal exposure during LOCA on the depth of cracking and degree of damage of the CBS at different ages, thus accounting for RIVE effects. Three LOCA scenarios were considered, starting with no RIVE (pristine control case, assuming no irradiation-induced degradation) and RIVE-induced degradation after 20 and 40 years of operation. The simulations were performed in three steps:

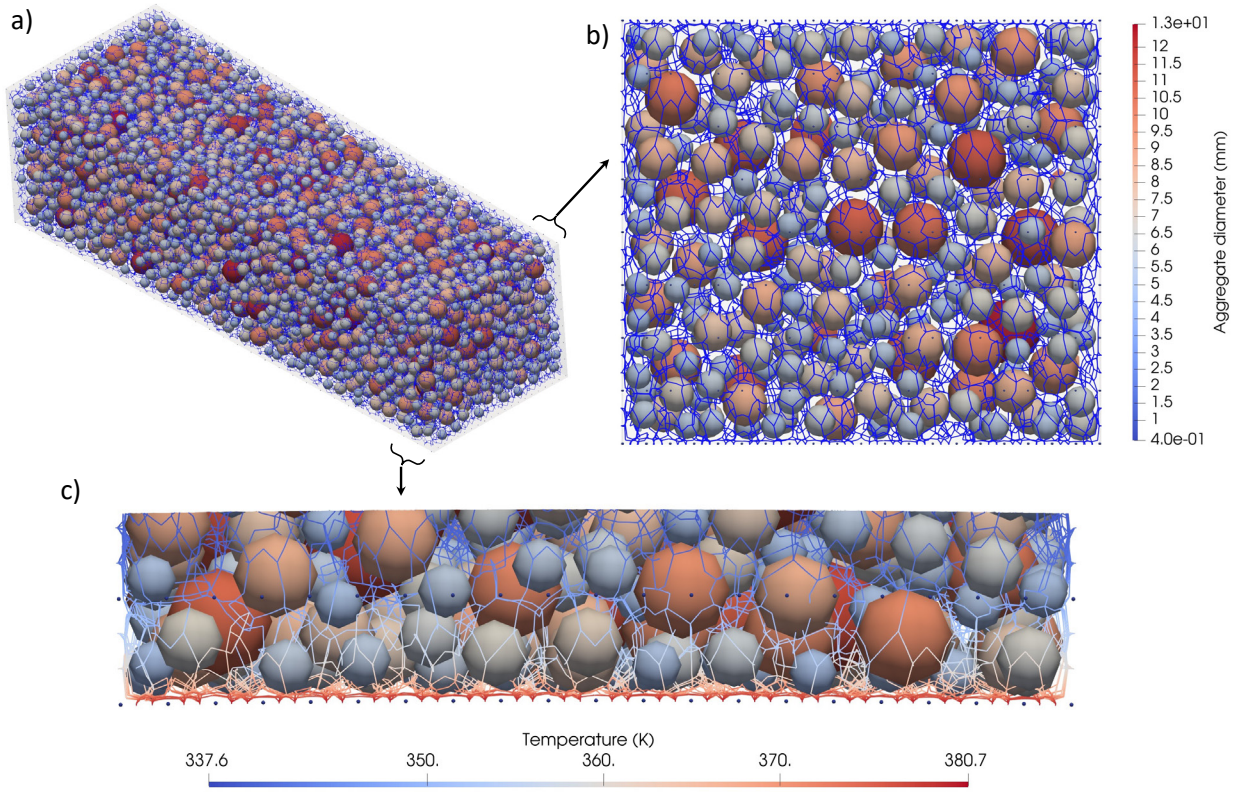

Figure 60. Heat diffusion conduit network surrounding LDPM concrete particles: (a) the full 300 mm sector system with conduits colored in blue, and aggregates colored based on their diameters, (b) front view of a slice of the first 20 mm from the inner surface, (c) top view of the same slice with the diffusion network colored according to temperature gradient during the early LBLOCA thermal shock peak.

1. The in-service irradiation depth was calculated assuming that the neutron attenuation profile did not vary over time, thus ignoring the possible effects of core or internal design changes. The single input parameter was the fast neutron fluence at the surface of the concrete. RIVEs were determined from the fluence and in-service temperature profiles. The induced cracking and damage in the CBS sector were obtained from the mechanical simulations using LDPM.
2. A thermal shock caused by LOCA was applied to the surface of the concrete. The transient temperature profiles were calculated using the LDPM's heat transfer simulation. (See the temperature profile in Figure 61).
3. The mechanical response of the irradiation-induced pre-damaged CBS sector to the thermal expansions caused by LOCA was calculated to determine the increase in damage depth.

Hence, these computationally intensive simulations provided three damage depths that were used as benchmark data points to be compared with a 1D-SAM.

1D-SAM relies on linear simulation principles, even though the concrete properties vary with exposure to neutron irradiation. Hence, loading can be superimposed into a single simulation to account for irradiation-induced RIVE, LOCA-induced temperature increase, and LOCA-induced pressure in the reactor cavity. For the sake of comparison with LDPM, pressure is ignored at this stage.

The LOCA-induced temperature profiles vary over time, starting with a spike (black line in Figure 61, temperature vs. depth plot) at the surface of the concrete when subjected to steam release in the cavity, evolving into quasi-linear profiles after a few hours (turquoise, green, and magenta lines in Figure 61, temperature vs. depth plot).

In the 1D-SAM simulation, only a linear temperature profile was considered as an approximation of the temperature profile at approximately 1 hour after the start of the LOCA. The main plot in Figure 61 shows the evolution of the damage depth caused by a combination of irradiation and LOCA loading with an increasing fast neutron fluence at the surface of the concrete. The same stress-based (dashed line) and strain-based (solid line) criteria are used to interpret the 1D-SAM results and to compare them with the LDPM results (blue diamonds) which model a LOCA occurring after 0, 20, and 40 years of operation. The agreement between LDPM and 1D-SAM provides reasonable assurance that the simplified model can be employed to conduct parametric studies.

Thus, 1D-SAM simulations could be expanded to account for varying temperature and pressure in the reactor cavity during a LOCA. The modeled temperature increase and pressure during a LOCA range from 15 °C to 40 °C and from 0 to 1 MPa, respectively[3]. In-service irradiation was considered for six different fast neutron fluences at the surface of the concrete: 0.5×10^{19}, 1×10^{19}, 2×10^{19}, 4×10^{19}, 7×10^{19}, and 10×10^{19} n.cm^{-2} ($E > 10$ keV). The results of the 216 simulations are summarized in Figure 62. Each colored heat map corresponds to a specific irradiation condition. It can be observed that all maps are qualitatively similar. Note that the range of values varies from one heat map to another; refer to the contour line values on each map for clarification. The highest LOCA-induced damage depth occurs at the highest temperature increase and lowest pressure in the cavity. The reason for this is that temperature increase and pressure in the cavity contribute to opposite mechanical effects in the concrete region near the reactor cavity. Temperature increase and irradiation-induced expansion cause the development of biaxial compression in the concrete, whereas pressure in the cavity creates tension in those directions. Within the range of modeled temperature increase and pressure, the variation in LOCA-induced damage depth is approximately 30 mm for each in-service irradiation value. The main variation in damage depth is caused

3. Simulated pressure values: 0, 0.1, 0.25, 0.5, 0.7, and 1.0 MPa. Simulated temperature increase values: 15, 20, 25, 30, 35, and 40 °C.

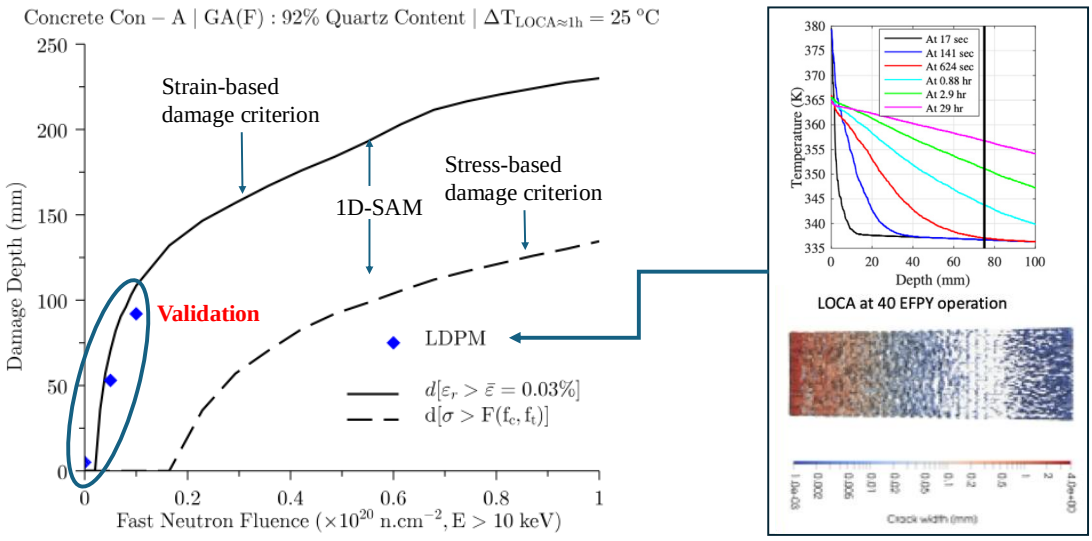

Figure 61. LOCA-induced damage depth in the CBS with increasing fast neutron fluence at the surface of the concrete. Comparison between LDPM and 1D-SAM simulations.

by in-service irradiation. Figure 63 shows the evolution of the damage depth with increasing fast neutron fluence, comparing the effect of in-service irradiation alone (black line) and the combined effects of in-service irradiation and LOCA (red line: average values). The increase in damage depth caused by LOCA is approximately 25 mm, independent of in-service irradiation, and it extends to an additional 40 mm in the worst-case scenario.

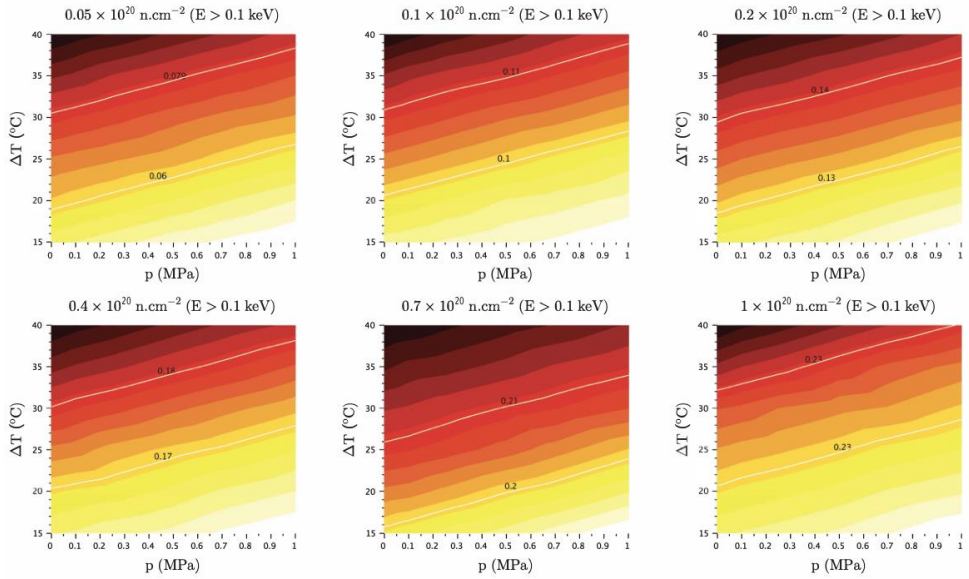

Studied range
ΔT_{1h}: +15 to +40°C
p: 0 to 1 MPa

Limited effect of the range of pressure and temperature on the damage depth increase.

Main factor: in-service irradiation

Figure 62. LOCA-induced damage depths at varied in-service fast neutron exposures, and varied pressure and temperature increase in the reactor cavity during a LOCA.

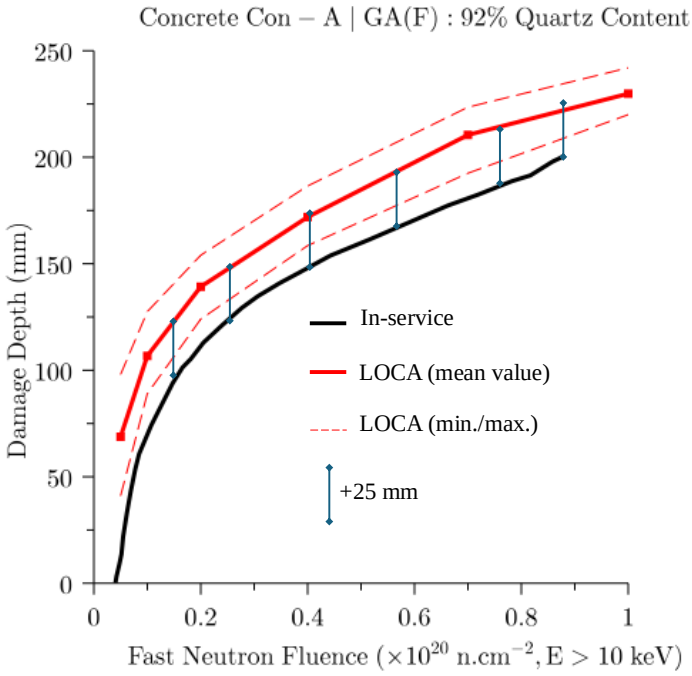

Figure 63. Combined in-service irradiation and LOCA effects of the damage depth.

5. ASSESSMENT OF THE RPV SUPPORT SYSTEM

This section provides an analysis of the bearing capacity of a generic RPV shoe-type support system with a focus on the resistance of the anchor group system embedded in concrete and subjected to in-service irradiation.

5.1 GEOMETRY

A study of a shoe-type support is presented in this report. Specific design may vary from one reactor to the other.

> *Per system design requirements, the RPV supports must restrict movement of the RPV under all design loading conditions. At the same time, the RPV must be allowed to expand and contract under varying temperature conditions. A 'shoe' interface, also referred to as a 'saddle,' is used under the inlet and/or outlet nozzles or under load brackets between nozzles; the shoe restricts vertical and tangential movement, but allows radial thermal growth of the RPV. The loadings on the shoe are transferred to the underlying support system. The shoe is anchored to the top of the biological shield wall (i.e., either sitting directly on the top surface or set in a recess on the top surface). The shoes are attached to metal weldments. These designs incorporate some type of air or water cooling to minimize heat transfer to the underlying concrete. Some designs incorporate taller vertical plates that allow for better air cooling, but place the load-bearing baseplate of the weldment on the concrete, closer to the higher radiation fields at the beltline of the RPV* (Biwer et al. 2021).

In this study, a generic shoe-support design inspired by Farley's design was analyzed. The details of Farley's support system are presented in Figure 8, p. 12. Additional details of the shoe box design are shown in Figure 64.

The description of Farley's support system is provided in (Southern Nuclear 2017):

> *The reactor pressure vessel (RPV) rests on six steel supports which are located underneath the RPV nozzles. There are six supports; one support for each of the three hot leg nozzles and one support for each of the three cold leg nozzles. Each nozzle support consists of two parts, one part (the upper part) which is attached to the nozzle and the lower part which supports the upper part and is in turn supported by the concrete primary shield wall. The lower part is anchored into the concrete primary shield wall. The upper part is allowed to slide on the lower part to allow for thermal expansion of the RPV. The load path from the RPV is the nozzle support upper part through the lower part to the concrete surface. The gross cross-sectional area of the primary shield wall is approximately 835 square feet, as compared to sum of the footprint areas of the six supports, which is approximately 76.6 square feet. Based on these areas, the supports occupy less than ten percent of the cross-sectional area of the primary wall.*

5.2 LOADING

The maximum loads induced in PWR vessel supports are those from the combined effects of postulated pipe ruptures (LOCA), SSE, and other loads per the licensing basis.

Both LOCA and earthquakes involve complex dynamic loading and structural analysis, including thermohydraulics, fluid-structure interaction, and soil-structure interaction. To derive the loading conditions

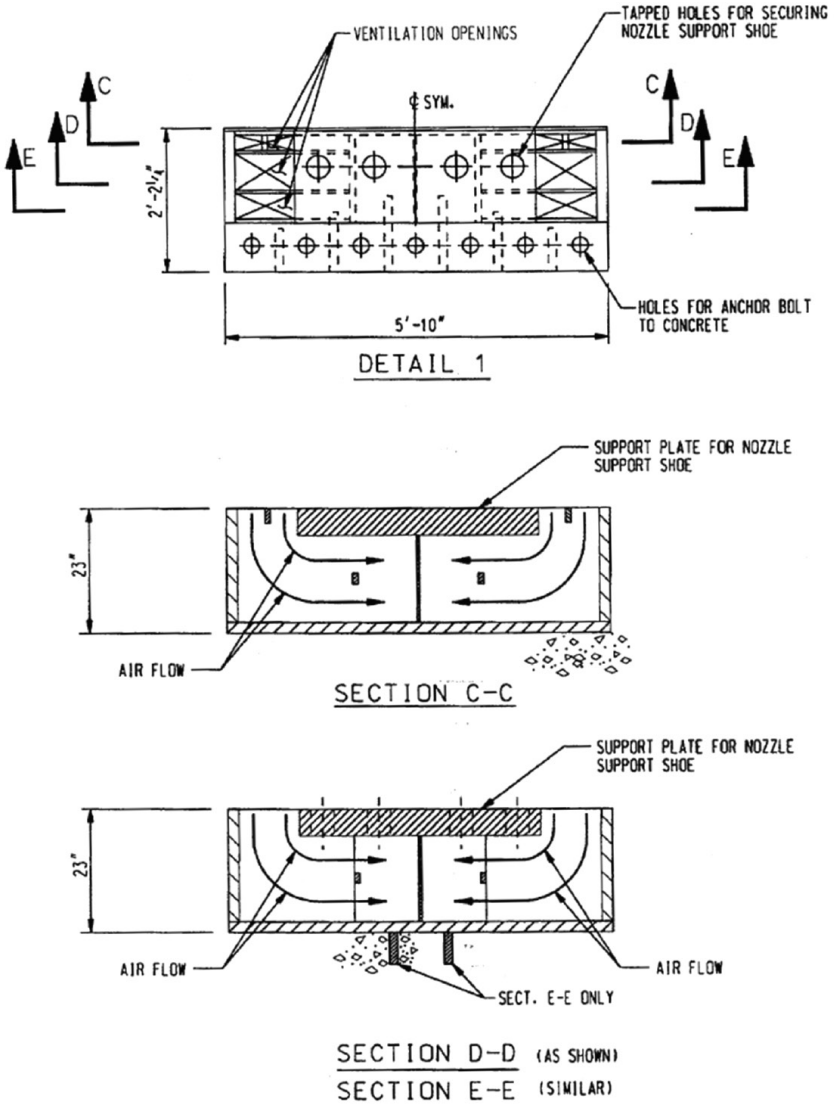

Figure 64. Farley Units 1 and 2 reactor vessel support box detail.

exerted on the RPV support structures, thermohydraulics and structural models are used, including the reactor's main components—reactor vessel, steam generators, reactor coolant pump, main coolant piping (Beukelmann et al. 2012); the main concrete structural components—CBS, concrete containment building (CCB)); and a refined description of the reactor internals and core assemblies, as well as the reactor vessel supports. In this report, the objective is to assess the bearing capacity of a shoe-type support system and the possible effects of irradiation on that system. Realistic loading scenarios are considered based on published information available in the literature and as informed by best judgment.

5.2.1 LOCA

Cloud (1978) provides time-dependent loads at the RPV support locations for a Westinghouse 4-loop PWR. Break locations are postulated in the reactor coolant loop using the methods and criteria outlined in WCAP-8082 (1973). Figure 65(a) shows the vertical and horizontal forces at the support under the broken nozzle. Note that the intervals where the vertical force is zero indicate lift-off during these periods. Because of the unilateral boundary conditions in the support system and the downward movement of the vessel's centerline (Figure 66), the vertical load at the support near the break varies from 0 (lift-off) to compression, with a maximum value of approximately 1.1×10^6 pounds (~5 MN). At the opposite support, no lift-off is observed, and the vertical compression ranges between approximately 0.8 and 13 MN as the vessel rocks on its supports (Figure 66). The horizontal load at the support located at the broken nozzle is directed toward the CBS's back wall, opposite the concrete edge near the cavity. The horizontal load shows an initial spike around 2.8×10^6 lb (~12.7 MN), followed by variations around an average value of about 6.75 MN. The horizontal load at the nozzle opposite the break is not reported in (Cloud 1978). Nevertheless, because of the vessel's rocking motion, it is assumed that the horizontal load at this location may be directed toward the edge of the concrete, toward the reactor cavity. "Generally, the peak horizontal loads and peak vertical loads do not occur at the same support. The largest vertical load occurs beneath the nozzle on the opposite side from the broken nozzle, and the peak horizontal load occurs on the supports that are mostly perpendicular to the broken nozzle" (Biwer et al. 2021).

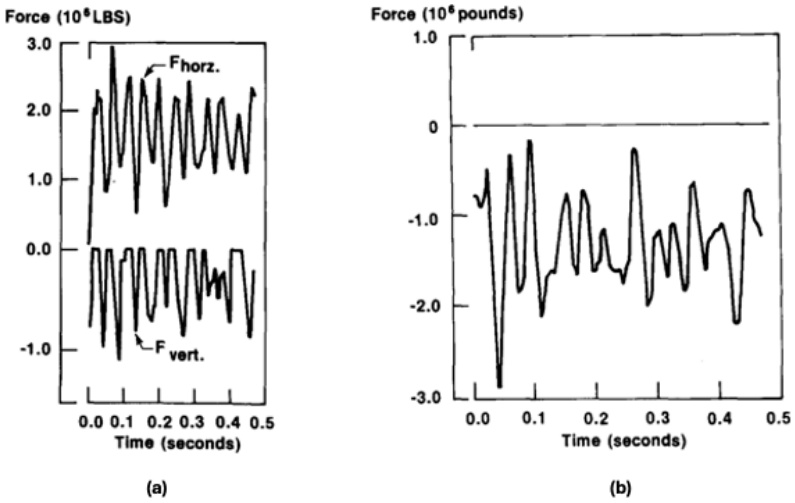

Figure 65. LOCA-induced time-dependent load at (a) the broken nozzle support and (b) the support opposite the broke nozzle (Cloud 1978).

The peak horizontal load values provided by Cloud (1978) appear to be higher than the estimated jet impingement thrust calculated using RELAP5-3D (see Table 6), although these values are comparable to the

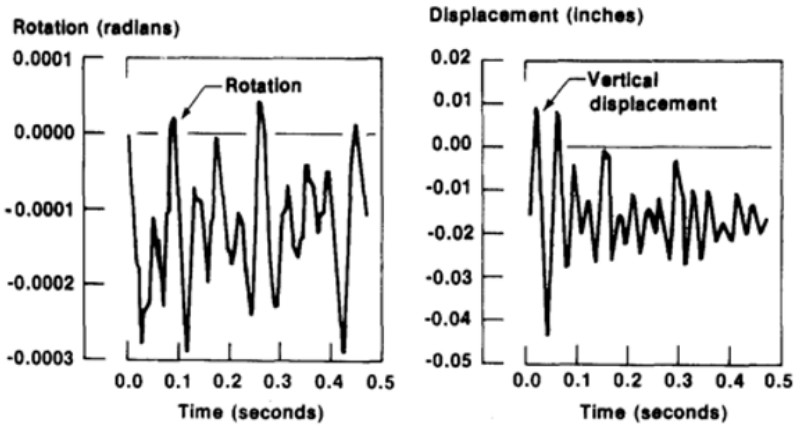

Figure 66. LOCA-induced time-dependent rotation and vertical displacement of the RPV centerline (Cloud 1978).

average horizontal loads provided by Cloud (1978).

5.2.2 SSE

At this time, seismic loads caused by an earthquake are not analyzed in this report. Determination of the loads requires a complex analysis of the reactor system's response to an hypothetical earthquake, including site-specific data, soil-structure interaction, and reactor component design.

5.3 SUPPORT SYSTEM CAPACITY

5.3.1 Anchorage Failure Modes

The shoe support system relies on a steel plate to transfer the vertical downward force exerted by the RPV and nozzle system, as well as seven long anchors (diameter $2\frac{3}{4}$ in. [$\sim$ 7 cm], approximate length 2 ft [$\gtrsim$ 60 cm]) to transfer shear force to the CBS wall. The anchor centers are aligned at a distance of $23\frac{3}{4}$, which is also close to 60 cm. The height of the support box for the nozzle is 23 in. Hence, the horizontal force creates a bending moment at the location of the interface between the bottom steel plate and the supporting concrete.

Unfortunately, the embedded reinforcement details could not be found in the public literature at this writing. The presence of reinforcement through the thickness of the concrete below the support plate plays an important role in the shear strength of an anchor group near a concrete edge (Sharma, Eligehausen, and Asmus 2017; Bokor, Sharma, and Hofmann 2020).

Different failure modes can be hypothesized (see Figure 67 for details):

Concrete edge failure develops from the external anchors towards the edge of the concrete. The angle between the concrete edge and the fracture is approximately 30 degrees (Sharma, Eligehausen, and Asmaus 2016). In the absence of reinforcement, the shear capacity is governed by the geometry of the fracture surface and the shear strength of plain concrete. A similar fracture mode can occur with stirrups which significantly increase the shear capacity of the anchored system (Sharma, Eligehausen, and Asmus 2017).

Stirrup failure (yielding) may occur when the tensile stress in the reinforcing bars is exceeded.

Concrete crushing may also occur beneath the box's bottom steel plate. This effect is aggravated by the bending moment caused by the horizontal force applied at the top of the shoe box. If only plain concrete is considered, then the compression stresses under the plate near the concrete edge may lead to a wedge-type fracture toward the cavity. To reach concrete failure by crushing, reinforcement tying the hypothetical wedge is needed.

Pry-out failure may occur as the result of a rotation of the anchor.

The irradiation-induced damage may affect a portion of the concrete located directly under the support plate near the reactor cavity.

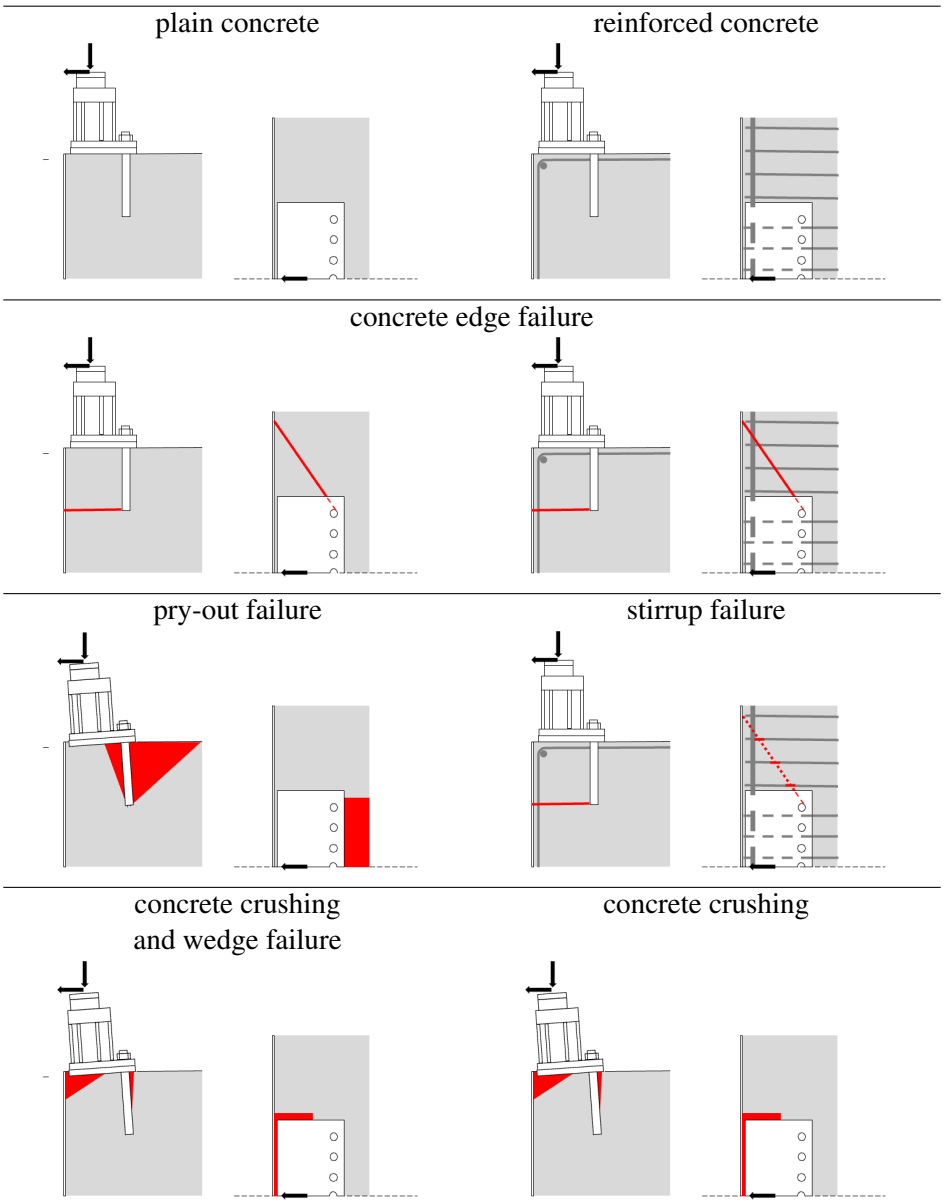

Figure 67. Hypothetical failure modes of the (reinforced) concrete below the nozzle shoe support.

5.3.2 Effects of Irradiation

The effects of irradiation on the concrete located below the support system depend on its elevation relative to the elevation of the fuel at mid-core.

5.3.3 Analytical Expressions

5.3.3.1 Notations

A_s: area of a single reinforcement bar
a: bottom steel plate width (hoop direction)
b: bottom steel plate length (radial direction)
c: horizontal distance of the anchor bolts to the concrete edge
c': horizontal distance of the anchor bolts to the bottom steel plate edge
c_1: concrete cover (to center)
d: embedded depth of the anchors
δ: irradiation-induced depth
f_c: concrete compressive strength (cylinder)
$f_{c,c}$: concrete compressive strength (cube)
f_y: steel yield strength
ϕ_s: reinforcement diameter
s_t: reinforcement spacing

5.3.3.2 Concrete Edge Failure

Plain Concrete

The hypothetical shear failure mode only accounts for the effects of the horizontal load H. The assumed failure occurs along three planes: one horizontal plane located at the elevation of the bottom of the anchors, and two lateral outward planes. The three shear planes form a trapezoidal prism sloping toward the reactor cavity. The lateral planes meet the concrete edge at an estimated distance of approximately $1.5c$ (Sharma, Eligehausen, and Asmaus 2016). See Figure 68 for details. The back of the prism fails in tension. Denoting τ_s and f_t, the shear and tensile strength of plain concrete, the shear capacity reads: $\bar{V} = f_t ad + \tau_s \left(\sqrt{13} cd + ac + \frac{3}{2} c^2 \right)$. Assuming that τ_s is approximately 3 MPa, neglecting the contribution of tension resistance, and considering that $c \simeq h \simeq 0.6$ m, the edge failure shear resistance of this anchored system is approximately 8.75 MN considering only the plain concrete contribution.

Assuming that irradiation-induced damage causes the formation of a damage depth (δ) considered constant in the region of the edge failure, the variation of shear capacity evolves linearly with δ when the tensile resistance of the back plane is not considered: $\frac{\Delta \bar{V}}{\bar{V}} = -\frac{\delta}{c}$

The presence of reinforcements is necessary to provide resistance in the concrete supporting the shoe-type support system. The details of the reinforcement are not known to date. Therefore, only a theoretical analysis can be presented at this time. Details are provided in the paragraph below.

Reinforced Concrete

The contribution of the horizontal bars to the resistance of the wedge failure is the sum of the hook and bond capacities for each bar crossing the failure plane. The hook capacity depends on the location (l) of the failure crack relative to the hook, specifically relative to the concrete cover of the vertical reinforcement, denoted as c_1. According to Sharma, Eligehausen, and Asmaus (2016), "Any stirrup that is not intercepted by the crack or whose anchorage length in the assumed breakout body is $\leq 4\phi_s$ does not contribute towards the load carrying capacity of the anchorage." For illustration, assuming that the concrete

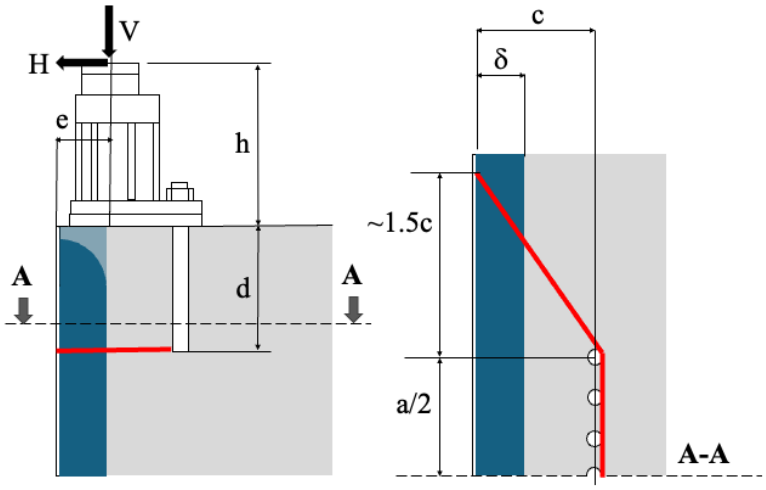

Figure 68. Concrete edge failure (red) and in-service irradiation damage (blue).

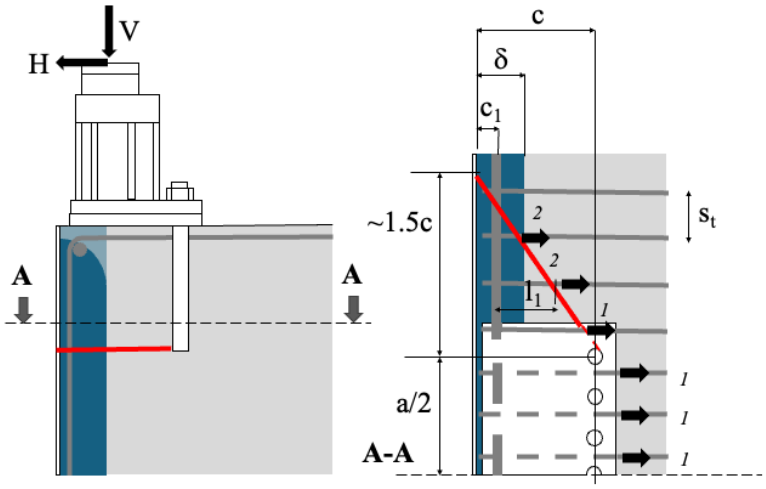

Figure 69. Concrete edge failure of reinforced concrete (red) and in-service irradiation damage (blue).

cover is approximately 7 cm and the bar diameter is 25 mm, if the crack intercepting the rebar is located less than $7 + 2.5 \times 4 = 17$ cm from the concrete edge, then it does not contribute to the anchor capacity.

The hook contribution of each bar is determined by $N_{hook} = \Psi_1\Psi_2\Psi_3 A_s f_y \left(f_{c,c}/30\right))^{0.1}$, where Ψ_1 accounts for the influence of the reinforcement position relative to the crack, and
Ψ_1 is equal to 0.95 for position *1* and 0.16 for position *2* (see Figure 69 for explanation),
Ψ_2 accounts for the influence of the diameter, $\phi_{s,\text{hoop}}$, of the hoop bar forming the hook located at the edge reinforcement as given by $\Psi_2 = \left(\frac{\phi_{s,\text{hoop}}}{\phi_s}\right)^{3/2} \leq 1.2$,
Ψ_3 accounts for the influence of the bond length, l_1, and is given by $\Psi_3 = (l_1/c)^{2/5}(10/\phi_s)^{1/4}$.
$f_{c,c}$ is the mean compressive strength of concrete obtained using 150 mm cubes.
The ratio of the compressive strength of concrete from cylinder to cube specimens can be approximated as $f_c/f_{c,c} \sim 0.8$.

The contribution of the bond of one bar is given by $N_{\text{bond}} = \pi(l_1 - 4\phi_s)\phi_s\bar{\tau}_b$, where $\bar{\tau}_b$ is the mean bond strength between the concrete and the bar.
$\bar{\tau}_b$ is approximately twice the value of the design's bond strength.

The total anchor group capacity is the sum of the hook and bond resistance of the contributing bars that tie the cracking planes. The specific total anchor group capacity depends on the geometry of the support system and the steel and concrete properties. For the sake of illustration, a calculation is presented assuming the following values:
Steel yield strength (f_y): 414 MPa (grade 60).
Concrete compressive design strength (cylinder, f_c): 25 MPa. The corresponding compressive strength obtained on cube specimen ($f_{c,c}$) is approximately 30 MPa.
Steel–concrete bond strength (τ_b): 5 MPa. Reinforcement spacing: 25 cm (approximately 10 in., which is also the spacing between the anchors).
Reinforcement diameter (all directions): 25 mm.
Concrete cover to the hoop reinforcement center: 7 cm.
Layers of rebar in the height of the wedge: 3 (spacing 25 cm).
Note that these values are hypothetical and need to be established from construction drawings that are not readily available at this date. For each layer, after calculation, the total capacity is 9.3 MN.

The possible effects of the irradiation-induced damage depth on the anchor group capacity for this failure mode are as follows:
(1) If the damage depth exceeds the the location of the hook, then the contribution of the hook capacity should not be considered. The calculation hypothesis provided above implies a reduction of the total anchor group capacity of $\approx -40\%$ if the damage depth at the elevation of the contributing reinforcing bars reaches or exceeds approximately 7 cm.
(2) The bond capacity will also be affected if the irradiation-induced damage depth exceeds the location of the hook because it will reduce the bond length denoted l_1.

5.3.3.3 Concrete Crushing

Pure Flexural Mode

In pure flexure, only the effect of the horizontal load on the bending moment is considered. The resisting bending moment is estimated by $\bar{\mathcal{M}}_r = 0.8\Psi f_c bx(c' - x/2)$, where f_c is the compressive strength of concrete, and bx is the area under the plate subject to compression. The value of x is determined assuming that the deformation field under the plate is linear and that the maximum allowable compression strain in concrete is $\varepsilon_{c,u} = 0.35\%$. The balance of forces[4] between the anchors in tension and the concrete in compression

4. $0.8\Psi f_c bx = nE_s\varepsilon_s A_s$ with n the number of anchors and E_s the Young's modulus of steel. The tensile strain in the steel anchors is determined by $\varepsilon_s = \varepsilon_{c.u}(c' - x)/x$.

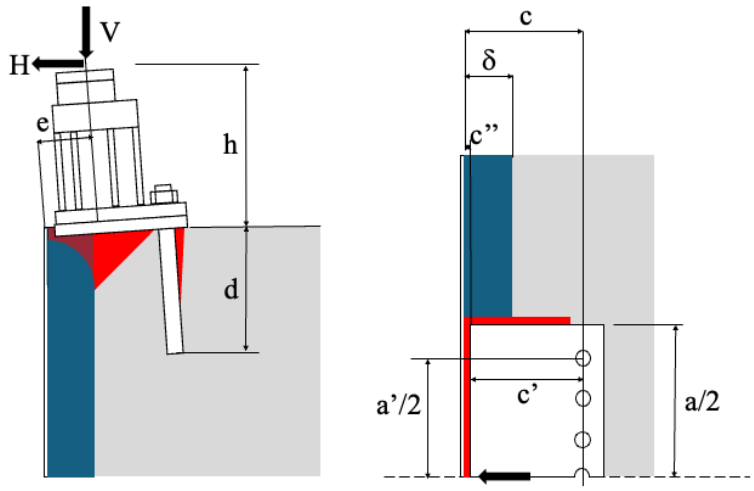

Figure 70. Concrete crushing failure (red) and in-service irradiation damage (blue).

leads to $x \sim 0.4$ m. The value of $\bar{\mathcal{M}}_r/h$ is ~ 6.24 MN.

The irradiation-induced damage depth reduced the load transmission area under the bottom plate of the support shoe box. Assuming a maximum damage depth of 20 cm, the value of $\bar{\mathcal{M}}_r/h$ is reduced to 2.9 MN. The horizontal load capacity for intermediate values of irradiation-induced damage depth is provided in the summary presented at the end of this chapter. The anchors remain in the elastic regime for all studied cases.

5.3.3.4 Pry-out failure

The study of the pry-out failure mode was studied using LDPM. Methods and results are provided in the next section

5.3.4 Numerical model

As mentioned above, data about the system reinforcement and dimensions are not known at this date. Therefore, the simulation presented here is based on the following simplifying assumptions:

1. CBS reinforcement is not represented.
2. Symmetry boundary conditions are assumed, so only one half of the support is simulated.
3. To limit computational cost, only 45^o angle of the CBS is considered.
4. The support block and anchors are simulated using hexahedral finite elements with elastic steel properties.
5. The LDPM is used to simulate the concrete around the support block, extending 91.44 cm (3 ft) radially behind the block and 152.4 cm (5 ft) below the bottom of the support block (91.44 cm or 3 ft below the tips of the anchors). The remainder of the wedge is simulated using hexahedral finite elements with elastic concrete properties.
6. To reduce computational costs, the effects of irradiation on concrete damage are considered by neglecting the contribution of (deleting) the innermost LDPM elements within 10, 15, and 20 cm from the inner surface of the CBS facing the RPV cavity.
7. A very coarse concrete mix design was used in this model with a maximum aggregate size of 50 mm and a minimum aggregate size cutoff at 25 mm. Details of the model calibration are presented next.

The model geometry is shown in Figure 71. The gray-colored part represents the LDPM model and is shown partially transparent to reveal the internal idealized spherical aggregate. The support block and anchors are colored red, and the remaining volume of the simulated CBS wedge is colored blue.

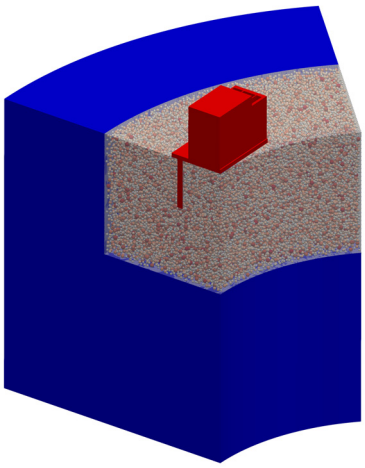

Figure 71. A 45^o wedge model of the CBS showing LDPM (opaque gray) with internal aggregate, along with the support block (red) and the surrounding elastic concrete (blue).

5.3.4.1 Lattice Discrete Particle Model Overview

An overview of LDPM can be found in **lepape2023-tm-cbempty citation**.

Model Calibration

Because material data are limited and only the compressive strength is known, the same procedure detailed in Alnaggar and Bhanot 2018 is used here. Assuming actual $f_c = 30$ MPa and using ACI 318-19 2019, estimates of elastic modulus $E_c = 25,907$ MPa and splitting tensile strength $f_{sp} = 3.0672$ MPa can be obtained. For a normal concrete with a Poisson's ratio of 0.19, LDPM elastic parameters can be computed following Cusatis, Pelessone, and Mencarelli 2011, which gives $\alpha = 0.25$ and $E_0 = 40,040$ MPa. To determine strength parameters, it is first assumed that the mesoscale tensile strength is equal to the splitting tensile strength $\sigma_t = f_{sp} = 3.0672$ MPa. Then, the tensile characteristic length l_t is to be calculated from the mesoscale fracture energy G_t, which was show to be equal to the initial fracture energy G_f Alnaggar and Bhanot 2018. Using a maximum aggregate size of $d_a = 50$ mm, a water-to-cement ratio of $w/c = 0.5$, and $f_c = 30$ MPa, the initial fracture energy can be estimated following Bažant and Becq-Giraudon 2002, giving $G_f = 33.579$ N/m. This gives $l_t = 285.82$ mm. It only remains to calibrate the mesoscale shear strength σ_s using simulations of uniaxial compression tests of standard 6×12 in. cylinders. Given the coarse aggregate size used, four randomly generated cylinders were simulated, and $\sigma_s = 11.87$ MPa was calibrated to achieve an average $f_c = 30$ MPa, as shown in Figure 72.

Using these calibrated parameters, the model shown in Figure 71 is used to perform push-over analysis with and without vertical loads.

Push-over analysis under horizontal loads only

Here, a monotonically increasing horizontal load is applied to the top of the support plate. The failure surface is a combination of pry-out and concrete edge failure where the anchors form a concrete cone that initiates a crack surface starting at the anchor tip and propagating to the surface. Because of the compression from the edge of the support block on the interior edge of the CBS, the crack propagates nearly

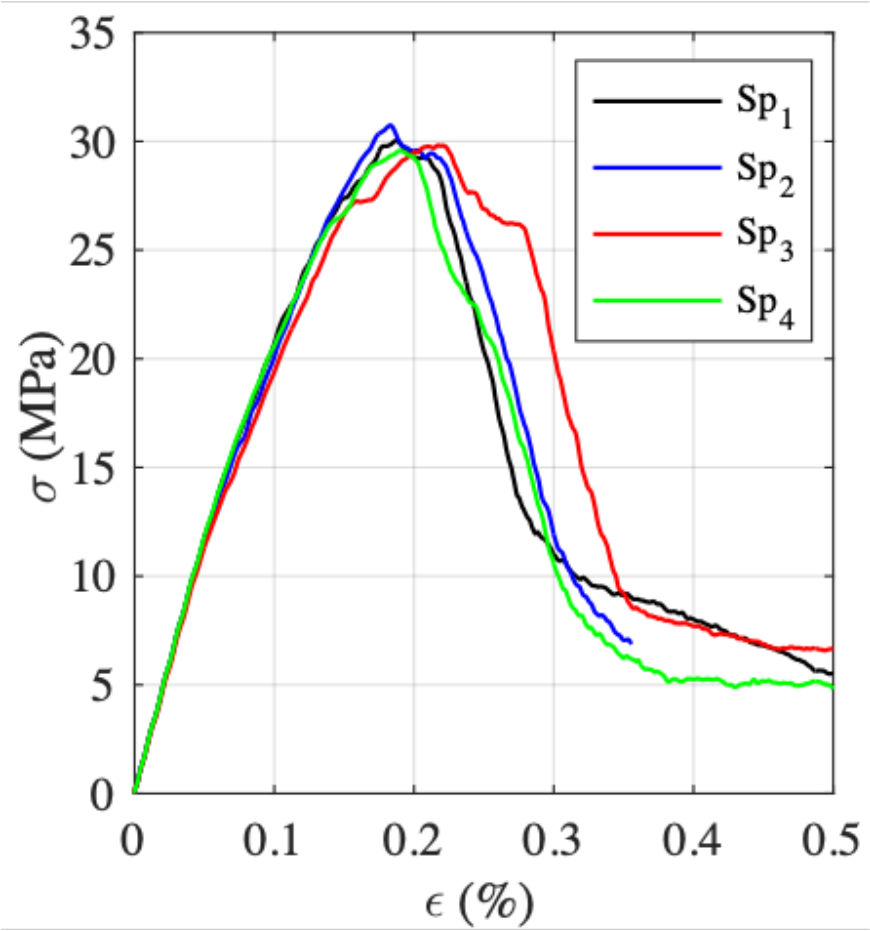

Figure 72. Calibrated uniaxial compressive response of four 6×12 inch cylinders.

horizontally under the block zone. The estimated peak load in this case is approximately 3.26 MN. At this peak load, Figure 73 shows the system colored by the displacement magnitude. Crack traces can be seen in Figure 74. The formed crack surface is shown in Figure 75. At this peak load, while anchors are under significant tension caused by support block rotation, none of the anchors yield, as illustrated by the Von Mises stress distribution shown in Figure 76, where the color bar's upper limit is 414 MPa, which is the steel yield strength (Grade 60). This indicates that as long as the 2 ft length of the anchors is adequate for full development, then the resulting peak load and failure mode can be considered realistic.

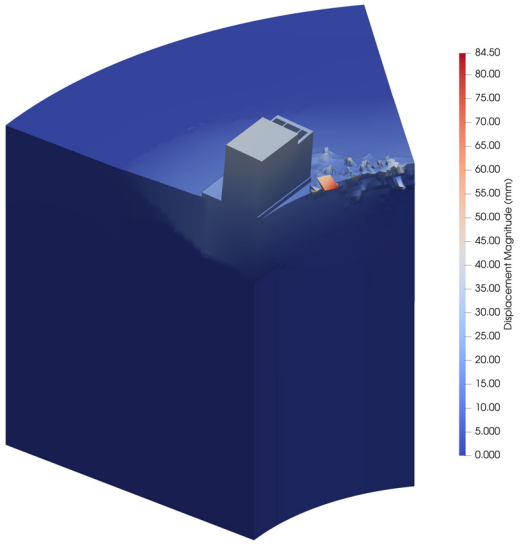

Figure 73. CBS wedge displacement at a peak horizontal load of 3.26 MN without applied vertical loads.

To account for irradiation-induced damage effects in a simplified manner, the innermost LDPM elements are neglected. This is done here solely to reduce the computational cost and to provide insight into the possible conservative failure mechanisms. Three explicit damage depths are simulated, including 10, 15, and 20 cm from the inner surface of the CBS facing the RPV cavity, as shown in Figure 77.

The partial loss of support under the support block results in an increase of its rotation. Although more cracking and damage around the support block can be observed, the mode of failure is still dominated by pry-out. This is expected because the lost elements shorten the lever arm between the compression zone under the support block and the anchors causing higher tensile forces in the anchors and higher compression under the plate at the same horizontal force. Crack traces on the wedge surface, as well as the internal crack, surface are shown for the 20 cm damage depth case in Figure 78. Similar crack patterns were observed for 10 cm and 15 cm damage depths. The horizontal peak load capacities for all push-over cases without applied vertical loads are presented in the first column of Table 7.

Push-over analysis under vertical and horizontal loads

Here, a vertical load of 5.0 MN representing the vertical reaction of the RPV is first applied to the top of the support block. Then, a monotonically increasing horizontal load is applied to the top of the support block in a manner similar to that appplied in the case without vertical loads. The failure surface is similar to the previous case, showing a combination of pry-out and concrete edge failure where the anchors form a concrete cone that initiates a crack surface starting at the anchor tip and propagating to the surface. The

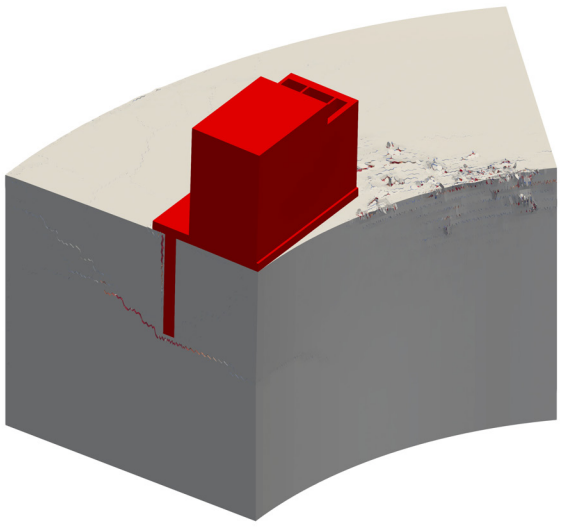

Figure 74. CBS wedge crack traces on the surface at a peak horizontal load of 3.26 MN without applied vertical loads.

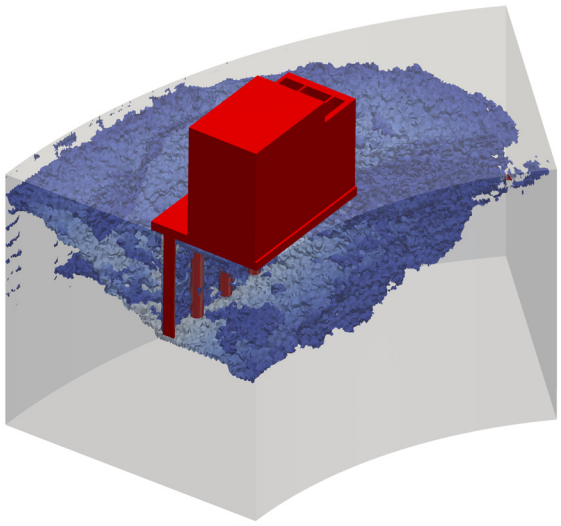

Figure 75. CBS wedge crack surface at a peak horizontal load of 3.26 MN without applied vertical loads.

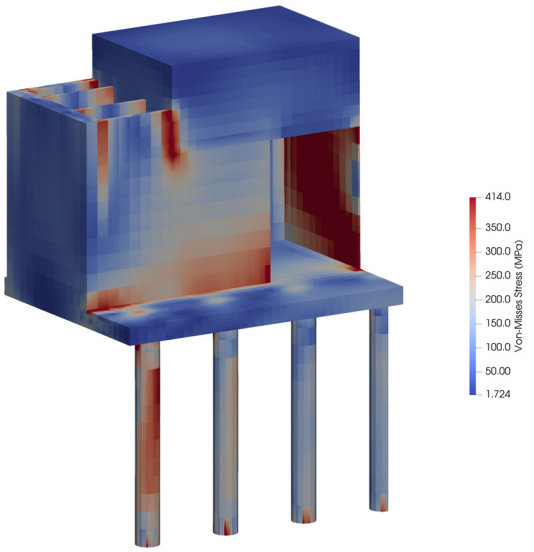

Figure 76. Von Mises stress distribution within the support block showing no yielding of the anchors at a peak horizontal load of 3.26 MN without applied vertical loads.

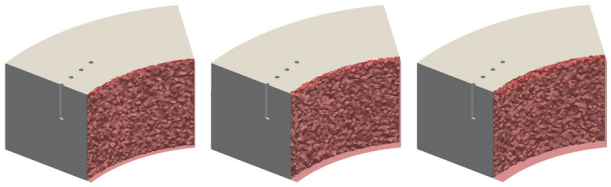

Figure 77. LDPM model geometry showing the removed elements (opaque red) to represent damage depths of 10 cm (left), 15 cm (middle), and 20 cm (right).

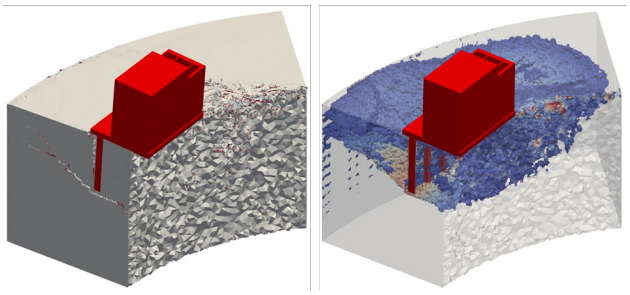

Figure 78. CBS wedge with 20 cm damage depth showing crack traces on the surface (left) and interior crack surface (right) at a peak horizontal load of 2.06 MN without applied vertical loads.

main difference here is that the presence of an additional vertical load increases the compression zone under the support block and also increases the concrete's internal friction. This is why the simulations show a higher peak load capacity of 4.25 MN as compared to 3.26 MN without vertical loads. The increase of horizontal load capacity can be understood by observing that the compression from the edge of the support block (increased by the combination of bending and vertical loads on the interior edge of the CBS) increases friction along the crack which in turn propagates nearly horizontally under the block zone. At this peak load, Figure 79 shows the system colored according the displacement magnitude, Figure 74 shows crack traces on the wedge surface, and Figure 75 shows the formed internal crack surface. These figures show that the additional compressive force prevented the horizontal crack that initiated at the anchor tip from fully propagating to the internal CBS surface. Instead, an additional vertical crack propagated also at the anchors' tips. This is because the support block is attached better to the concrete block beneath it, and the blocks tend to move together.

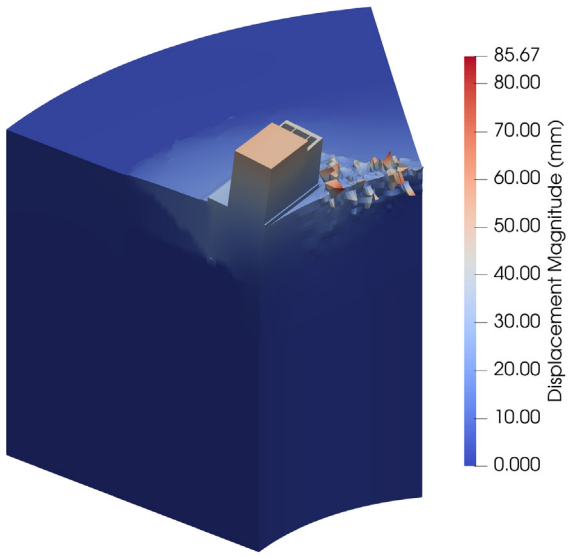

Figure 79. CBS wedge displacement at a peak horizontal load of 4.25 MN with applied vertical loads.

The effects of irradiation were simulated in a similar manner by removing the innermost LDPM elements, and the results show similar trends in terms of preventing the propagation of a horizontal crack beneath the support block and initiating a vertical crack at the tips of the anchors. Figure 82 shows surface and interior cracks for the 20 cm damage depth case under vertical loads, thus illustrating the observed cracking trends. Note that crushing under the support block can be observed. However, the compression-induced vertical crack suggests that an extended concrete volume participated in resisting the lateral loads, which explains the higher horizontal load capacity of 2.61 MN compared to 2.06 MN for the same damage depth without vertical loads. The horizontal peak load capacities for all push-over cases with applied vertical loads are presented in the second column of Table 7.

Observations and limitations of the numerical simulations

These numerical simulations using LDPM provide important insights into the possible complex interactions between the support block and the CBS. When compared to analytical postulated failure modes, it was shown that ultimate failure is initiated by pry-out, followed by crack propagation from the tip of the

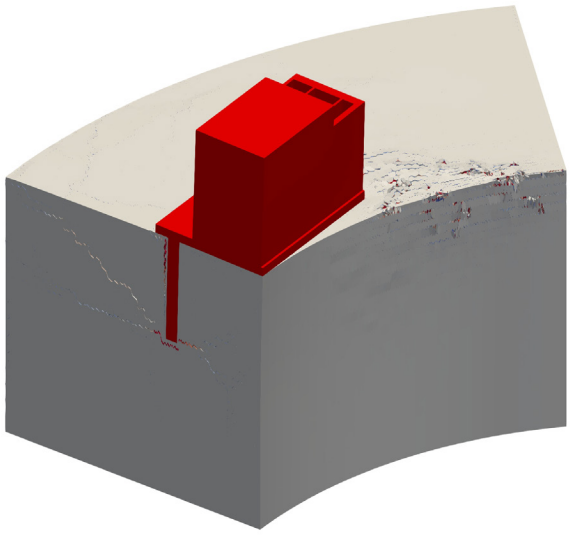

Figure 80. CBS wedge crack traces on the surface at a peak horizontal load of 4.25 MN with applied vertical loads.

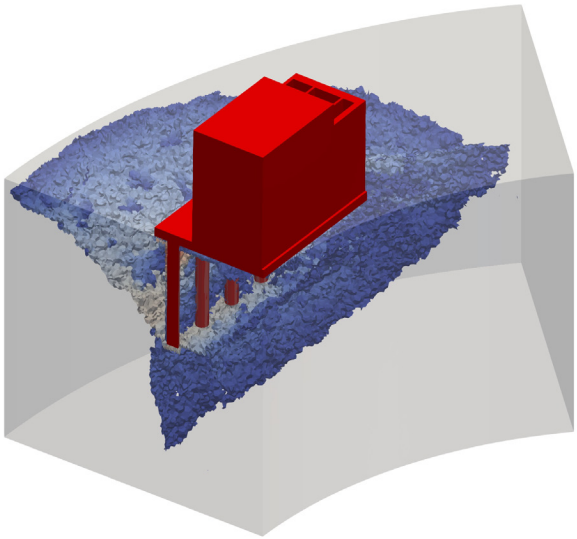

Figure 81. CBS wedge crack surface at a peak horizontal load of 4.25 MN with applied vertical loads.

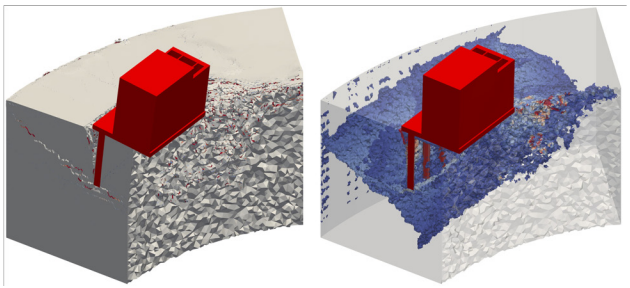

Figure 82. CBS wedge with 20 cm damage depth showing crack traces on the surface (left) and interior crack surface (right) at a peak horizontal load of 2.61 MN with applied vertical loads.

Table 7. Results of the LDPM simulations. Horizontal load capacity with increasing irradiation-induced damage depth

Damage depth (cm)	$\bar{H}(V = 0)$ (MN)	$\bar{H}(V > 0)$ (MN)
0	3.26	4.25
10	2.68	3.46
15	2.40	2.98
20	2.06	2.61

anchor group. This crack propagation is nearly horizontal and reaches the inner surface of the CBS when no vertical loads are applied. When vertical loads representing the RPV vertical reaction are applied, the propagating crack becomes vertical initially, and then it branches as a result of the high compression under the support block. It is important to note that the wedge analysis with proper boundary conditions allowed for capturing the CBS ring action effects on the propagation of cracks on the sides of the support block, thus causing their surfaces to follow a curved path rather than a straight path at an angle as had been assumed in the analytical solutions. These observations show the benefits and depth of understanding that could be obtained when such high-fidelity modeling is used.

However, it must be noted that simplifying assumptions of the model and neglecting the CBS reinforcement made the model predictions lower than a number of analytical solution cases. For example, horizontal reinforcement was expected to confine the top surface. Together with its contribution as ties, this would have provided additional horizontal force resistance. Additionally, vertical reinforcement at the internal edge of the CBS would have also reduced edge crushing. These effects and contributions can be easily accounted for once detailed reinforcement information is obtained.

5.3.4.2 Summary

The bearing capacity of a shoe-type nozzle support system was studied, with various failure modes of plain and reinforced concrete considered. Figure 83 summarizes the results of the analytical calculations and simulation results obtained with LDPM for different failure modes, including plain concrete crushing, plain or reinforced concrete wedge failure, and pry-out failure (white diamonds indicate damage without considering the vertical load, and black diamonds indicate damage considering the vertical load). The red lines correspond to the jet thrust force obtained using RELAP5-3D for a full break area (1A) or a partial break area (0.5A, i.e., at 50

The horizontal load applied to the support system depends on the actual break area, the dynamic response of the reactor system during LOCA, and specific design details of the support system that permit relative

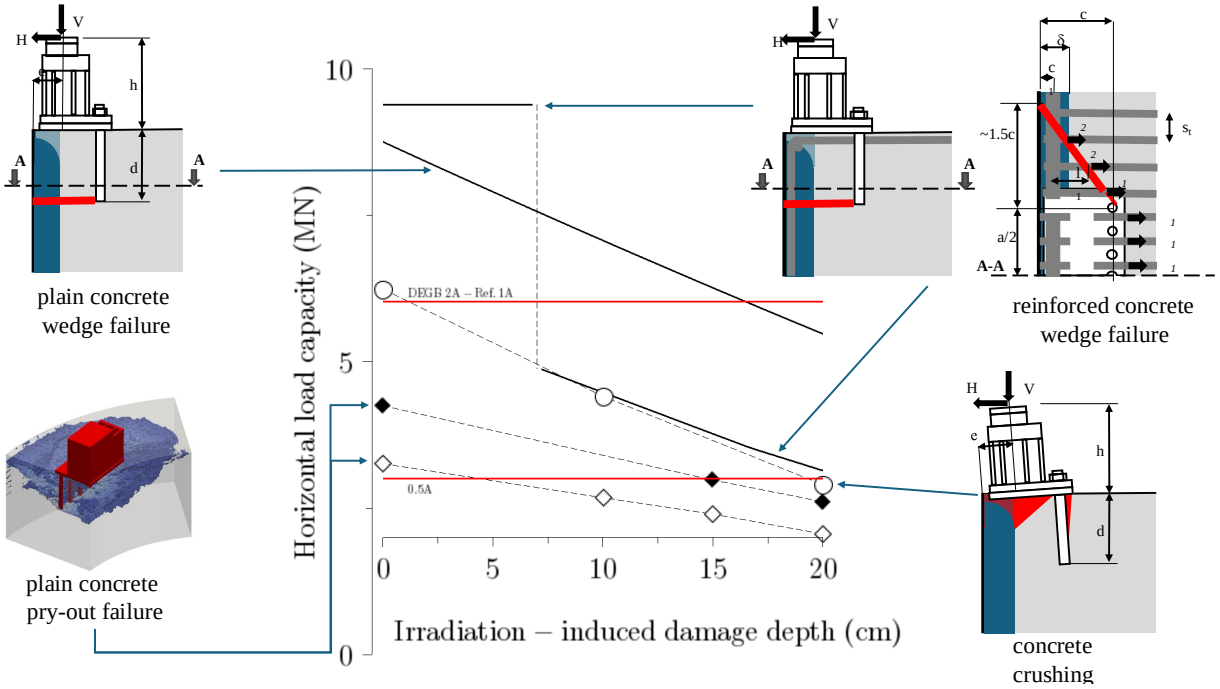

Figure 83. Evolution of the horizontal load capacity with the irradiation-induced damage depth.

free deformation of the nozzle. The jet thrust–induced horizontal load of approximately 6 MN at full break is considered an upper bound value. Assuming this value as the design accidental load, the structural safety margin of the unirradiated concrete is minimal for the crushing concrete mode. The presence of reinforcement (e.g., stirrups not modeled in the crushing failure mode) may provide additional concrete confinement and resistance, thus improving the bearing capacity of the edge concrete.

The calculated safety factor for the wedge failure mode of the unirradiated reinforced concrete is approximately 1.5.

The bearing capacity obtained by LDPM, assuming plain concrete during the pry-out failure mode, is lower than that of the design load. Evidently, the presence of reinforcement is expected to significantly improve the overall bearing capacity. Further studies are needed.

The effects of irradiation were considered assuming a uniform damage depth with elevation. This hypothesis is conservative. Figure 84 shows the fast neutron flux profile with height that was obtained by Remec (2013) using the irradiation transport code MCNP and the corresponding irradiation-induced damage depth obtained using the 1D-SAM presented in Section 4. The profile of irradiation-induced damage depths exhibits a sharp change above approximately 1.5 m from the fuel core mid-elevation. Based on data provided in NUREG/CR-7280 (Biwer et al. 2021), the blue-shaded area in Figure 84 indicates the estimated range of elevations of the support system for varied designs. Each configuration is specific to the geometry of the reactor cavity. Hence, it is conservative to assume a uniform damage depth in the concrete region bordering the cavity below the support system. With increasing damage depth, the bearing capacity of the concrete gradually decreases for all failure modes except the wedge failure mode of reinforced concrete. In this case, once the damage depth reaches the reinforcement, the hook bond resistance is considered lost; hence, a sudden drop in bearing capacity is observed. However, the bearing capacity of plain concrete mitigates this effect, ensuring sufficient bearing capacity. The loss of load capacity caused by irradiation-induced damage may be the limiting factor for such a support system design.

Additional LDPM simulations accounting for a realistic reinforcement layout are needed to obtain more reliable estimates of the residual bearing capacity of the shoe support system. Whereas previous studies show that the irradiation-induced damage marginally affected the over-designed bearing capacity of the CBS, the coefficient of structural safety of the studied structural support system appears to be limited.

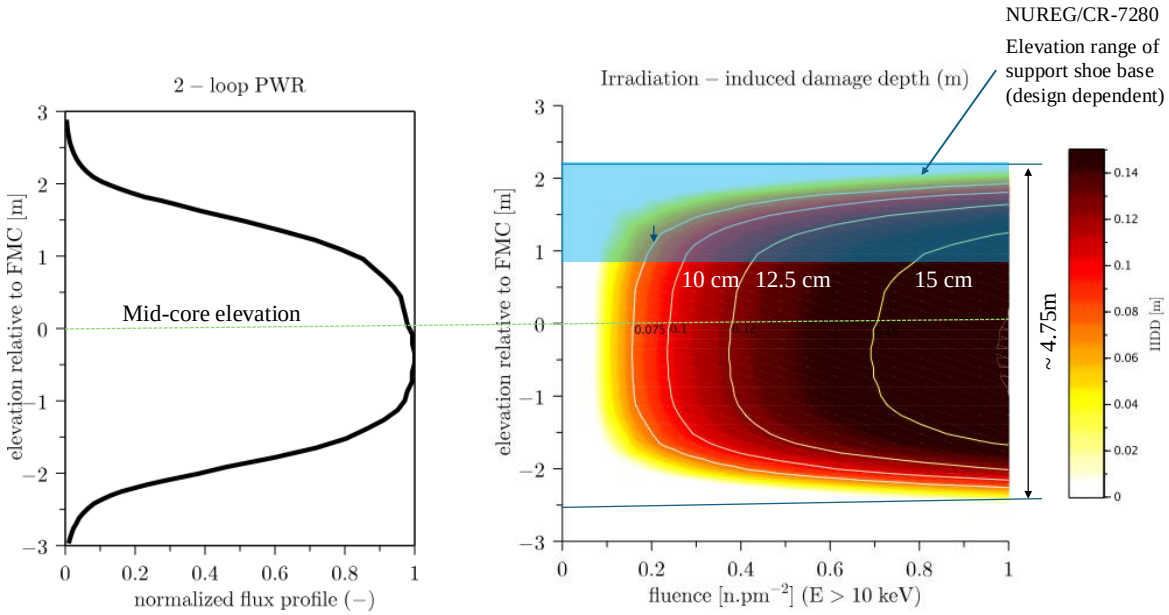

Figure 84. Fast neutron flux profile and irradiation-induced damage estimates with elevation.

6. CONCLUSIONS

This report presents the analysis of the effects of a LOCA on the structural performance of a PWR CBS, accounting for the in-service irradiation-induced damage that occurs during normal operation.

The irradiation-induced damage is characterized by a damage depth which is determined using 1D-SAM simulations for computational efficiency. The 1D-SAM method was cross-validated against advanced nonlinear simulation techniques, including FEA, using the Grizzly code and LDPM. At the elevation of the core's mid-fuel level, the in-service irradiation-induced damage increases monotonically with an onset at about 0.5×10^{19} n.cm^{-2} ($E > 10$ keV). The damage depth rate decreases with increased fast neutron fluence. The 1D-SAM method makes it possible to account for the aggregate's mineral composition. The full extent of the composition spectrum of magmatic rocks was studied. At 7×10^{19} n.cm^{-2}, which is about the maximum estimated fluence at 80 years of operation across the US PWR fleet, the irradiation-induced damage depth ranges from approximately 12.5 cm to 15 cm. In addition, a bounding case scenario considering 92% quartz content (metachert–JCAMP) was studied. At the same fast neutron fluence, the corresponding damage depth reached approximately 17.5 cm.

The temperature and pressure conditions resulting from a hypothetical LOCA were studied using the RELAP5-3D code. A nozzle break releases steam into the reactor cavity, which gradually fills the cavity and connected volumes, including the containment building. Pressure spikes within the first 1 s following the nozzle failure, reaching a high pressure greater than 1 MPa. At approximately 20 s after the nozzle failure, the pressure drops to a steady value of approximately 4 bars in both the cavity and the containment building. The temperature in the cavity follows a similar trend. A sudden temperature spike near 300 °C lasts for about 20 s, after which the temperature drops to a near-steady regime of approximately 120 °C. After one minute, the temperatures in the reactor cavity, refueling cavity, and containment building reach similar values. The peak pressure and temperature values depend on the location of the nozzle break. As the break location moves further from the RPV, the steam flow is partly diverted toward adjacent volumes, thus reducing the pressure and temperature in the cavity. The steam jet at the break creates a thrust, applying a horizontal load with a value estimated at approximately 6 MN in the worst-case scenario.

The study of the effects of LOCA-induced pressure and temperature on the structural performance of the CBS consisted of two parts. First, the possible extension of the in-service irradiation-induced damage depth was analyzed using the same 1D-SAM method, which was cross-validated against the LDPM. A parametric study was conducted to account for the variability of pressure and temperature in the cavity during a LOCA. In the range of conditions studied, the extension of the damage depth was limited to an additional 4 cm. Second, an analysis was performed on the effects of a LOCA on the performance of the RPV support systems. Note that this part of the study specifically addressed the interactions between the support system and the surrounding concrete which may have been damaged from extended irradiation. Because there is a wide variety of support systems, they were grouped into categories of low, moderate, and high susceptibility to concrete irradiation-induced damage. The most susceptible systems are the shoe-type and cantilever beam supports, both of which are essential for transferring vertical and horizontal loads from the RPV to the CBS. These systems are either directly resting on or embedded in concrete areas that are potentially subject to irradiation-induced damage.

A structural analysis of a shoe support system based on the design drawing of Farley nuclear power plant (NPP) was conducted. Because the reinforcement details are not known to date, the analysis only aimed at providing methodological guidance of the structural capacity of the support system against horizontal loads occurring during accidental conditions. Several failure modes were studied using analytical and numerical analysis, including horizontal wedge formation, concrete crushing below the bottom shoe plate,

and pry-out failure. With the assumptions made about the reinforcement layout, it was found that the the concrete crushing failure wedge failure mode is more detrimental than the wedge failure mode for unirradiated concrete. The pry-out failure mode leads to the lowest load capacity, but the simulations do not account for the presence of the reinforcement. The development of the irradiation-induced damage depth causes a reduction of the structural capacity of the nozzle support system. The wedge failure mode analysis indicated a structural capacity approximately 1.5 times higher than the jet thrust estimated from the results of the RELAP5-3D simulation for the maximum break area. However, when the irradiation-induced damage depth reaches the location of the hoop reinforcement in the CBS, the hook resistance of the reinforcing bars tying the lateral wedge cracks can no longer be considered, thus leading to a significant loss in the structural capacity of the support system against horizontal loading. This loss of reinforcement resistance, however, may be compensated by the shear resistance of plain concrete. The safety factor, however, may be reduced to approximately 1.25. Finally, the numerical simulation conducted on plain (unreinforced) concrete showed a pry-out failure mode occurring at a relatively low horizontal load. The role of the reinforcement should be studied further in simulations to be conducted in FY25. To complete the required probabilistic analysis for this research, realistic reinforcement details from plant owners will be needed. The safety factor relative to the integrity of the irradiated concrete support shoe-type system during an accident appears to be limited.

7. REFERENCES

ACI 318-19. 2019. *Building Code Requirements for Structural Concrete.* ACI 318-19.

Alnaggar, M., Y.-J. Choi, and Y. Le Pape. 2023. *Assessment of the Effect of the In-Service Irradiation-Induced Degradation on the Structural Performance of Biological Shields during a Loss of Coolant Accidents.* Technical report ORNL/SPR-2023/3158, M3LW-23OR0403043. Oak Ridge National Laboratory.

Alnaggar, Mohammed, and Naina Bhanot. 2018. "A machine learning approach for the identification of the Lattice Discrete Particle Model parameters." *Eng. Fract. Mech.* 197 (June): 160–175.

Andreev, V.I., and D.A. Kapliy. 2014. "Stress-State of a Thick-Walled Cylindrical Shell under the Combined Action of Radiation and Temperature Field." *Advanced Materials Research* 1006-1007:177–180.

Basta, L. 2023. *Revision to Reactor Vessel Surveillance Capsule Withdrawal Schedule.* Technical report RA-23-0141. US Nuclear Regulatory Commission.

Bažant, Zdeněk P, and Emilie Becq-Giraudon. 2002. "Statistical prediction of fracture parameters of concrete and implications for choice of testing standard." *Cem. Concr. Res.* 32, no. 4 (April): 529–556.

Beaver Valley Power Station, Unit No. 2. 2014. *Updated Final Safety Analysis Report, revision 16, Chapter 6.* Technical report NRC ADAMS ML14339A412. Vistra.

Beukelmann, D., W. Guo, W. Holzer, R. Kauer, W. Münch, C. Reichel, and P. Schöner. 2012. "Safety Assessment of Reactor Pressure Vessel Integrity for Loss of Coolant Accident Conditions" [in eng]. *Journal of pressure vessel technology* (New York, NY) 134 (1). ISSN: 0094-9930.

Biwer, B., D. Ma, J. Xi, and Y. Jing2. 2021. *Review of Radiation-Induced Concrete Degradation and Potential Implications for Structures Exposed to High Long-Term Radiation Levels in Nuclear Power Plants.* Technical report NUREG/CR-7280, ANL/EVS-20/8. US Nuclear Regulatory Commission.

Bokor, Boglárka, Akanshu Sharma, and Jan Hofmann. 2020. "Experimental investigations on the concrete edge failure of shear loaded anchor groups of rectangular and non-rectangular configurations." *Engineering Structures* 222:111153. ISSN: 0141-0296. https://doi.org/https://doi.org/10.1016/j.engstruct.2020.111153. https://www.sciencedirect.com/science/article/pii/S0141029619352952.

Bouniol, P. 2004. *State of knowledge on the water radiolysis in cemented waste forms and its approach by simulation.* Technical report CEA-R-6069. In French. CEA / Saclay 91191 Gif-sur-Yvette Cedex France: Commissariat à l'Energie Atomique.

Bouniol, P., and A. Aspart. 1998. "Disappearance of oxygen in concrete under irradiation: the role of peroxides in radiolysis." *Cement and Concrete Research* 28 (11): 1669–1681. ISSN: 0008-8846.

Bowen, N.L. 1913. "The melting phenomenon of the plagioclase feldspars." *American Journal of Science* 35 (4th Series): 577–599. https://doi.org/http://dx.doi.org/10.2475/ajs.s4-35.210.577.

Bruck, P. 2018. *Guidance for Aging Management of Concrete Biological Shields that Utilize a Neutron Shield Tank, Basis for Concrete Biological Shield Wall for Aging Management.* Technical report 3002013051. Electric Power Research Institute.

Bruck, P.M., T.C. Esselman, B.M. Elaidi, J.J. Wall, and E.L. Wong. 2019. "Structural assessment of radiation damage in light water power reactor concrete biological shield walls." *Nuclear Engineering and Design* 350:9–20.

Bykov, V.N., A.V. Denisov, V.B. Dubrovskii, V.V. Korenevskii, G.K. Krivokoneva, and L.P. Muzalevskii. 1981. "Effect of Irradiation Temperature on the Radiation Expansion of Quartz." *Atomnaya Energiya* 51, no. 3 (September): 593–595.

Carolina Power & Light. 2017. *H.B. Robinson Steam Electric Plant, Unit 2, Revision 27 to Updated Final Safety Analysis Report.* Technical report Docket No. 50-261, Hartsville, SC. ADAMS Accession No. ML17298A849 - Chapter 3.

Cheniour, A., E. Davidson, Y. Le Pape, T. Pandya, B. Collins, B. Spencer, A. Godfrey, and M. Asgari. 2023. "A structural model of the long-term degradation of the concrete biological shield." *Nuclear Engineering and Design* 405:112217. ISSN: 0029-5493. https://doi.org/https://doi.org/10.1016/j.nucengdes.2023.112217. https://www.sciencedirect.com/science/article/pii/S0029549323000663.

Cheverton, R.D., W.E. Pennell, G.C. Robinson, and R.K. Nanstad. 1989. *Impact of Radiation Embrittlement on Integrity of Pressure Vessel Supports for Two PWR Plants.* Technical report NUREG/CR-5320, ONRL/TM010966. US Nuclear Regulatory Commission.

Cloud, R.L. 1978. "Structural mechanics applied to pressurized water reactor systems." *Nuclear Engineering and Design* 46:273–302.

Cusatis, G, D Pelessone, and A Mencarelli. 2011. "Lattice Discrete Particle Model (LDPM) for Concrete failure Behavior of Concrete. I: Theory." *Cement and Concrete Composites* 33 (9): 881–890.

Don Fletcher, C., C. B. Davis, and D. M. Ogden. 1985. *Thermal-Hydraulic Analyses of Overcooling Sequences for the H.B. Robinson Unit 2 Pressurized Thermal Shock Study.* Technical report NUREG/CR-3935, EGG-2335. Idaho National Laboratory.

Energy, Duke. 2017. *Updated Final Safety Analysis Report, Revision No. 27, Chapter 6, Engineered Safety Features.* Technical report ADAMS ML17298A855. US Nuclear Regulatory Commission.

Entergy Operations Inc. 2000. "Arkansas Nuclear One - Unit 1 License Renewal Application." (Russellville, AR), no. Docket No. 50-313, ADAMS Accession No. ML003679667.

Esselman, T., and P. Bruck. 2013. *Expected condition of concrete at age 80 of reactor operation.* Technical report A13276-R-001. 36 Main Street, Amesbury, MA 01913: Lucius Pitkins, Inc., September.

Exelon Generation. 2018. "Three Mile Island Nuclear Station, Unit 1, Updated Final Safety Analysis Report (UFSAR), Revision 24 Fire Hazards Analysis Report (FHAR)." (Kennett Square, PA), no. Revision 28 UFSAR and FHAR Reference Drawings Docket No. 50-289, ADAMS Accession No. ML19066A349.

Exelon Generation Company LLC. 2017. *Calvert Cliffs Nuclear Power Plant Units 1 and 2, Updated Final Safety Analysis Report, Revision 49.* Technical report Docket Nos. 50-317 and 50-318, ADAMS Accession No. ML17354B239. Kennett Square, PA.

FENOC. 2024. *Beaver Valley, Unit 2, Submittal of the Updated Final Safety Analysis Report, Revision 21.* Technical report Docket No. 50-412, Shippingport, PA. ADAMS Accession No. ML14339A419. First Energy Nuclear Operating Company.

Framatome. 2021. *Framatome Reactor Vessel and RCP TLAA and Aging Management Review Input to the ONS SLRA.* Technical report ANP-3898NP, Revision 0.

Goldich, S.S. 1938. “A study in rock-weathering.” *The Journal of Geology* 46 (1): 17–58.

Hookham, C.J. 1991. *Structural Aging Assessment Methodology for Concrete Structures in Nuclear Power Plants.* Technical report ORNL/NRC/LTR-90/17. Oak Ridge National Laboratory, March.

Hosford, S.B., R. Mattu, R.O. Meyer, E.D. Throm, and C.G. Tinkler. 1981. *Asymmetric Blowdown Loads on PWR Primary Systems – Resolution of Generic Task Action Plan A-2.* Technical report NUREG-0609. US Nuclear Regulatory Commission, January 1, 1981.

Kambayashi, D., S. Sasano H. Sawada, K. Suzuki, and I. Maruyama. 2020. “Numerical Analysis of a Concrete Biological Shielding Wall under Neutron Irradiation by 3D RBSM.” *Journal of Advanced Concrete Technology* 18:617–632.

Kaplan, M.F. 1971. “Concrete for Pressure Vessels, Shielding and Containment of Nuclear Reactors: A Report on the American Concrete Institute Seminar "Concrete for Nuclear Reactors’; held at the Bundesanstalt für Materialprüfung (BAM), Berlin, 5-9 October, 1970.” *Nuclear Engineering and Design* 16:369–374.

———. 1983. *Nuclear radiation and the properties of concrete.* Technical report No. 35. University of Cape Town.

Khmurovska, Y., P. Štemberk, T. Fekete, and T. Eurajoki. 2019. “Numerical analysis of VVER-440/213 concrete biological shield undernormal operation.” *Nuclear Engineering and Design* 350:58–66.

Le Pape, Y. 2015. “Structural Effects of Radiation-Induced Volumetric Expansion on Unreinforced Concrete Biological Shields.” *Nuclear Engineering and Design* 295:534–548.

Le Pape, Y., M. Alnaggar, and A. Cheniour. 2023. *Assessment of the Effect of the Irradiation-Induced Degradation on the In-Service Structural Performance of the Concrete Biological Shields.* Technical report ORNL/SPR-2023/3031, M3LW-23OR0403013. Oak Ridge National Laboratory.

Le Pape, Y., M.H.F. Alsaid, and A.B. Giorla. 2018. “Rock-forming minerals radiation-induced volumetric expansion – Revisiting the literature data.” *Journal of Advanced Concrete Technology* 16:191–209. https://doi.org/10.3151/jact.16.191.

Le Pape, Y., S. Sabatino, and E. Tajuelo Rodriguez. 2023. *Effects of Aggregates Mineralogy on the Irradiation-Induced Damage in Concrete Biological Shields.* Technical report ORNL/SPR-2023/2912. Oak Ridge National Laboratory.

Lobner, P., C. Donahoe, and C. Cavallin. 1990. *Overview and Comparison of US Commercial Nuclear Power Plants - Nuclear Power Plant System Sourcebook.* Technical report NUREG/CR-5640, SAIC-89/1541. US Nuclear Regulatory Commission.

Mager, T.R., M. Brumovsky, M. Erve, M.J. Banic, C. Faidy, Ph. Tipping, J. Pachner, and P.E. MacDonald. 1999. *Assessment and management of ageing of major nuclear power plant components important to safety: PWR pressure vessels.* International Atomic Energy Agency. IAEA-TECDOC-1120, October.

Maruyama, I., O. Kontani, M. Takizawa, S. Sawada, S. Ishikawa, J. Yasukouchi, O. Sato, J. Etoh, and T. Igari. 2017. “Development of the Soundness Assessment Procedure for Concrete Members Affected by Neutron and Gamma-Irradiation.” *Journal of Advanced Concrete Technology* 15:440–523.

Mazars, J., and G. Pijaudier-Cabot. 1989. “Continuum Damage Theory –Application to Concrete.” *Journal of Engineering Mechanics – ASCE* 115:345–365.

Pomaro, B., V.A. Salomoni, F. Gramegna, G. Prete, and C.E. Majorana. 2011. "Radiation damage evaluation on concrete within a facility for Selective Production of Exotic Species (SPES Project), Italy." *Journal of Hazardous Materials* 194 (0): 169–177. ISSN: 0304-3894.

Remec, I. 2013. "Radiation Environment in Concrete Biological Shields of Nuclear Power Plants." Light Water Reactor Sustainability Program.

Remec, I., T. Rosseel, K. Field, and Y. Le Pape. 2016. "Characterization of Radiation Fields for Assessing Concrete Degradation in Biological Shields of NPPs." In *9th Topical Meeting of the Radiation Protection and Shielding Division of the American Nuclear Society – (RPSD-2016).* Paris, France, October.

Risner, J., A. Alpan, and J. Yang. 2020. *Radiation Evaluation Methodology for Concrete Structures.* Technical report NUREG/CR-7281 ORNL/SPR-2020/1572. Oak Ridge: Oak Ridge National Laboratory.

Sabatino, S., A. Brooks, P. Bran Anleu, D. Arregui Mena, M. Rivers, E. Tajuelo Rodriguez, and Y. Le Pape. 2024. *Assessment of Neutron-Induced Crack Volume on Aggregates of Varied Mineralogy and Estimation of Irradiation Damage Depth in the Concrete Biological Shield.* Technical report ORNL/SPR-2024/3581–M3LW-24OR0403035. Oak Ridge National Laboratory.

Sharma, A., R. Eligehausen, and J. Asmaus. 2016. "Analytical model for concrete edge failure of multiple row anchorages with supplementary reinforcement." In *9th International Comcference on Fracture Mechanics of Concrete and Concrete Structures.* FraMCoS-9. V. Saouma, J. Bolander / E. Landis (Eds). https://doi.org/0.21012/FC9.101.

Sharma, Akanshu, Rolf Eligehausen, and Jörg Asmus. 2017. "Experimental investigation of concrete edge failure of multiple-row anchorages with supplementary reinforcement." *Structural Concrete* 18 (1): 153–163. https://doi.org/https://doi.org/10.1002/suco.201600015. eprint: https://onlinelibrary.wiley.com/doi/pdf/10.1002/suco.201600015. https://onlinelibrary.wiley.com/doi/abs/10.1002/suco.201600015.

Simpson, D. A. 2023. *H.B. Robinson Unit 2: Recommended Changes to the Surveillance Capsule Withdrawal Schedule.* Technical report CPL-RV000-TM-ME-000001. Westinghouse.

Smith, S. 2023. *H.B. Robinson Unit 2 Subsequent License Renewal: Reactor Vessel, Vessel Support and Bioshield Concrete Exposure Data.* Technical report CPL-REAC-TM-AA-000001. Westinghouse.

Society, American Nuclear. 1988. *Design Basis for Protection of Light Water Nuclear Power Plant Against the Effect of Postulated Pipe Rupture.* Technical report ANSI/ANS 58.2. American Nuclear Society.

Southern Nuclear. 2017. *Joseph M. Farley Nuclear Plant Updated Final Safety Analysis Report (Revision 27).* Technical report Docket Nos. 50-348 and 50-364, ADAMS Accession No. Chapter 3 Pt. 2 - ML17117A368; Chapters 4 and 5 - ML17117A369. Birmingham, AL.

Standard Review Plan for the Review of Safety Analysis Reports for Nuclear Power Plants: LWR Edition. n.d. Technical report NUREG-0800, Formerly issued as NUREG-75/087. U.S. Nuclear Regulatory Commission. https://www.nrc.gov/reading-rm/doc-collections/nuregs/staff/sr0800/index.html.

Team, The RELAP5-3D Code Development. 2018a. *RELAP5-3D Code Manual, Volume 1: Code Structure, System Models and Solution Methods.* Technical report INL/MIS-15-36723. Idaho National Laboratory, June 1, 2018.

———. 2018b. *RELAP5-3D Code Manual, Volume 4: Models and Correlation.* Technical report INL/MIS-15-36723. Idaho National Laboratory, June 1, 2018.

Timoshenko, S.P., and J.N. Goodier. 1986. *Theory of Elasticity.* Edited by Third Edition. McGraw-Hill.

Verrall, S., and J. Fitzpatrick. 1985. *Design concepts to minimize the activation of the biological shield of light-water reactors.* Technical report EUR 8804. Commission of the European Communities.

WCAP-8082. 1973. *Pipe Breaks for the LOCA Analysis of the Westinghouse Primary Coolant Loo.* Technical report. Proprietary. P. O. Box 355, Pittsburgh, Pennsylvania 15230: Westinghouse Electric Corporation.

Whitney, D.L., and B.W. Evans. 2010. "Abbreviations for names of rock-forming minerals." *American Mineralogist* 95:185–187.

APPENDIX A. SIMPLIFIED MODELING STRATEGY

APPENDIX A. SIMPLIFIED MODELING STRATEGY

The proposed structural model considers the effects of radiation and temperature within the thickness (i.e., r direction) of the biological wall. The constitutive model for irradiated concrete is assumed to be nonlinear elastic: the elastic parameters are a function of the r resulting from the irradiation damage. The free volumetric expansion and contraction of concrete are lumped into one single deformation $3\varepsilon_*$. The general constitutive equation is similar to that of thermo-elasticity, (Timoshenko and Goodier 1986):

$$\sigma_i = \left(k - \frac{2\mu}{3}\right) \text{tr}\, \varepsilon + 2\mu\varepsilon_i - 3k\varepsilon_*, \tag{A.1}$$

where k and μ are, respectively, the local bulk and the shear moduli of the material, and ε_* is the unrestrained thermal expansion. The latter can be replaced by any other form of physically or chemically induced expansion, ε^*—the macroscopic expansion/contraction of concrete resulting from the effects of temperature elevation; shrinkage; and RIVE: $\varepsilon^* = f(\Delta T, \Delta m/m_0, \Phi)$, where ΔT, $\Delta m/m_0$ and Φ arethe increase of temperature, the loss of mass (drying), and the neutron fluence, respectively. All these fields are spatially variable in the CBS. As a first approximation, a 1D cylindrical model is proposed, accounting primarily for the profiles of temperature, mass loss, and neutron fluence in the depth of the biological shield at the level of the RPV belt line, where the fluence is at its maximum. Hence, the materials properties subjected to degradation, volumetric expansion, and stress-strain fields are only functions of r. They represent the depth assuming the origin at the center of the reactor.

Because of the geometry of the biological shield, plane strain cylindrical conditions are assumed as $\varepsilon_z = 0$. The inner and outer radii of the biological shield wall are noted r_a and r_b, respectively. The displacement field u is only a function of the radius r. The radial and orthoradial strain fields derive from the displacement field:

$$\varepsilon_r = \frac{\partial u}{\partial r} \text{ and } \varepsilon_\theta = \frac{u}{r} \tag{A.2}$$

. The assumed confinement results in the development vertical stresses:

$$\sigma_z = \lambda\left(\varepsilon_r + \varepsilon_\theta\right) - 3k\varepsilon^* \tag{A.3}$$

. The expressions of the radial and orthoradial stresses read as follows, respectively:

$$\sigma_r = M\varepsilon_r + \lambda\varepsilon_\theta - 3k\varepsilon^* \tag{A.4}$$

,

$$\sigma_\theta = \lambda\varepsilon_r + M\varepsilon_\theta - 3k\varepsilon^*. \tag{A.5}$$

Local force equilibrium, $\partial\sigma_r/\partial r + (\sigma_r - \sigma_\theta)/r = 0$, yields after calculation to the ordinary differential equation (ODE):

$$M\frac{\partial^2 u}{\partial r^2} + \left(\frac{\partial M}{\partial r} + \frac{M}{r}\right)\frac{\partial u}{\partial r} + \left(\frac{\partial \lambda}{\partial r} - \frac{M}{r}\right)\frac{u}{r} - 3\frac{\partial}{\partial r}\left(k\varepsilon^*\right) = 0, \tag{A.6}$$

where M is the P-wave modulus, or $M = k + 4\mu/3 = E(1-\nu)/(1+\nu)/(1-2\nu)$, and λ is Lamé's first parameter, $\lambda = k - 2\mu/3$. Both M and λ are functions of the radius as a result of the irradiation damage.

The boundary conditions are obtained by writing the equality of the radial stress with the inner pressure p at the inner diameter (ID) and outer diameter outer diameter (OD) of the biological shield—$\sigma_r(r_a) = p$ and $\sigma_r(r_b) = 0$. In-service, $p = 0$. During a LOCA, $p(t) \geq 0$.

The fluence profiles are inputs of the model.

It is not possible to obtain an analytical solution of the ordinary differential equation, Eq. (A.6) in the general case of RIVE and elasticity varying with the radius. Its resolution is performed using a finite difference solver programmed with Scilab (open source software for numerical computation http://www.scilab.org/). For the sake of simplicity, an explicit scheme (second order forward) is chosen, i.e. $\partial u/\partial r \simeq (u_{n+1}-u_n)/\delta_r$ and $\partial^2 u/\partial r^2 \simeq (u_{n+2}-2u_{n+1}+u_n)/\delta_r^2$, where δ_r is the discretized space-step. After development, the explicit displacement $u_{n+2} = u(r+2\delta_r)$ is given by the equation

$$u_{n+2} = \left(2 - \frac{\delta_r}{r} - \frac{\delta_r}{M}\frac{\partial M}{\partial r}\right)u_{n+1} - \left(1 - \frac{\delta_r}{r} - \frac{\delta_r^2}{r^2} + \frac{\delta_r}{M}\frac{\partial M}{\partial r} + \frac{\delta_r^2}{rM}\frac{\partial \lambda}{\partial r}\right)u_n + 3\frac{\partial(k\varepsilon^*)}{\partial r}, \tag{A.7}$$

where u_{n+1} and u_n are the previously computed displacements at $r+\delta_r$ and r, respectively. The derivatives of M, λ, and $k\varepsilon^*$ are also computed with an explicit scheme. Recurrence relation (A.7) is valid for all n but requires the calculation of u_1 and u_2 to be applied. The pressure applied at the inner surface of the biological wall $\sigma_r(r_a) = p$ reads:

$$u_2 = u_1\left(1 - \frac{\lambda(r_a)}{M(r_a)}\frac{\delta_r}{r_a}\right) - 3\frac{k(r_a)}{M(r_a)}\varepsilon^*(r_a)\delta_r + \frac{p}{M}\delta_r. \tag{A.8}$$

Thus, once u_1 is given, $u_{n=2,\dots}$ can be explicitly calculated using (A.8) once, and then can be calculated using (A.7). The second boundary condition is given by the absence of radial stress at the outer surface of the biological shield, $\sigma_r(r_b) = 0$. Because of the second order forward integration scheme chosen, this condition cannot be implemented explicitly. The solving algorithm iteratively finds u_1 so that the computed value of $|\sigma_r(r_b)| \leq \epsilon$, where ϵ is a given small error ($\approx 10^{-3}$ MPa).